

Unveiling the 3D Structure of Magnetosheath Jets

Shahab Fatemi¹, Maria Hamrin², Eva Krämer², Herbert Gunell², Gabriella Nordin², Tomas Karlsson³, and Oleksandr Goncharov⁴

¹Department of Physics at Umeå University

²Umeå University

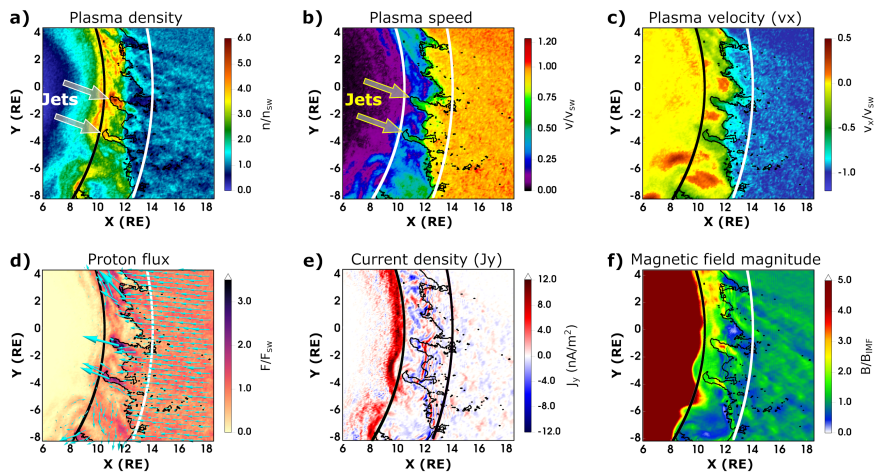
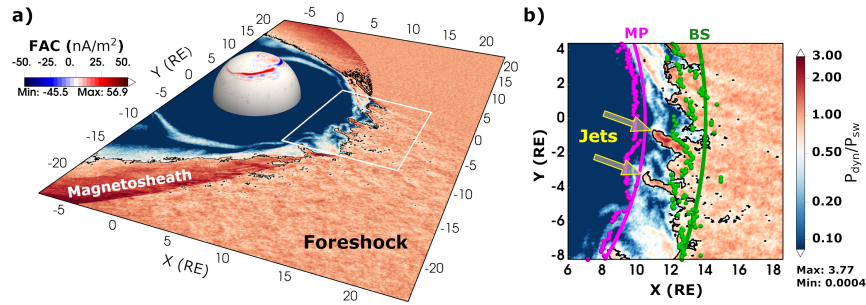
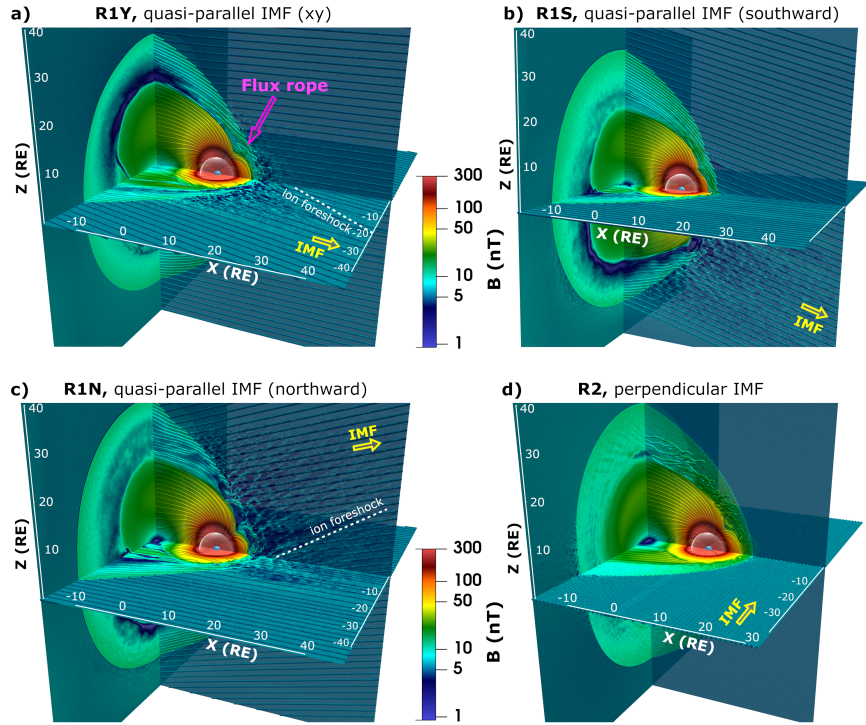
³KTH Royal Institute of Technology

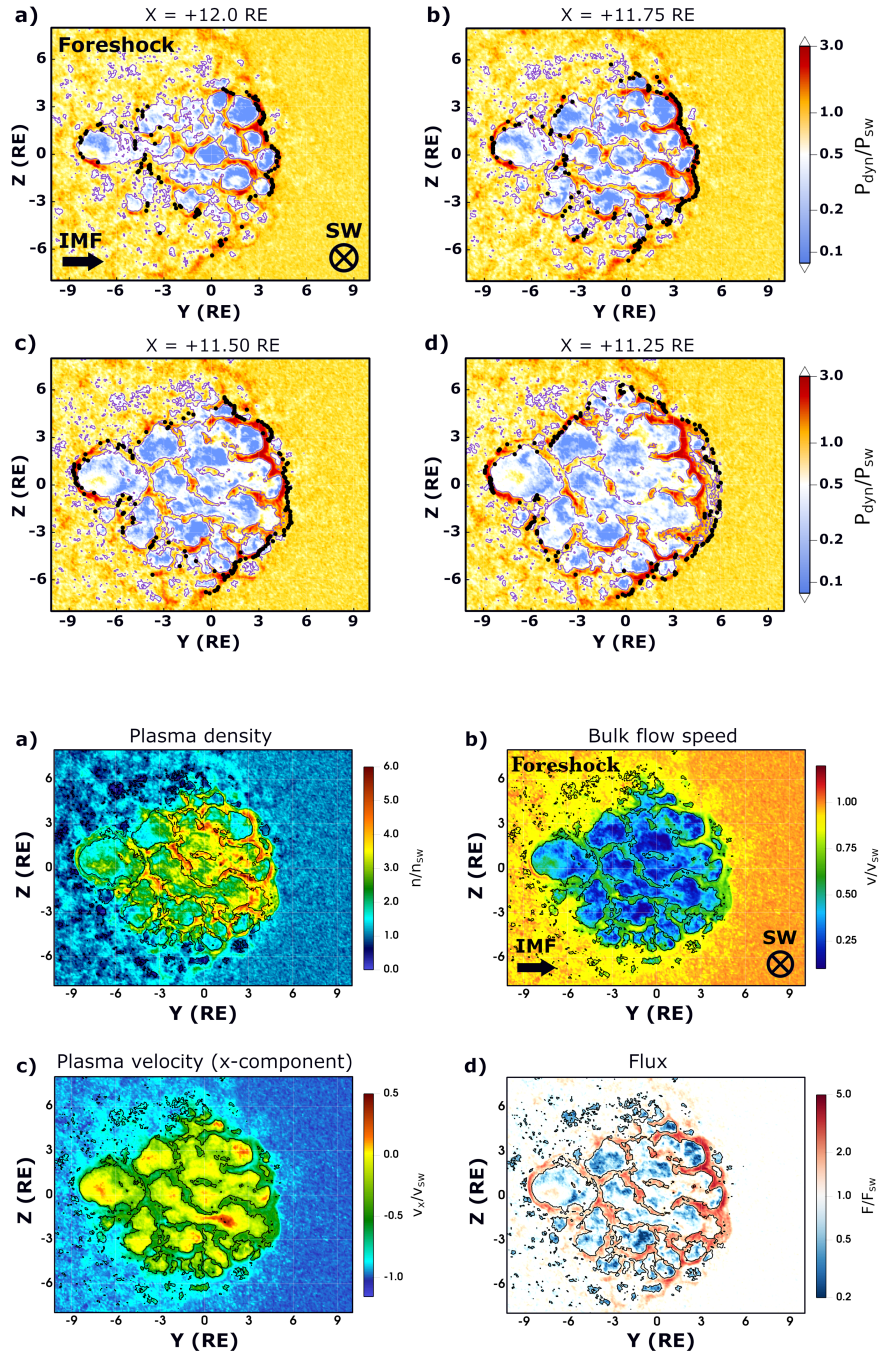
⁴Charles University in Prague

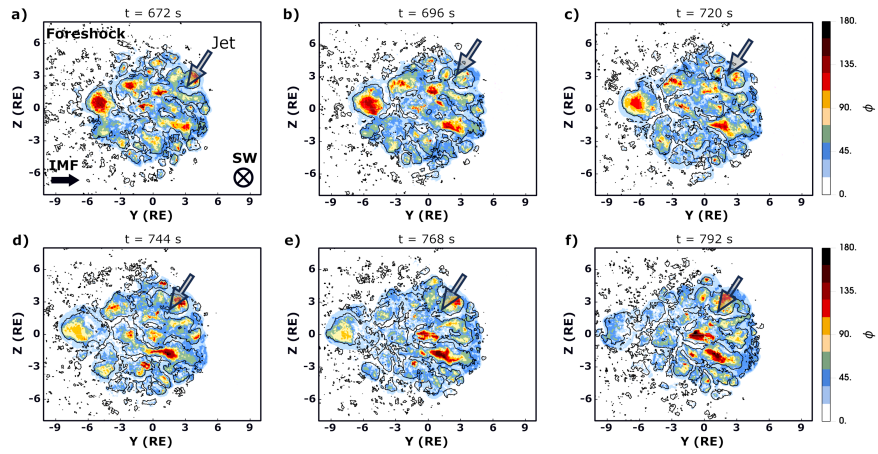
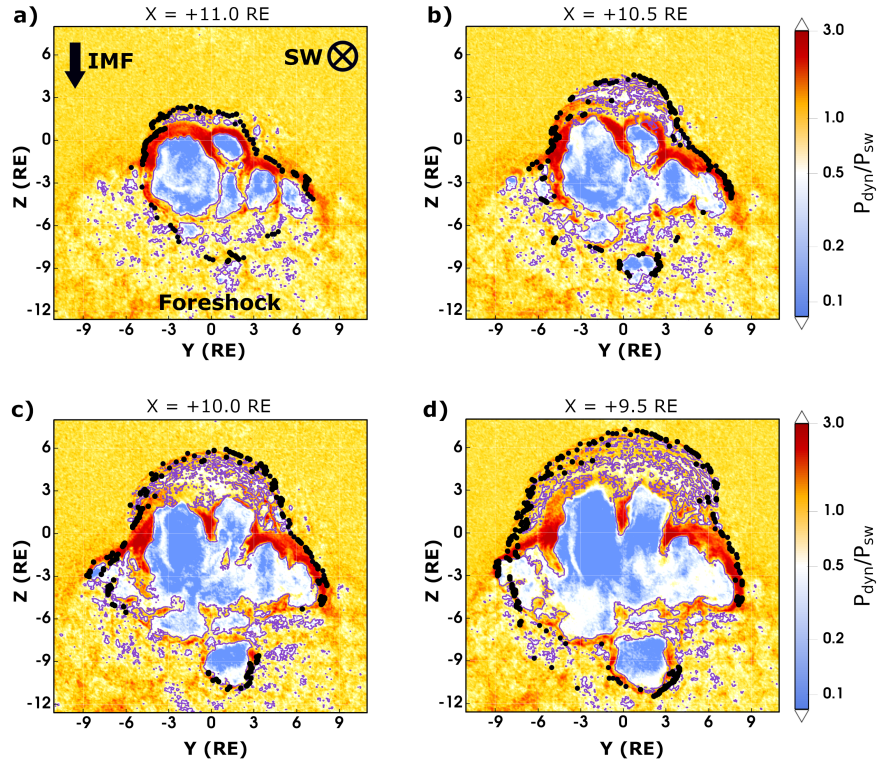
March 04, 2024

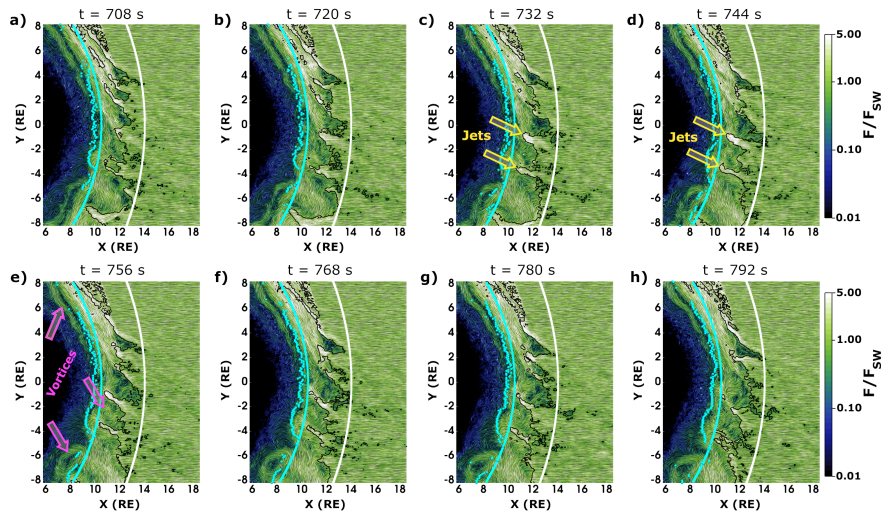
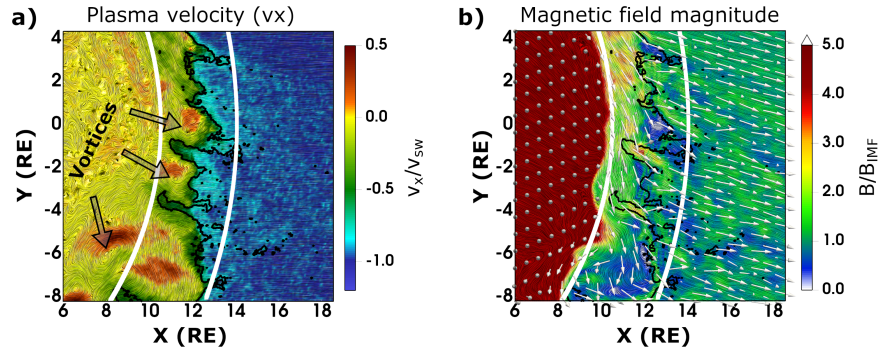
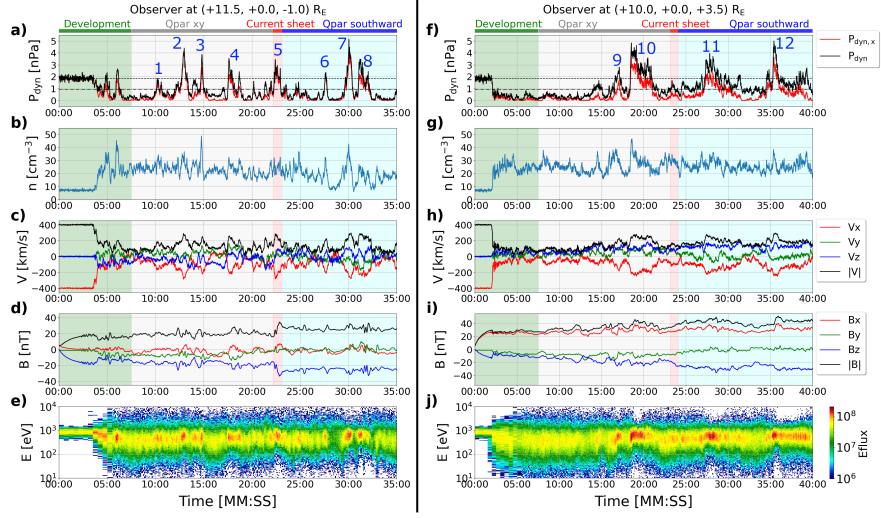
Abstract

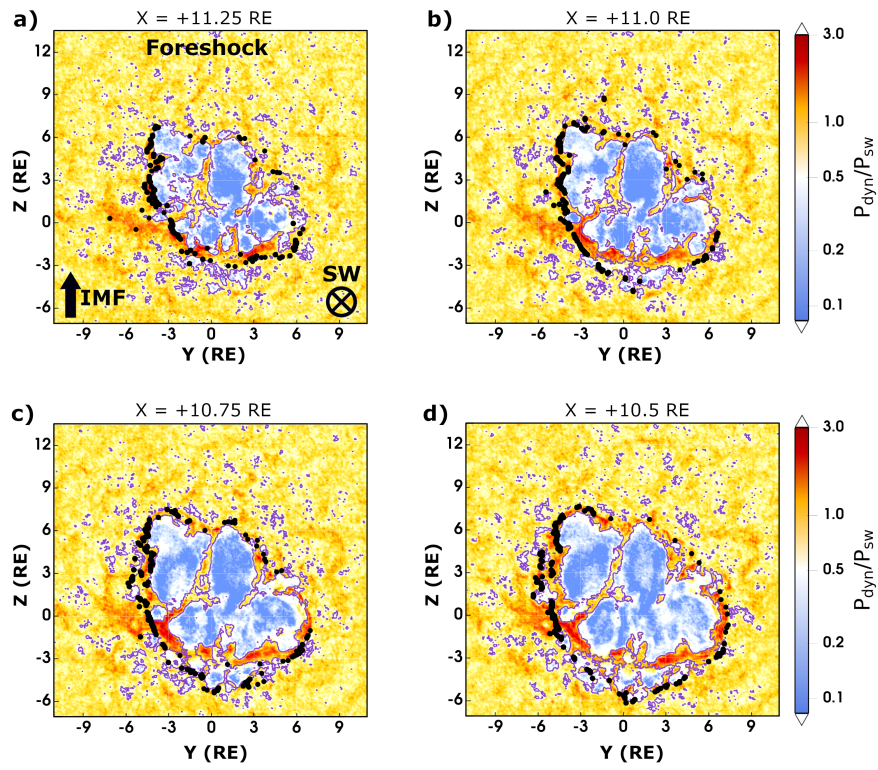
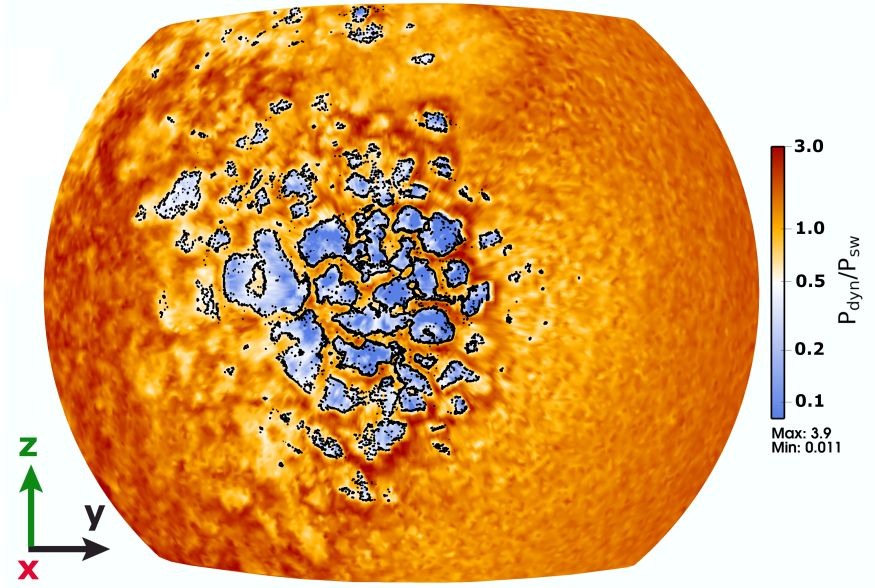
Magnetosheath jets represent localized enhancements in dynamic pressure observed within the magnetosheath. These energetic entities, carrying excess energy and momentum, can impact the magnetopause and disrupt the magnetosphere. Therefore, they play a vital role in coupling the solar wind and terrestrial magnetosphere. However, our understanding of the morphology and formation of these complex, transient events remains incomplete over two decades after their initial observation. Previous studies have relied on oversimplified assumptions, considering jets as elongated cylinders with dimensions ranging from 0.1RE to 5.0RE (Earth radii). In this study, we present simulation results obtained from Amitis, a high-performance hybrid-kinetic plasma framework (particle ions and fluid electrons) running in parallel on Graphics Processing Units (GPUs) for fast and more environmentally friendly computation compared to CPU-based models. Considering realistic scales, we present the first global, three-dimensional (3D in both configuration and velocity spaces) hybrid-kinetic simulation results of the interaction between solar wind plasma and Earth. Our high-resolution kinetic simulations reveal the 3D structure of magnetosheath jets, showing that jets are far from being simple cylinders. Instead, they exhibit intricate and highly interconnected structures with dynamic 3D characteristics. As they move through the magnetosheath, they wrinkle, fold, merge, and split in complex ways before a subset reaches the magnetopause.

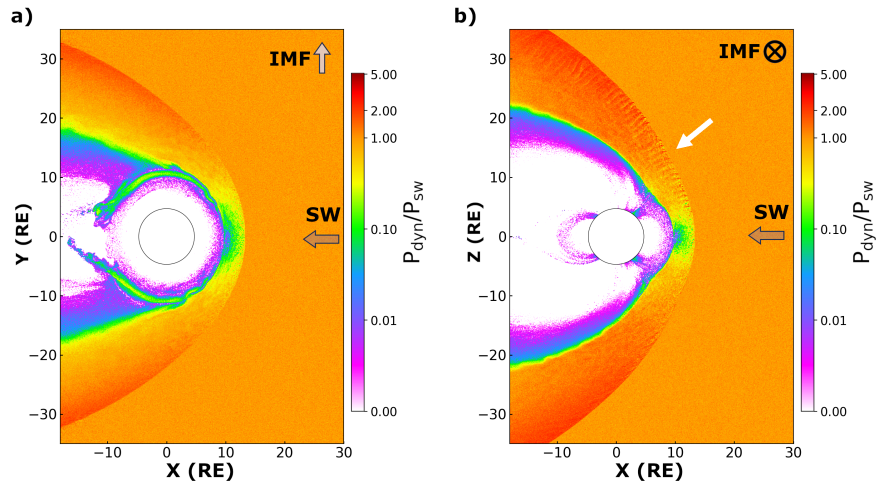
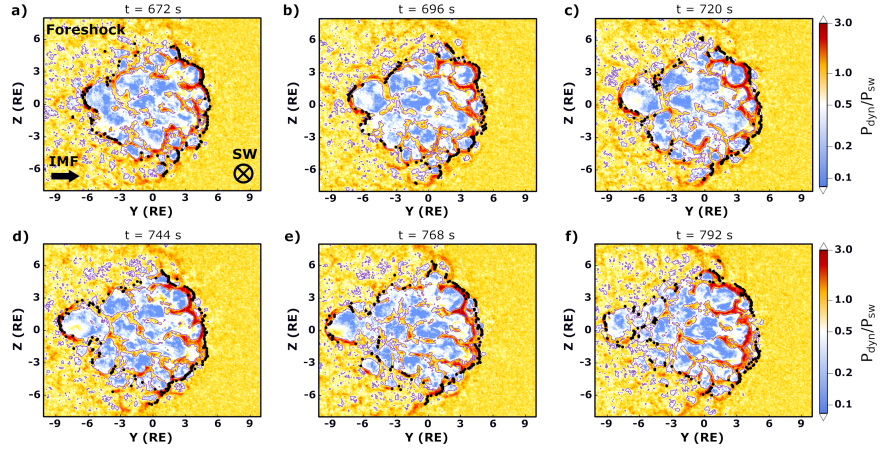


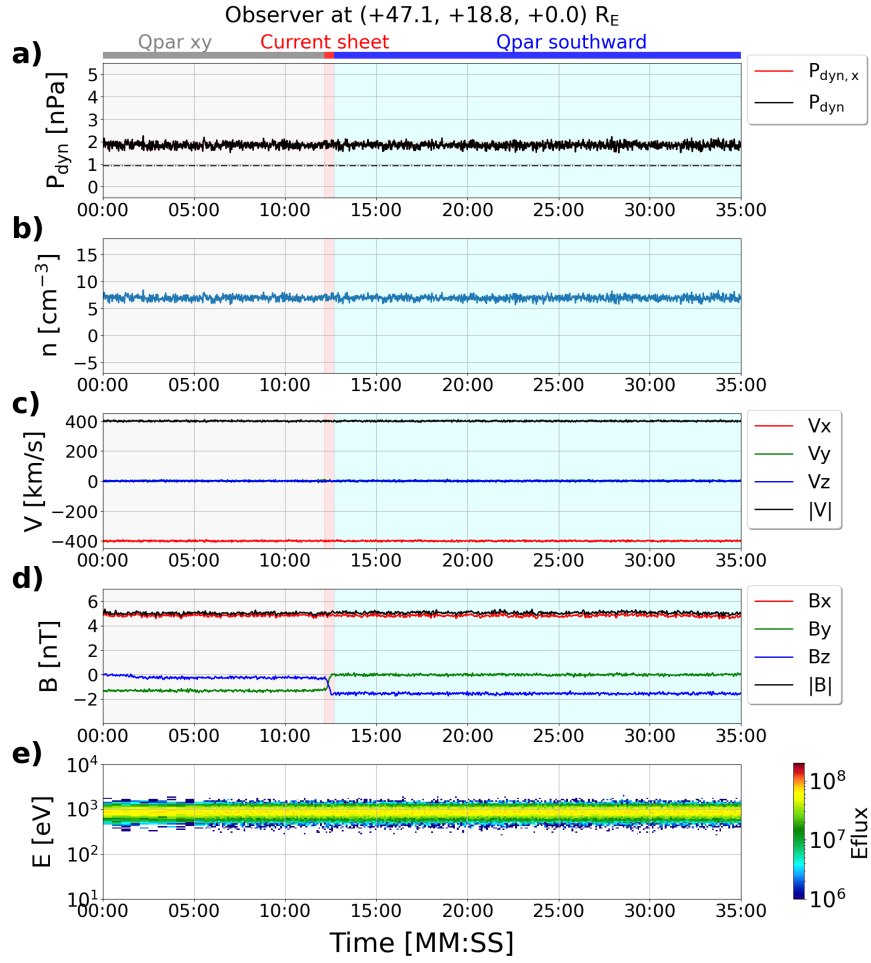












Unveiling the 3D Structure of Magnetosheath Jets

Shahab Fatemi^{1*}, Maria Hamrin¹, Eva Krämer¹, Herbert Gunell¹, Gabriella Nordin¹, Tomas Karlsson², Oleksandr Goncharov³

¹Department of Physics, Umeå University, Umeå, Sweden

²School of Electric Engineering and Computer Science, KTH Royal Institute of Technology, Stockholm, Sweden

³Faculty of Mathematics and Physics, Charles University, Prague, The Czech Republic

Key Points:

- We present the first 3D hybrid-kinetic simulation results of the solar wind interaction with the magnetosphere of Earth at physical scales
- We show the three-dimensional (3D) structure of the magnetosheath jets when the IMF is parallel to the solar wind flow direction
- Magnetosheath jets are not shaped like cylinders but are intricate, interconnected structures that split and merge in complex ways

*Address: Linnaeus väg 20, 901 87 Umeå, Sweden

Corresponding author: Shahab Fatemi, shahab.fatemi@amitiscode.com; shahab.fatemi@umu.se

Abstract

Magnetosheath jets represent localized enhancements in dynamic pressure observed within the magnetosheath. These energetic entities, carrying excess energy and momentum, can impact the magnetopause and disrupt the magnetosphere. Therefore, they play a vital role in coupling the solar wind and terrestrial magnetosphere. However, our understanding of the morphology and formation of these complex, transient events remains incomplete over two decades after their initial observation. Previous studies have relied on oversimplified assumptions, considering jets as elongated cylinders with dimensions ranging from $0.1 R_E$ to $5 R_E$ (Earth radii). In this study, we present simulation results obtained from Amittis, a high-performance hybrid-kinetic plasma framework (particle ions and fluid electrons) running in parallel on Graphics Processing Units (GPUs) for fast and more environmentally friendly computation compared to CPU-based models. Considering realistic scales, we present the first global, three-dimensional (3D in both configuration and velocity spaces) hybrid-kinetic simulation results of the interaction between solar wind plasma and Earth. Our high-resolution kinetic simulations reveal the 3D structure of magnetosheath jets, showing that jets are far from being simple cylinders. Instead, they exhibit intricate and highly interconnected structures with dynamic 3D characteristics. As they move through the magnetosheath, they wrinkle, fold, merge, and split in complex ways before a subset reaches the magnetopause.

1 Introduction

The magnetosheath is a region confined between the planetary bow shock (a boundary where the supersonic flow of the solar wind is decelerated, deflected, and heated) and the magnetopause (the outermost boundary of the magnetosphere). In this highly dynamic region, the properties of the solar wind plasma and magnetic field undergo significant changes due to compression and turbulence, making the magnetosheath a crucial region for understanding the interaction between the solar wind and planetary magnetosphere (recently reviewed by Narita et al. (2021)).

In the last two decades, spacecraft observations have frequently reported localized and temporary enhancements of plasma dynamic pressure in the magnetosheath of Earth, characterized by a sudden increase in plasma velocity and/or density compared to the surrounding magnetosheath plasma (Němeček et al., 1998; Savin et al., 2008; Hietala et al., 2009; Karlsson et al., 2012; Archer & Horbury, 2013; Hietala & Plaschke, 2013; Plaschke et al.,

2013; Gunell et al., 2014; Gutynska et al., 2015; Plaschke et al., 2017, 2020; Goncharov et al., 2020; Raptis et al., 2020). These enhancements have been observed more often at the sub-solar magnetosheath behind a quasi-parallel shock, i.e., when the interplanetary magnetic field (IMF) has a small cone angle ($<30^\circ$ with respect to the Earth-Sun line) (Archer & Horbury, 2013; Plaschke et al., 2013; Vuorinen et al., 2019; LaMoury et al., 2021). Similar phenomena have recently been observed in the magnetosheath of Mars (Gunell et al., 2023).

Currently, there is no general consensus on the nomenclature of these dynamic pressure enhancements, indicating a lack of comprehension of their underlying nature and characteristics. Throughout the years, various terminologies have been employed to describe these phenomena including “transient flux enhancements” (Němeček et al., 1998), “fast plasma streams” (Savin et al., 2012), “high energy density jets” (Savin et al., 2008), “plasmoids” (Karlsson et al., 2012; Gunell et al., 2014; Karlsson et al., 2015), and “magnetosheath jets” (Hietala et al., 2012; Plaschke et al., 2013; Dmitriev & Suvorova, 2015). We adopt the term “jets” in this study.

Previous analyses of the observed magnetosheath jets have provided different results regarding the morphology of the jets, particularly their sizes and structures (Plaschke et al., 2018). The early event studies indicated that the typical size of jets in the direction parallel to their flow motion is around $1 R_E$ (Archer et al., 2012), where $R_E = 6371$ km is the mean radius of Earth. However, large flow-parallel scale sizes ($5 R_E$) have also been observed (Dmitriev & Suvorova, 2012). Similarly, there is a wide spread in the flow-perpendicular dimension of jets, ranging from $0.2 R_E$ to a few R_E (Archer et al., 2012; Hietala et al., 2012; Gunell et al., 2014). Later, statistical analyses estimated $0.7 R_E$ for the flow-parallel dimension and nearly twice as large for the flow-perpendicular dimension of the jets (Plaschke et al., 2013). Recent re-analysis of jets suggested that the scales of jets follow a log-normal distribution (Plaschke et al., 2020). This has led to a significant reduction in their estimated sizes, with median scales of $0.15 R_E$ and $0.12 R_E$ for the flow-parallel and flow-perpendicular dimensions, respectively (Plaschke et al., 2020). Despite substantial adjustments in the estimation of jet sizes, the earlier findings concerning the rate of large jets ($> 1 R_E$) impacting the magnetopause (3 per hour, in general) remained unchanged (Plaschke et al., 2020).

In addition to observations, both local- and global-scale kinetic simulations of Earth’s magnetosheath have investigated the properties and scales of jets, and they have greatly advanced our understanding of these mysterious phenomena (Gutynska et al., 2015; Hao,

79 Lembège, et al., 2016; Omidi et al., 2016; Palmroth et al., 2018; Voitcu & Echim, 2018;
80 Preisser et al., 2020; Palmroth et al., 2021; Suni et al., 2021; Omelchenko et al., 2021;
81 Guo et al., 2022). These simulations, similar to observations, revealed a broad range of
82 sizes for jets from $0.2 R_E$ to a few R_E at various directions. Nonetheless, they consistently
83 demonstrated that the size of jets is larger in flow-parallel compared to flow-perpendicular
84 directions (e.g., Hao, Lembège, et al., 2016; Palmroth et al., 2018, 2021; Guo et al., 2022).

85 The uncertainties encountered in understanding the structure of these jets can be as-
86 sociated with oversimplified assumptions employed in their analyses. These assumptions
87 often portray jets as either cylinder-, pancake-, or finger-like shapes, exhibiting diverse sizes
88 aligned in parallel or perpendicular directions to the plasma flow or magnetic field orien-
89 tation (Archer et al., 2012; Karlsson et al., 2012; Plaschke et al., 2016, 2018; Palmroth et
90 al., 2021; Plaschke et al., 2020; Goncharov et al., 2020; Guo et al., 2022). In addition, all
91 the previously applied kinetic models to investigate magnetosheath jets have either been
92 two-dimensional (2D) models in the spatial domain (configuration space) (Gutynska et al.,
93 2015; Hao, Lembège, et al., 2016; Omidi et al., 2016; Palmroth et al., 2018; Preisser et al.,
94 2020; Palmroth et al., 2021; Suni et al., 2021; Guo et al., 2022) or three-dimensional (3D)
95 models with reduced scales of Earth (Karimabadi et al., 2014; Omidi et al., 2016; Ng et
96 al., 2021; Omelchenko et al., 2021) or focused on a small region in the magnetosheath (e.g.,
97 Voitcu & Echim, 2018). Furthermore, spacecraft observations at specific locations in the
98 magnetosheath are unable to cover and probe a large spatial area at once, and therefore,
99 provide a limited “1D snapshot” view of jets. Consequently, due to the lack of comprehen-
100 sion of the structure of the jets, several assumptions and simplifications have been made
101 that can lead to uncertainties and ambiguities in our understanding of the morphology of
102 these phenomena.

103 In addition to their sizes and structures, the formation mechanism of jets has also
104 remained elusive (Plaschke et al., 2018, 2020). Observations suggest that the occurrence
105 of jets downstream of the quasi-parallel shock is more frequent in proximity to the bow
106 shock as compared to the magnetopause (Archer & Horbury, 2013; Plaschke et al., 2013;
107 Goncharov et al., 2020). On the contrary, the occurrence frequency of jets increases toward
108 the magnetopause downstream of the quasi-perpendicular shock (Archer & Horbury, 2013).
109 It has been suggested that the formation of jets downstream of the quasi-parallel shock
110 can be linked to the foreshock structures and/or the bow shock ripples, and reformation
111 (Hietala & Plaschke, 2013; Omidi et al., 2016; Hao, Lembège, et al., 2016; Hao, Lu, et al.,

112 2016; Kajdič et al., 2017; Gutynska et al., 2015; Karlsson et al., 2015; Suni et al., 2021;
113 Raptis, Karlsson, Vaivads, Pollock, et al., 2022). Moreover, jets have been observed more
114 frequently when the IMF exhibits a higher level of stability (Savin et al., 2008; Hietala et
115 al., 2009; Archer & Horbury, 2013; Plaschke et al., 2013). This suggests that, in general, the
116 formation of jets is not directly associated with IMF discontinuities or transient events such
117 as magnetic discontinuities and hot flow anomalies (Hietala & Plaschke, 2013; Plaschke et
118 al., 2013; Karimabadi et al., 2014; Suni et al., 2021; Raptis, Karlsson, Vaivads, Pollock, et
119 al., 2022).

120 Despite the lack of understanding of the nature and formation mechanism of magne-
121 tosheath jets, observations have found compelling evidence that jets play a crucial role in
122 coupling between the solar wind and planetary magnetospheres by transferring a significant
123 amount of energy and momentum towards and into the magnetosphere (Savin et al., 2008;
124 Shue et al., 2009; Savin et al., 2012; Gunell et al., 2012, 2014; Dmitriev & Suvorova, 2015;
125 Plaschke et al., 2016). They also contribute to various fundamental plasma processes, such
126 as wave generation (Karlsson et al., 2018; B. Wang et al., 2022; Krämer et al., 2023), plasma
127 acceleration (Lavraud et al., 2007; Liu et al., 2019), and magnetic reconnection (Phan et
128 al., 2007; Hietala et al., 2018; Ng et al., 2021). Beyond their impact on the magnetosphere,
129 these jets exhibit observable effects even on the ground, including geomagnetic disturbances,
130 enhancements in ionospheric outflow, and dayside aurora (Hietala et al., 2012; Han et al.,
131 2016; B. Wang et al., 2018; Norenus et al., 2021; B. Wang et al., 2022). Such far-reaching
132 influences highlight the significance of the jets in the solar wind coupling with the magne-
133 tosphere and ionosphere of Earth (Plaschke et al., 2018; Rakhmanova et al., 2023). However,
134 the extent of their impact remains uncertain, mainly due to our limited understanding of
135 their structure, dimensions, and formation mechanisms (Plaschke et al., 2018).

136 In this study, we present the first 3D configuration of magnetosheath jets using the
137 Amitis code, a state-of-the-art hybrid-kinetic plasma model (Fatemi et al., 2017). We have
138 successfully resolved, for the first time, the time-dependent, global 3D interaction (both
139 spatial and velocity domains) between the solar wind and Earth’s magnetosphere using the
140 physical scales of the Earth’s magnetosphere. By simulating typical solar wind conditions
141 near the orbit of Earth, we present a new view of the structure of jets forming within the
142 magnetosheath.

2 Model and Methods

2.1 Amitis Model

In this study, we use an upgraded version of the Amitis code, a high-performance hybrid-kinetic plasma model that runs in parallel on multiple Graphics Processing Units (GPUs) instead of a single GPU (Fatemi et al., 2017, 2022). Amitis is 3D in both configuration and velocity spaces, time-dependent, and grid-based kinetic plasma framework (Fatemi et al., 2017). In this model, the ions are kinetic, charged macro-particles, and electrons are a massless, charge-neutralizing fluid. The model is the first of its kind that runs entirely on GPUs and it runs at least 10 times faster and more energy and cost-efficient (environmentally friendly) compared to its parallel CPU-based predecessors (Fatemi et al., 2017).

In our model, an ion position, \mathbf{r}_i , and velocity, \mathbf{v}_i , are obtained from the Lorentz equation of motion

$$\frac{d\mathbf{v}_i}{dt} = \frac{q_i}{m_i} (\mathbf{E} + \mathbf{v}_i \times \mathbf{B}), \quad \frac{d\mathbf{r}_i}{dt} = \mathbf{v}_i, \quad (1)$$

where q_i and m_i are the charge and mass of a macro-particle ion, respectively. \mathbf{E} is the electric field and \mathbf{B} is the magnetic field applied to the ion at its position. We calculate the electric field from the electron momentum equation for mass-less electrons ($m_e = 0$), which is given by

$$\mathbf{E} = \overbrace{\mathbf{J} \times \mathbf{B} / \rho_i}^{\text{Hall}} + \overbrace{\eta \mathbf{J}}^{\text{Ohmic}} - \overbrace{\mathbf{u}_i \times \mathbf{B}}^{\text{Convective}} - \overbrace{\nabla p_e / \rho_i}^{\text{Ambipolar}}, \quad (2)$$

where \mathbf{J} is the electric current density calculated from Ampère's law where displacement current is neglected (i.e., $\mathbf{J} = \nabla \times \mathbf{B} / \mu_0$), ρ_i is the charge density of macro-particle ions, η is the resistivity, \mathbf{u}_i is the bulk flow velocity of ions, and p_e is the electron pressure. Different electric field terms including the Hall, ohmic, convective, and ambipolar electric fields are labeled in Equation 2. Amitis can solve electron pressure tensors, but for simplicity in this study, we assume that electrons are an ideal gas with $p_e \propto n_i^\gamma$, where $\gamma = 5/3$ is the adiabatic index and n_i is the ion density. Therefore, the pressure gradient in Equation 2 is comparable to the ion density gradient in our model. We advance the magnetic field in time using Faraday's law, $\partial \mathbf{B} / \partial t = -\nabla \times \mathbf{E}$. The model principles are described in detail by Fatemi et al. (2017).

Amitis has been extensively applied to study plasma interactions with various planetary bodies including the Moon, Mercury, Ganymede, Mars, Comets, and several asteroids (e.g., Fatemi et al., 2017; Fuqua-Haviland et al., 2019; Fatemi et al., 2020; Aizawa et al., 2021;

166 Poppe et al., 2021; Rasca et al., 2022; Fatemi et al., 2022; Shi et al., 2022; X.-D. Wang et
 167 al., 2023; Poppe & Fatemi, 2023; Gunell et al., 2024). In addition, its results have been
 168 successfully validated through comparison with spacecraft observations (e.g., Fatemi et al.,
 169 2017, 2020; Aizawa et al., 2021; Rasca et al., 2022; Fatemi et al., 2022; X.-D. Wang et al.,
 170 2023), theories (Fuqua-Haviland et al., 2019), and other kinetic and magnetohydrodynamic
 171 (MHD) models (Fatemi et al., 2017; Aizawa et al., 2021).

172 **2.2 Coordinate System and Simulation Setup**

173 In our analysis, we utilize the Geocentric Solar Magnetospheric (GSM) coordinate sys-
 174 tem, which is centered at Earth’s center of mass. In this coordinate system, the $+x$ axis
 175 is directed towards the Sun, representing the direction opposite to the flow direction of the
 176 solar wind. The $+z$ axis points to the northern magnetic pole and the $+y$ axis completes the
 177 right-handed coordinate system. To perform our simulations, we employ a simulation do-
 178 main with dimensions $-19 R_E \leq x \leq +53 R_E$ and at smallest $-55 R_E \leq (y, z) \leq +55 R_E$,
 179 where $1 R_E = 6371$ km is the radius of Earth in our simulations. To discretize our simu-
 180 lation domain, we employ a regularly spaced Cartesian grid with cubic cells of size 500 km
 181 ($\approx 0.078 R_E$).

182 The focus of this study is on the structure of the solar wind interaction with the dayside
 183 magnetosphere, primarily the magnetosheath jets. Therefore, we exclude the simulation of
 184 Earth’s atmosphere, ionosphere, and exosphere by assuming that the inner boundary of
 185 the magnetosphere is a conductive sphere with a radius of 30,000 km ($\approx 4.7 R_E$), centered
 186 at the origin of our coordinate system. When a particle impacts this inner boundary, we
 187 remove that particle from the simulation domain. The choice for the size and configuration
 188 of the inner boundary aligns with previous simulations of Earth by the Vlasiator model
 189 (e.g., Palmroth et al., 2018, 2021).

190 The inflow boundary ($x = +53 R_E$) and the outflow boundary ($x = -19 R_E$) of our sim-
 191 ulations act as a perfect plasma absorber. At the inflow boundary, kinetic macro-particles
 192 are continuously injected into the simulation domain, following a drifting Maxwellian ve-
 193 locity distribution function. Along the y - and z -axes, the boundaries are assumed to be
 194 periodic for both electromagnetic fields and particles. This means that along the y - and
 195 z -axes the electromagnetic fields and particles are replicated from one side to the other side
 196 of the simulation domain.

197 We incorporate the actual scales of the Earth’s magnetic field in our simulations. We
 198 adopt a magnetic dipole model with a magnetic moment $M = 8.22 \times 10^{22} \text{ A m}^2$ (Walt, 1994)
 199 positioned at the center of the Earth and oriented exactly along the $-z$ axis. This magnetic
 200 moment generates a surface equatorial magnetic field of $\sim 32 \mu\text{T}$ at a distance of $1 R_E$, and
 201 $\sim 305 \text{ nT}$ at the inner boundary (plasma absorber) of our simulations at $4.7 R_E$.

202 At the inflow boundary where the solar wind enters our simulation domain, we employ
 203 32 macro-particles per grid cell consisting exclusively of protons with mass $1.67 \times 10^{-27} \text{ kg}$
 204 and charge $1.60 \times 10^{-19} \text{ C}$. For simplicity, we do not include solar wind He^{++} or heavier
 205 ions (e.g., O^{+6}) in our simulations, explained in detail in Section 2.5. Within our simulation
 206 domain, we track the trajectories of over 40 billion macro-particle protons at every simulation
 207 time step. To achieve this, we utilize a time step of $\Delta t = 8 \times 10^{-3} \text{ s}$, which is 5×10^{-4} of
 208 the upstream solar wind proton gyro-period away from magnetospheric disturbances and
 209 is 3×10^{-2} of a proton gyro-period near magnetospheric poles at the inner boundary of
 210 our simulations. By employing such a small time step, we ensure that the gyromotion of
 211 the solar wind protons is fully resolved within the entire simulation domain and Courant-
 212 Friedrich-Lewy (CFL) condition is fulfilled.

213 Within our model, the plasma resistivity is uniformly set to $10^4 \Omega \text{ m}$ wherever the ions
 214 exist. This resistivity is primarily required to damp numerical oscillations and to facilitate
 215 magnetic reconnection to occur in our simulations (Fatemi et al., 2017, 2020, 2022). To
 216 effectively handle the vacuum regions that arise in our simulations, such as those found
 217 in the magnetotail, we incorporate a vacuum resistivity of $0.2 \times 10^7 \Omega \text{ m}$, as described in
 218 Holmström (2013) and Fatemi et al. (2017). Whenever the density of a grid cell falls below
 219 1% of the undisturbed (upstream) solar wind plasma density, we dynamically assign the
 220 vacuum resistivity to those cells. In these vacuum regions, we solve the magnetic diffusion
 221 equation instead of utilizing general Faraday’s law, as explained in detail by Holmström
 222 (2013) and Fatemi et al. (2017).

223 In this study, we perform a series of hybrid simulations using the Amitis code for the
 224 “typical” solar wind conditions near Earth, i.e., the solar wind speed of 400 km/s , plasma
 225 density of 7 cm^{-3} , and magnetic field strength of 5 nT (Kivelson & Russell, 1995). The solar
 226 wind plasma and magnetic field configurations applied in our simulations are summarized
 227 in Table 1. In this table, the calculation for plasma dynamic pressure, represented as P_{dyn} ,
 228 is given by $P_{\text{dyn}} = mn\mathbf{v}^2$, where m represents the proton mass, n is the plasma density, and

229 \mathbf{v} is the plasma flow velocity. In the solar wind, $P_{\text{sw}} = mn_{\text{sw}}v_{\text{sw}}^2$. The plasma β denotes
 230 the ratio between the solar wind thermal pressure and the magnetic pressure. M_A , M_s , and
 231 M_{ms} are the Alfvén, sonic, and magnetosonic Mach numbers, respectively.

Table 1. Solar wind plasma parameters and IMF configurations applied in our simulations. Only the IMF orientation is different between the simulation runs.

Run	$\mathbf{B}_{\text{IMF}}(B_x, B_y, B_z)$ (nT)	$ \mathbf{B} $ (nT)	n_{sw} (cm^{-3})	$\mathbf{v}_{\text{sw}}(v_x, v_y, v_z)$ (km/s)	$T_i = T_e$ (eV)	P_{sw} (nPa)	β	M_A	M_s	M_{ms}
R1Y	(+4.83, +1.30, 0.0)	5.0	7.0	(-400, 0, 0)	10.0	1.86	1.1	9.7	7.1	5.7
R1S	(+4.83, 0.0, -1.30)									
R1N	(+4.83, 0.0, +1.30)									
R2	(0.0, +5.0, 0.0)									

232 Our simulations consisted of different scenarios. First, we conducted a simulation where
 233 the IMF is directed radially outward from the Sun (run R1), forming a 15° angle from the
 234 solar wind flow direction (i.e., quasi-parallel to the solar wind flow). Note that in this
 235 manuscript, the term “quasi-parallel IMF” refers to the direction of the IMF relative to
 236 the upstream solar wind flow direction, and not to the bow shock normal, unless stated
 237 otherwise. As outlined in Table 1, the R1 simulation run consists of three distinct IMF con-
 238 figurations. Initially, the IMF had only x and y components (run R1Y). After approximately
 239 11 minutes of physical time, we changed the IMF orientation upstream in our simulations
 240 (i.e., the inflow boundary) and made it southward (R1S), propagating into the simulation
 241 domain while the magnitude and cone angle of the IMF remained unchanged. Subsequently,
 242 after nearly 35 minutes, we again changed the IMF to a northward orientation (R1N). This
 243 allowed us to simulate the passage of two consecutive current sheets (magnetic transients)
 244 through our simulations.

245 In the R1 simulation, the IMF changes occurred in the format of a step-function where
 246 the magnetic field orientation changed. For example, see time 12:30 in Figure S7d in the
 247 supplementary materials where the y -component of the magnetic field changes from +1.3 nT
 248 to zero, and the z -component of the magnetic field changes from zero to -1.3 nT. However,
 249 due to the non-zero plasma resistivity applied in our simulations ($10^4 \Omega \text{m}$), these changes
 250 formed a magnetic transient (current sheet) with a width of $\approx 1 R_E$ propagating through

251 the entire simulation domain, interacting with Earth. Choosing a smaller plasma resistivity
 252 results in a narrower current sheet, but increases the numerical noise in our simulations.
 253 Before the arrival of the current sheet and after its passage, the solar wind parameters,
 254 and magnetic field configurations remained constant upstream of our simulation domain,
 255 indicating a relatively constant environment in terms of solar wind conditions and magnetic
 256 field configurations.

257 In addition to the R1 simulation series, we conducted one simulation with the IMF
 258 perpendicular to the solar wind flow direction (R2), listed in Table 1. Throughout this run,
 259 we maintained a fixed IMF orientation without making any changes. The solar wind plasma
 260 parameters including plasma density, velocity, and temperature remained unchanged during
 261 both R1 and R2 simulations.

262 The simulation results presented here (Figures 1–7) are taken before the arrival of
 263 the current sheets at $x = +25 R_E$ and/or long after the previous current sheet passed the
 264 dayside magnetosphere. This ensures that the dayside magnetosphere has responded to
 265 the magnetic transients and **fully developed** and is stable in the analyses presented in
 266 this manuscript. Detailed investigations on the response of the magnetosphere to magnetic
 267 transients and how the bow shock, magnetosheath jets, and magnetopause respond to IMF
 268 variations are beyond the scope of this study, saved for future research.

269 **2.3 Jet Selection Criteria**

270 Various methods have been applied to detect magnetosheath jets from observed space-
 271 craft data, summarized in Plaschke et al. (2018). Among those, two general approaches
 272 are commonly used: (a) comparing observed features with time-averaged local background
 273 conditions in the magnetosheath (Archer & Horbury, 2013; Karlsson et al., 2012), and (b)
 274 comparing the observed features with undisturbed solar wind plasma and magnetic field
 275 upstream of the bow shock (Plaschke et al., 2013). However, both methods have limita-
 276 tions, as thoroughly reviewed by Plaschke et al. (2018). Utilizing a running average (often
 277 tens of minutes) to establish the local background imposes a limitation on the timescales
 278 of detectable transient events, like jets (Plaschke et al., 2013). The averaging timescales
 279 must be considerably longer than the duration of most transients and exceed their typical
 280 recurrence timescale (Archer & Horbury, 2013; Plaschke et al., 2013). Comparison with
 281 the upstream solar wind conditions allows for a broader range of timescales, but it requires

282 information on the solar wind, which is often not readily available to a spacecraft located
 283 downstream of the bow shock. Therefore, the solar wind observations by other satellites
 284 that continuously monitor the solar wind plasmas are used (e.g., ACE or Wind spacecraft
 285 data) and time-shifted to the nominal sub-solar bow shock (e.g., Plaschke et al., 2013, 2018).
 286 This time-shifting method can introduce complications and uncertainties in analyzing the
 287 data in the magnetosheath and the magnetosphere of Earth. However, this is not an issue
 288 in numerical simulations, because the upstream conditions are very well-known and can be
 289 accurately tracked in time in the simulations. Therefore, we use the latter approach in this
 290 study (i.e., method b).

291 One of the commonly employed thresholds using upstream solar wind conditions is
 292 $P_{\text{dyn},x} \geq 0.5P_{\text{sw}}$, where $P_{\text{dyn},x}$ is the dynamic pressure in the magnetosheath along the
 293 x axis, and P_{sw} is the solar wind dynamic pressure, explained by Plaschke et al. (2013).
 294 This threshold, referred to as the ‘‘Plaschke criterion’’ throughout this study, should only
 295 be applied to the sub-solar region (Plaschke et al., 2013). We use this criterion to select
 296 jets in the magnetosheath in our simulations. Since the IMF is nearly parallel to the solar
 297 wind flow direction during the R1 simulation run, and our focus is on the magnetosheath
 298 jets forming near the sub-solar region, the Plaschke criterion is a valid assumption in the
 299 presented analyses in this study. We limit our investigations spatially to the sub-solar region
 300 with a maximum 30° deviation from the Earth-Sun line (Plaschke et al., 2013, 2018).

301 2.4 Magnetospheric Boundary Selection Criteria

302 Determining magnetospheric boundaries, such as the bow shock and the magnetopause,
 303 in the sub-solar region during quasi-parallel IMF configurations is not straightforward due
 304 to the disturbances associated with the foreshock. This complication holds for both sim-
 305 ulations and spacecraft data. Our approach to select these boundaries in our simulations
 306 primarily relies on analyzing the intensity and direction of electric currents, \mathbf{J} , computed
 307 from Ampère’s law using our simulation data, a privilege available for 3D simulations. In
 308 previous studies, we successfully employed this method to identify magnetospheric bound-
 309 aries at Mercury (Fatemi et al., 2018, 2020) and Ganymede (Fatemi et al., 2022). While
 310 the electric current density is our primary method to identify magnetospheric boundaries,
 311 for the R1 simulation series, however, the presence of the foreshock region makes it chal-
 312 lenging to accurately pinpoint the bow shock’s location in the sub-solar region. To address

313 this issue, we incorporate additional criteria in conjunction with the electric current density
 314 analysis. The criteria are as follows:

- 315 • The electric current intensity should exceed 3 nA/m^2 at the boundary,
- 316 • The plasma density downstream of the bow shock boundary should be higher than
 317 the upstream solar wind plasma density due to solar wind compression at the bow
 318 shock, and
- 319 • The bulk flow speed downstream of the bow shock boundary should be smaller than
 320 the solar wind plasma speed, due to the deceleration of plasma at the bow shock.

321 To identify the magnetopause boundary, we use the electric current density, and we
 322 choose 9 nA/m^2 as the minimum requirement for the current density at the magnetopause.
 323 Using these criteria, we selected the magnetopause and bow shock boundaries in our simu-
 324 lations. To validate our simulation results, we compare the location of the bow shock and
 325 magnetopause boundaries obtained from our simulations with an empirical model by Chao
 326 et al. (2002).

327 **2.5 Limitations in Simulations**

328 The presented results in this study come with certain limitations primarily due to the
 329 applied numerical method and the limited computational resources. The main limitations
 330 of this study are as follows:

- 331 • In our simulations, we focus exclusively on the solar wind protons and their impact
 332 on the overall interaction between the solar wind and Earth. Notably, the solar wind
 333 is comprised of various multiply charged heavy ion species like He^{+2} , O^{+6} , Si^{+8} , and
 334 Fe^{+9} (Bame et al., 1970; Bochsler, 2007). However, protons are the dominant solar
 335 wind ion species (averaging over 95%), and for simplicity, we do not include heavy
 336 ions in this study. While the current version of Amitis is capable of handling over 10
 337 ion species (e.g., Poppe et al., 2021), investigating the effect of the heavy ions in the
 338 formation, evolution, and morphology of the jets is an interesting research topic that
 339 remains for future investigation.
- 340 • The nature of hybrid models prevents us from including electron dynamics and their
 341 contributions to the interaction with the magnetosphere in this study. In addition,
 342 due to the lack of electron dynamics, our simulations underestimate the plasma accel-

343 eration associated with charge separation. As previously discussed by Fatemi et al.
 344 (2012), the ambipolar electric field in hybrid models, which is related to the electron
 345 pressure gradient shown in Equation 2, typically contributes less to plasma energiza-
 346 tion compared to simulations that explicitly resolve electron dynamics. Currently, the
 347 space physics community lacks a fully kinetic plasma model that accurately handles
 348 electron dynamics and includes 3D plasma interaction with planetary bodies in their
 349 physical scales.

- 350 • Generally, in a hybrid model of plasma the simulation cell size, ΔL , should be nearly
 351 an order of magnitude larger than δ_e , where $\delta_e = c/\omega_{pe}$ is the electron inertial length,
 352 c is the speed of light, and ω_{pe} is the electron plasma frequency (e.g., Harned (1982)
 353 and the review by Ledvina et al. (2008) and the references therein). For proton
 354 and electron, the ratio between the ion-inertial (δ_i) and electron-inertial length scales
 355 $\delta_i/\delta_e = \sqrt{m_i/m_e} \approx 43$, where m_i and m_e are the proton and electron mass, respec-
 356 tively. Therefore, ΔL in a hybrid model should be larger than $10\delta_e/43 \approx 0.25\delta_i$.
 357 Although the simulation cell sizes in hybrid models are sometimes comparable to or
 358 smaller than the ion inertial length, Tóth et al. (2017) have shown that as long as the
 359 global scales of a simulation are larger than δ_i , the global solution is not sensitive to
 360 the actual value of δ_i . Their finding is in agreement with earlier hybrid simulations
 361 of various solar system bodies obtained from different hybrid models where the sim-
 362 ulation cell sizes are larger than $\sim 2\delta_i$ (e.g., Kallio, 2005; Brain et al., 2010; Müller
 363 et al., 2012; Holmström et al., 2012; Fatemi et al., 2018; Exner et al., 2020; Jarvinen
 364 et al., 2020; Aizawa et al., 2021; A. Le et al., 2023), and sometimes even larger than
 365 $10\delta_i$ (e.g., Kallio & Janhunen, 2004), chosen based on the kinetic scales of interest.
 366 However, some of the hybrid models that have chosen cell sizes comparable to or
 367 smaller than δ_i have scaled down the global physical size of the interaction region
 368 (e.g., Karimabadi et al., 2014; Herčík et al., 2016; Omelchenko et al., 2021), and
 369 therefore, the relative size of δ_i to the interaction scale size is larger than the physi-
 370 cal ratios. In all the simulation results presented here, we have used regular-spaced
 371 Cartesian cubic grids of size $\Delta L = 500$ km ($\approx 0.08 R_E$), which is $\approx 5.8\delta_i$ for the solar
 372 wind parameters listed in Table 1. The global scales of the resolved phenomena in
 373 our simulations are larger than ΔL (e.g., the stand-off distance of the magnetopause
 374 is at $\approx 120\Delta L$), and the spatial length scales of the magnetosheath jets are a few
 375 times, if not an order of magnitude, larger than ΔL . Therefore, the selection for our

376 cell sizes does not affect the global pattern of the jets and magnetospheric structures
 377 (e.g., foreshock, bow shock, and vortices) captured by the simulations presented in
 378 this study. However, it is worth noting that our presented results do not address jets
 379 of sizes smaller than ΔL .

- 380 • Achieving extremely high simulation grid resolution (e.g., cell sizes comparable to
 381 or even smaller than δ_i) to simulate the global 3D kinetic structure of the Earth’s
 382 magnetosphere using its physical scales, while desirable, has been a decadal challenge
 383 for computation, and still remains impossible using kinetic (particle-based) models
 384 even using cutting-edge technologies like GPUs, at least with the current size of
 385 GPU’s internal memory (known as the global memory, which is maximum 80 GB on
 386 Nvidia A100 series at the time of this writing). In this study, we used 64 Nvidia A100
 387 GPUs, and as explained previously, $\Delta L \approx 5.8\delta_i$ in our simulations. Reducing the cell
 388 sizes from $5.8\delta_i$ to $1.0\delta_i$ requires using at least $5.8^3 \approx 200$ times more GPUs than
 389 those used in this study (!), which is currently not available to regular users of the
 390 large-scale supercomputers. Quantum computing shows promise for achieving such
 391 extremely high-resolution simulations, but this capability is not fully developed yet
 392 and will be accessible in the future.

393 While our presented results in this study shed light on important aspects of magne-
 394 tosheath jets and unveil their structure, it is important to acknowledge the limitations of our
 395 simulations when interpreting and generalizing the results. Future research with improved
 396 numerical methods and enhanced computational capabilities will help to address some of
 397 these constraints and provide a more comprehensive understanding of the subject matter.

398 **3 Results**

399 Here, we present the first 3D simulation results of the structure of magnetosheath jets
 400 using physical scales of the Earth’s magnetosphere. This detailed representation is obtained
 401 from the Amitis model, explained in Section 2. In our simulations, we use the typical solar
 402 wind plasma conditions near Earth and a range of IMF orientations, outlined in Table 1.
 403 The spatial and temporal scales of the magnetosphere are physically represented in our
 404 model, and no scaling has been applied in our simulations.

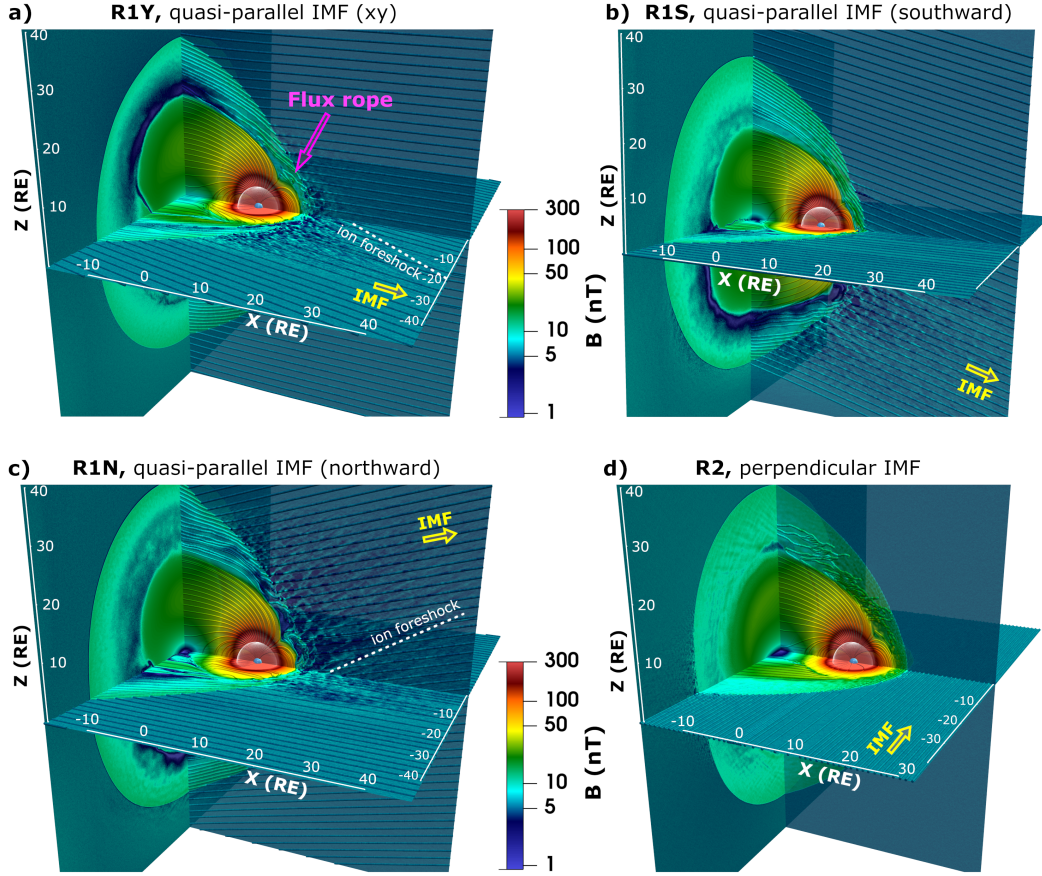


Figure 1. Time snapshot of the global, high-resolution, 3D structure of the solar wind interaction with Earth obtained from the Amitis hybrid model. The results are presented in the Geocentric Solar Magnetospheric (GSM) coordinate system for (a) a quasi-parallel IMF to the solar wind flow direction without any B_z component, i.e., run R1Y, (b) a quasi-parallel IMF with a southward component, i.e., run R1S, (c) a quasi-parallel IMF with a northward component, i.e., run R1N, and (d) a perpendicular IMF where only the B_y is non-zero, i.e., run R2. Note that the term “quasi-parallel” here refers to the orientation of the IMF with respect to the upstream solar wind plasma flow direction. The solar wind flows along the $-x$ axis. All simulation parameters are summarized in Table 1 and explained in Section 2. The background color shows the magnitude of the magnetic field in logarithmic scale in the xy (equatorial) plane at $z = 0$, the xz (mid-night meridian) plane at $y = 0$, and the yz plane at $x \approx -18.5 R_E$ in all panels. Streamlines shown in a few planes are magnetic field line tracing at that corresponding plane. For visualization purposes of the streamlines, we set the third component of the magnetic field to zero. The yellow arrows show the IMF orientation at each panel. The pink arrow in Figure 1a points to a flux rope in the magnetosheath over the northern cusp. Earth is shown by a small blue sphere, centered at the origin of the coordinate system, surrounded by a transparent sphere of radius $4.7 R_E$, indicating the inner boundary of our simulations. The dashed white lines in Figures 1a and 1c are parallel to the ion foreshock boundaries, shown to guide the eyes, indicating the ion foreshock boundary is not aligned with the IMF. See Movies S4 and S5 in the supplementary materials for the time evolution

3.1 Global 3D Structure of Earth’s Magnetosphere

First, we present the global, high-resolution, 3D kinetic interaction between the solar wind and Earth for various IMF configurations, showing our model correctly captures the physics of the interaction. Figure 1 presents a time-snapshot of the magnetic field obtained from our model for four distinct IMF configurations listed in Table 1: run R1Y for a quasi-parallel IMF to the solar wind flow without any B_z component (Figure 1a), runs R1S and R1N for a quasi-parallel IMF to the solar wind flow with a southward and northward component, respectively (Figures 1b and 1c), and run R2 for a perpendicular IMF to the solar wind flow (Figure 1d). Runs R1Y, R1S, and R1N are part of the same simulation sequence where the IMF orientation changes, as explained in Section 2. Note that the term “quasi-parallel” here refers to the orientation of the IMF with respect to the upstream solar wind flow and not the bow shock normal.

In addition to the global structure of the magnetosphere, one notable characteristic observed in Figures 1a–1c is the presence of a foreshock preceding the bow shock when the IMF is quasi-parallel to the solar wind (i.e., R1 simulation series). As marked in Figures 1a and 1c, the ion foreshock does not align with the IMF and instead, it remains behind the tangent field line, which is consistent with foreshock ion observations (Russell & Hoppe, 1983; Eastwood et al., 2005). However, when the IMF is perpendicular to the solar wind flow (Figure 1d), no foreshock is observed upstream of the bow shock. Instead, disturbances associated with the quasi-parallel shock are evident far downstream in the yz plane at $x \approx -18.5 R_E$ and $y < -30 R_E$ (see the yz plane in Figure 1d).

Our simulations, consistent with observations, suggest that the size of the magnetosheath is primarily influenced by the dynamic pressure of the solar wind and the angle between the IMF and the Sun-Earth line. When the IMF is aligned with the Sun-Earth line (parallel or antiparallel), the sub-solar bow shock gets highly disturbed and mixed into the foreshock, and consequently, the sub-solar magnetosheath region gets narrower (i.e., R1 series). Conversely, when the IMF is oriented at an oblique angle to the solar wind, the bow shock forms a well-confined boundary and the sub-solar magnetosheath region becomes thicker (i.e., run R2) compared to the quasi-parallel configurations.

Despite noticeable differences in the magnetic field structures presented in various panels in Figure 1, consistent features are visible in all panels, irrespective of the IMF configuration. These features include the collisionless bow shock, magnetopause, funnel-shaped

437 magnetospheric cusps, and elongated magnetotail. Other fundamental magnetospheric phe-
 438 nomena (e.g., a flux rope over the dayside northern cusp in the magnetosheath at approxi-
 439 mately $(+7.5, 0.0, +7.5) R_E$, marked with a pink arrow in Figure 1a and Kelvin-Helmholtz-
 440 like vortices marked in Figures S1a and S2e in the supplementary materials) have also been
 441 observed in our simulations, but analyzing them is beyond the scope of this study. In gen-
 442 eral, Figure 1 indicates that our simulations provide a reasonable representation of the solar
 443 wind plasma interaction with Earth.

444 3.2 Magnetosheath Jets

445 Here, we focus on the magnetosheath jets and present their morphology for different
 446 IMF configurations. In Figure 2a, we present plasma dynamic pressure, P_{dyn} , normalized
 447 to the upstream solar wind dynamic pressure, $P_{\text{sw}} = 1.86 \text{ nPa}$, in the equatorial (xy) plane
 448 at $z = 0$ for the R1Y simulation run (i.e., a quasi-parallel IMF to the solar wind flow
 449 with $B_z = 0$). The solid black contour lines in this Figure are obtained from the Plaschke
 450 criterion, highlighting $P_{\text{dyn},x} = 0.5 P_{\text{sw}}$. Additionally, we project the field-aligned current
 451 density, FAC, onto the inner boundary of our simulation at $4.7 R_E$. Different FAC regions are
 452 evident in Figure 2a, and their structure and current intensity are consistent with previous
 453 observations (Milan et al., 2017; Ganushkina et al., 2018). (See Movies S1 and S2 in the
 454 supplementary materials where we have shown the time evolution of the FACs as well as
 455 the plasma flux precipitation into the inner boundary of our simulations).

456 Our simulation presented in Figure 2a shows that the dynamic pressure is spatially
 457 variable in the foreshock region, ranging between $0.05 P_{\text{sw}}$ and $1.65 P_{\text{sw}}$ with the mean value
 458 of $0.95 P_{\text{sw}}$ and standard deviation of $0.18 P_{\text{sw}}$. For visualization purposes, we set the color
 459 bar range for the dynamic pressure between $0.083 P_{\text{sw}}$ and $3.0 P_{\text{sw}}$, centered at $0.5 P_{\text{sw}}$ (i.e.,
 460 the Plaschke criterion explained in Section 2.3), while the local minimum and maximum
 461 values in our presented simulation results are $4.0 \times 10^{-4} P_{\text{sw}}$ and $3.77 P_{\text{sw}}$, respectively. We
 462 see from Figure 2a that in some places in the magnetosheath, the dynamic pressure reaches
 463 nearly twice the upstream solar wind dynamic pressure and it gets higher than $3.0 P_{\text{sw}}$ near
 464 the magnetospheric flanks. At the sub-solar region, a few magnetosheath jets with localized
 465 high dynamic pressure are apparent.

466 For better visualization, Figure 2b provides a closer view of the upstream magne-
 467 tosheath region, where the presence of high dynamic pressure jets becomes evident. In

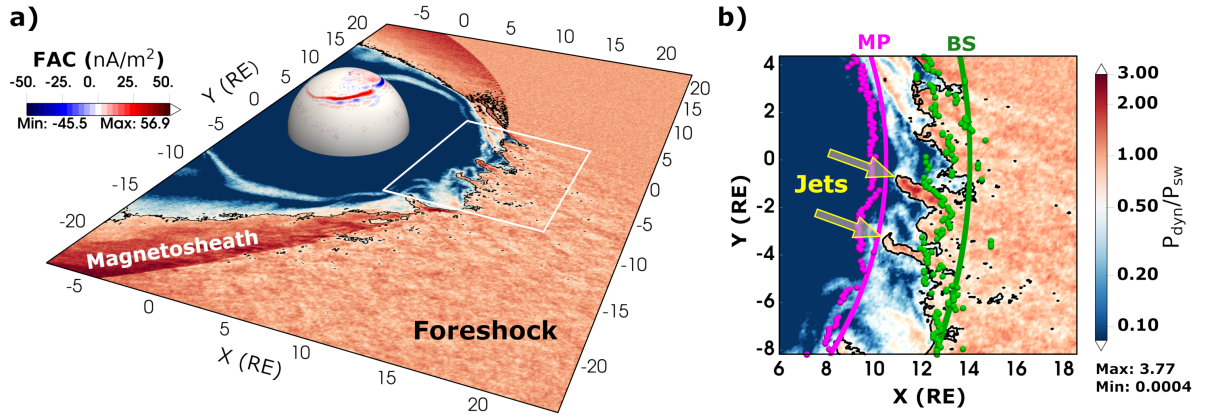


Figure 2. Amiris hybrid simulation results presented in the GSM coordinate system for the R1Y simulation at time $t = 744$ s in the xy (equatorial) plane at $z = 0$. (a) Plasma dynamic pressure in logarithmic scale, normalized to the upstream solar wind dynamic pressure, $P_{sw} = 1.86$ nPa. The sphere centered at the origin of the coordinate system represents the inner boundary of our simulations at $4.7 R_E$ with a projected intensity of the field-aligned current (FAC). The solid black contour lines show $P_{dyn,x} = 0.5 P_{sw}$, i.e., the Plaschke criterion for identifying magnetosheath jets, explained in Section 2. (b) A zoomed-in region from the highlighted area with the white rectangle in panel a shows the normalized plasma dynamic pressure with two marked magnetosheath jets. The pink and green dots denote, respectively, the magnetopause (MP) and bow shock (BS) boundaries estimated from our simulations. The selection criteria for the MP and BS boundaries are explained in Section 2.4. The solid pink and green lines mark the corresponding boundaries obtained from the empirical model by Chao et al. (2002) for the plasma parameters applied in our simulations and listed in Table 1.

468 this figure, similar to Figure 2a, the black contour lines highlight $P_{\text{dyn},x} = 0.5 P_{\text{sw}}$, i.e.,
 469 the Plaschke criterion for identifying magnetosheath jets. Two jets with apparent classical
 470 “cylinder-like” (or finger-like) structures are marked with arrows, displaying significantly
 471 higher dynamic pressure compared to their surrounding environment in the magnetosheath
 472 ($P_{\text{dyn}} \geq 0.5 P_{\text{sw}}$). In addition, the magnetopause and bow shock boundaries estimated from
 473 our simulations are shown, respectively, by the pink and green dots. Identifying the sub-
 474 solar bow shock boundary when the IMF is quasi-parallel to the solar wind flow presents a
 475 non-trivial task due to the influence of the foreshock disturbances. The bow shock boundary
 476 obtained from our simulations (green dots) stands slightly closer to Earth compared to the
 477 bow shock location estimated by Chao et al.’s empirical model for the bow shock (Chao et
 478 al., 2002), illustrated by the solid green curve. However, the magnetopause boundary yields
 479 a better agreement between our simulations (pink dots) and Chao’s empirical model for the
 480 magnetopause (solid pink curve).

481 To further investigate the characteristics of the jets, Figure 3 shows the detailed electro-
 482 magnetic and plasma environment obtained from our hybrid simulations, presented in the
 483 same format as that shown in Figure 2b. We see the plasma density inside jets (especially
 484 in the one closer to $y = 0$) is significantly higher compared to the density in the ambient
 485 magnetosheath and in the upstream solar wind (Figure 3a). However, as later shown, this
 486 is not necessarily valid for all jets, which is consistent with previous observations (Archer
 487 & Horbury, 2013; Karlsson et al., 2015; Plaschke et al., 2018). The overall speed of the
 488 plasma flow in the jets is approximately half of the upstream solar wind speed, and over two
 489 times larger than the average plasma speed in the surrounding magnetosheath (Figure 3b).
 490 For example, the averaged plasma speed of the jet closer to $y = 0$ is ~ 250 km/s, which
 491 is nearly 65% of the solar wind speed. However, as shown in Figure 3c, the surrounding
 492 environment of both highlighted jets has a sunward flow motion with v_x exceeding $0.15 v_{\text{sw}}$
 493 (i.e., 60 km/s moving sunward along the $+x$ axis). Similar sunward flow motion has been
 494 previously observed in both spacecraft data and numerical simulations (Shue et al., 2009;
 495 Plaschke et al., 2017; Guo et al., 2022).

496 The proton flux within both jets exceeds 170% of the upstream solar wind flux (Fig-
 497 ure 3d). In addition, at the time snapshot these results are taken, both jets advance towards
 498 the magnetopause, shown by arrows in Figure 3d, extending predominantly in the same di-
 499 rection as the upstream solar wind with some deviations. Their extension in the flow-parallel
 500 direction surpasses their dimension in the flow-perpendicular direction, which agrees with

501 previous numerical simulations (Hao, Lembège, et al., 2016; Palmroth et al., 2018; Guo et
 502 al., 2022). Both jets span the distance from the bow shock to the magnetopause, creating a
 503 deformation to the magnetopause boundary, evident in the magnetopause current structure
 504 shown in Figure 3e. Furthermore, the magnetic environment inside the jets shows noticeable
 505 changes compared to their surrounding magnetic field in the magnetosheath. For example,
 506 the magnetic field strength in the jet located closer to $y = 0$ reaches around 18 nT, i.e., over
 507 3.5 times larger than the strength of the IMF (Figure 3f). More detailed structures of the
 508 plasma flow motion and magnetic field orientation are shown in Figure S1 in the supple-
 509 mentary materials. In addition, the time evolution of these jets and their incidence on the
 510 magnetopause are shown in Movies S1 and S2 as well as in Figure S2 in the supplementary
 511 materials.

512 3.3 The Third Dimension of the Jets

513 Up till here, we have presented two-dimensional (2D) views of the jet properties (Fig-
 514 ures 2 and 3) as obtained from the 2D cross-sections of our 3D simulation results, and we
 515 have shown that our results are consistent with earlier spacecraft observations (Němeček et
 516 al., 1998; Savin et al., 2008; Hietala et al., 2009; Karlsson et al., 2012; Archer & Horbury,
 517 2013; Hietala & Plaschke, 2013; Plaschke et al., 2013; Gunell et al., 2014; Gutynska et al.,
 518 2015; Plaschke et al., 2017, 2020; Goncharov et al., 2020; Raptis et al., 2020) and 2D kinetic
 519 simulations (Gutynska et al., 2015; Hao, Lembège, et al., 2016; Omidi et al., 2016; Palm-
 520 roth et al., 2018; Preisser et al., 2020; Palmroth et al., 2021; Suni et al., 2021; Guo et al.,
 521 2022). However, in the following, we will unveil the 3D structure of the jets by including the
 522 third dimension and hereby show that the structure and properties of jets are much more
 523 complicated than previously thought.

524 Figure 4 illustrates the configuration of the magnetosheath jets for the R1Y simulation
 525 run in the yz plane (perpendicular to the solar wind flow direction) at different distances
 526 from the center of Earth. Due to the geometry of these planes, the center of Figure 4a
 527 is closer to the sub-solar bow shock, and the center of Figure 4d is closer to the nose of
 528 the magnetopause. The black dots indicate the bow shock boundary obtained from our
 529 simulations, and the black solid contour lines highlight $P_{\text{dyn},x} = 0.5 P_{\text{sw}}$. As discussed
 530 earlier in Section 2, identifying the quasi-parallel shock (black dots scattered at $y < 0$ in all
 531 panels in Figure 4) is a non-trivial task, but the quasi-perpendicular bow shock boundary
 532 is well-preserved (black dots at $y > 0$ in all panels in Figure 4). The magnetosheath is

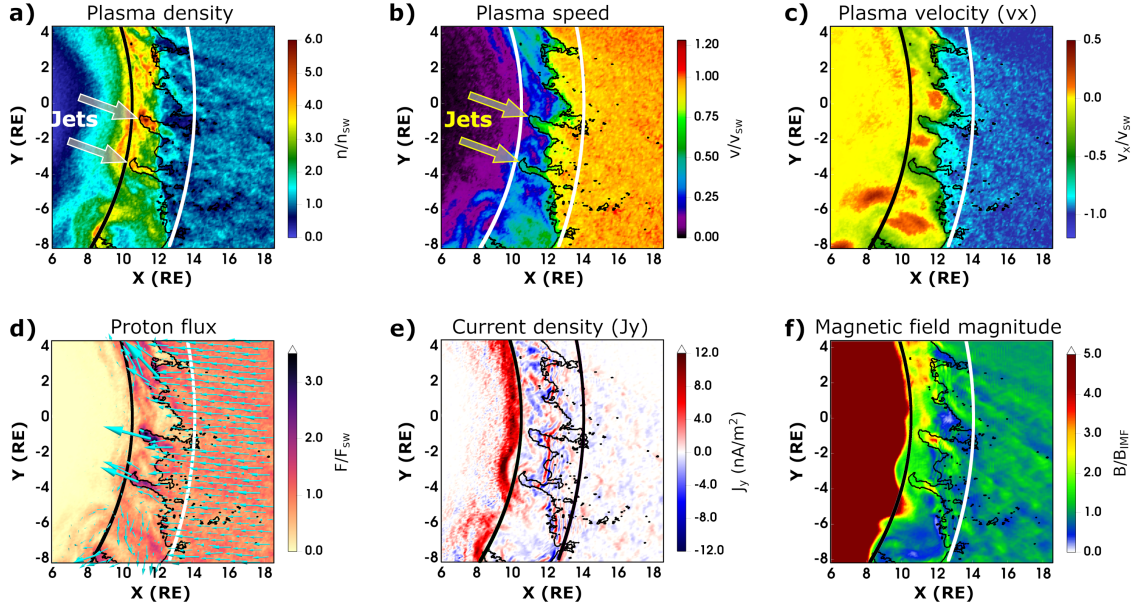


Figure 3. Hybrid simulation results for the R1Y simulation at time $t = 744$ s, presented in the same format as that shown in Figure 2b. (a) Proton density normalized to the upstream solar wind density, $n_{sw} = 7 \text{ cm}^{-3}$, (b) proton speed normalized to the upstream solar wind speed, $|v_{sw}| = 400 \text{ km/s}$, (c) normalized x -component of the proton velocity to the upstream solar wind speed where negative values show the anti-sunward and positive values show the sunward plasma motion, (d) proton flux normalized to the upstream solar wind flux, $F_{sw} = 2.8 \times 10^{12} \text{ m}^{-2} \text{ s}^{-1}$, and the colored arrows show the direction and magnitude of the proton flux, (e) the y -component of the electric current density, J_y , and (f) the magnitude of the magnetic field normalized to the strength of the IMF, $B_{IMF} = 5 \text{ nT}$. The arrows in Figures 3a and 3b mark the two magnetosheath jets highlighted in Figure 2. The inner and outer solid curves in all panels show, respectively, the magnetopause and bow shock boundaries obtained from the empirical model by Chao et al. (2002) for the plasma parameters applied to our simulations, listed in Table 1.

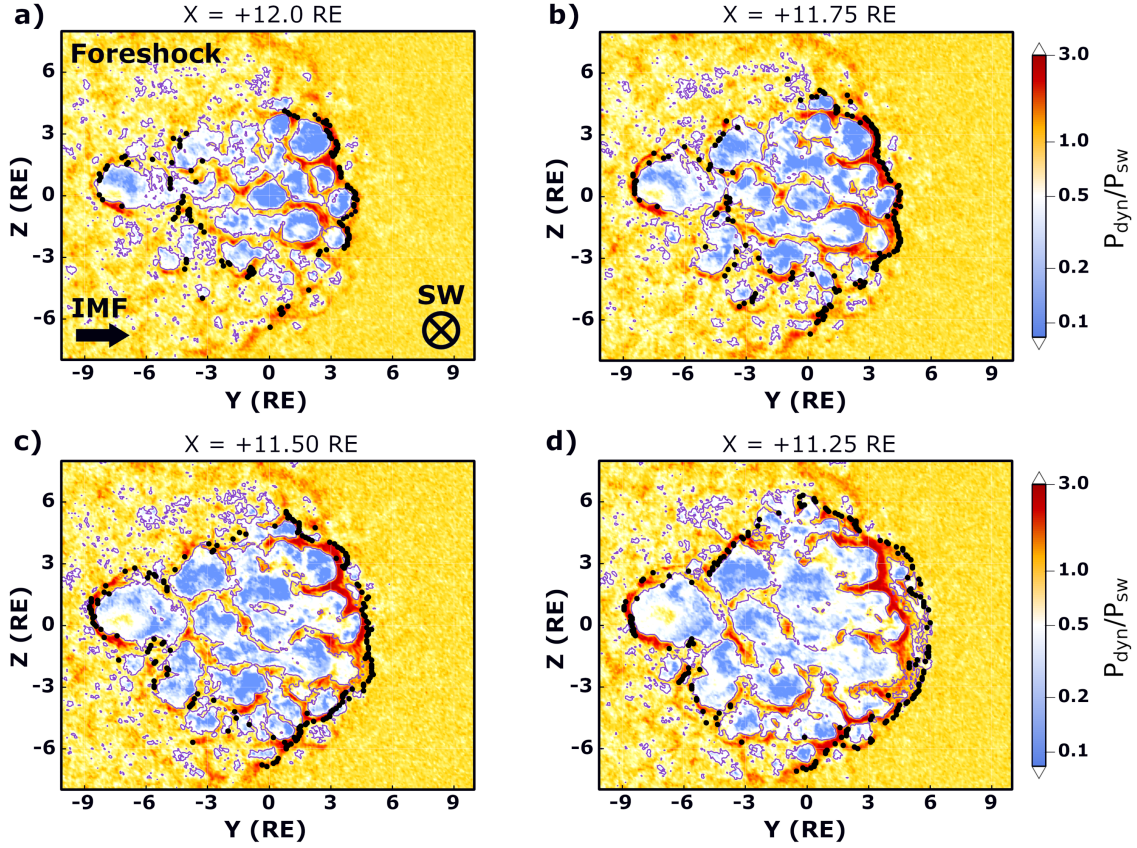


Figure 4. Amitis hybrid simulation results obtained from run R1Y at time $t = 744$ s in the GSM coordinate system, presenting the dynamic pressure normalized to the upstream solar wind dynamic pressure, $P_{sw} = 1.86$ nPa in the yz plane at different distances from the Earth's center: (a) $x = +12 R_E$, (b) $x = +11.75 R_E$, (c) $x = +11.5 R_E$, and (d) $x = +11.25 R_E$. The center of Figure 4a is closer to the sub-solar bow shock, and the center of Figure 4d is closer to the nose of the magnetopause. The black dots indicate the bow shock boundary obtained from our simulations, explained in Section 2. The magnetosheath is the area surrounded by the bow shock (black dots). The solid black contour lines highlight $P_{dyn,x} = 0.5 P_{sw}$ (i.e., the Plaschke criterion for identifying magnetosheath jets). The magnetosheath jets are all the **filamentary structures** with dynamic pressure larger than $0.5 P_{sw}$ in the magnetosheath (yellow and red in the figure). The Plaschke criterion is valid at the sub-solar region within an angle $< 30^\circ$ from the Earth-Sun line (Plaschke et al., 2013), which is nearly the entire magnetosheath region presented here. All panels are viewed from the Sun, and therefore, the solar wind flows into the planes. The direction of the upstream solar wind flow and the orientation of the undisturbed IMF are the same for all panels and marked by arrows in Figure 4a.

533 the region surrounded by the bow shock boundary. All the high-dynamic pressure regions
 534 ($\geq 0.5 P_{\text{sw}}$) with filamentary structures in the magnetosheath are jets (yellow and red color
 535 regions in the figure).

536 We present the findings in Figure 4 using simple 2D cross-sections of our simulations.
 537 Alternatively, Figure S3 in the supplementary text presents comparable results on a 3D
 538 curved representation of the magnetosheath. In Figure S3, the normalized dynamic pressure
 539 is mapped on a curved structure of the magnetosheath adjacent to the bow shock. Given
 540 the complexity of this geometry and the asymmetric nature of the magnetosheath structure,
 541 we present our simulation results exclusively on simple 2D flat plans, as shown in Figure 4.
 542 However, the overall structure of the jets presented in Figure 4 is similar to those shown in
 543 Figure S3.

544 Contrary to previous hypotheses regarding jet morphology (Archer et al., 2012; Karls-
 545 son et al., 2012; Plaschke et al., 2016, 2018; Palmroth et al., 2021; Plaschke et al., 2020;
 546 Goncharov et al., 2020; Guo et al., 2022), our 3D kinetic simulations demonstrate that the
 547 magnetosheath jets do not exhibit simple geometries like cylinders, spheres, or pancakes.
 548 Instead, their structure is exceedingly intricate and interconnected. At closer distances to
 549 the bow shock (e.g., Figures 4a and 4b), the jets appear as interconnected regions. Moving
 550 further downstream from the bow shock and getting closer to the magnetopause (e.g., Fig-
 551 ures 4c and 4d), the jets become increasingly fragmented and disconnected. The dynamic
 552 pressure inside the jets spans over a wide range from $\sim 0.5 P_{\text{sw}}$ to over $3.0 P_{\text{sw}}$ in the planes
 553 shown in Figure 4.

554 More detailed characteristics of the jets in the yz plane at $x = +11.5 R_E$ are shown
 555 in Figure 5. In general, we see from Figure 5 that the plasma density and velocity of
 556 the jets (filamentary structures in the figure) are considerably higher than the surrounding
 557 magnetosheath plasma. The time evolution of the jets in the yz plane at $x = +11.5 R_E$ for
 558 the R1Y simulation is shown in the Movie S3 in the supplementary materials.

559 The structure of the magnetosheath jets in the yz plane for the southward IMF config-
 560 uration (run R1S) is illustrated in Figure 6. In this simulation, both the magnetopause and
 561 bow shock are positioned closer to the planet under the southward IMF orientation, pri-
 562 marily due to magnetic reconnection eroding the dayside magnetosphere. This agrees with
 563 previous observations and numerical simulations (e.g., Aubry et al., 1970; Wiltberger et al.,
 564 2003; G. Le et al., 2016). Consequently, the planes shown in Figure 6 are located closer to

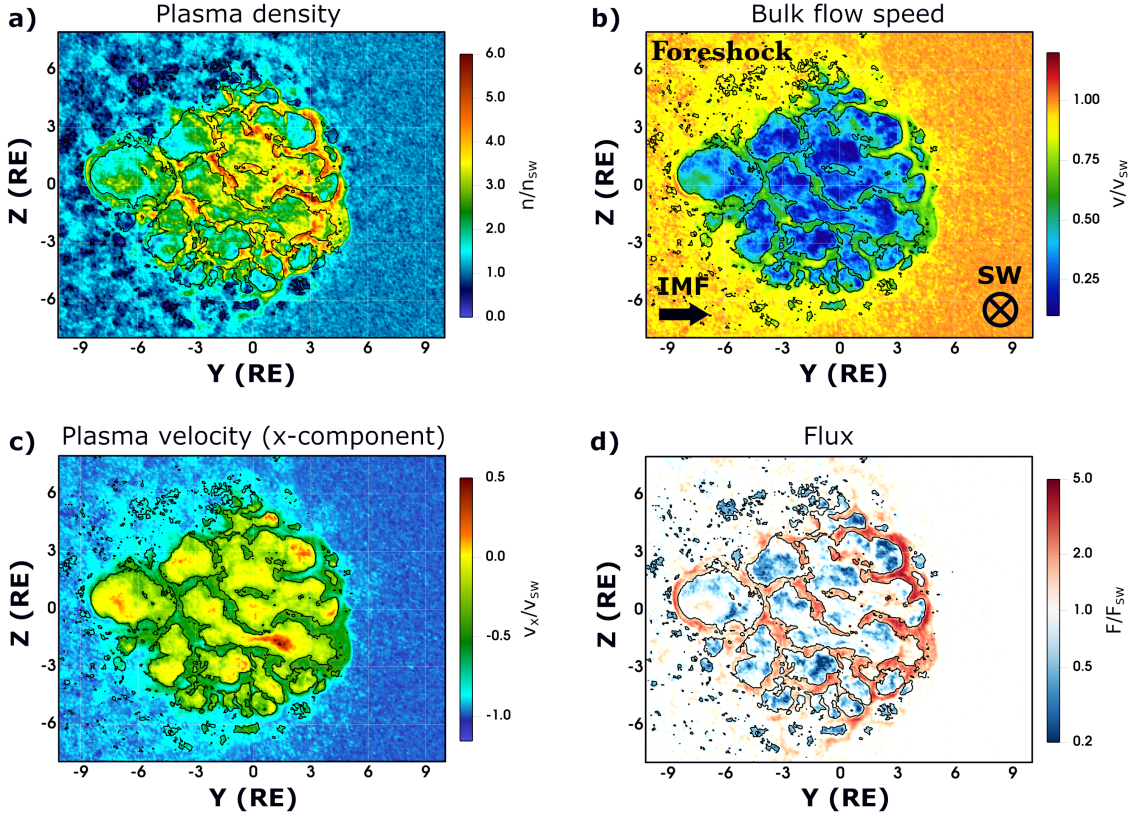


Figure 5. Hybrid simulation results obtained from the R1Y simulation run at time $t = 744$ s in the yz plane at $x = +11.5 R_E$. The geometry of the cuts is the same as those described in Figure 4. (a) Proton density normalized to the upstream solar wind density, $n_{sw} = 7 \text{ cm}^{-3}$, (b) proton bulk flow speed normalized to the upstream solar wind plasma speed, $v_{sw} = 400 \text{ km/s}$, (c) the x-component of the plasma velocity normalized to the upstream solar wind plasma speed, $v_{sw} = 400 \text{ km/s}$, and (d) the proton flux normalized to the upstream solar wind flux, $F_{sw} = 2.8 \times 10^{12} \text{ m}^{-2} \text{ s}^{-1}$. The black contour lines show where $P_{dyn,x} = 0.5 P_{sw}$. The jets are the filamentary structures in the magnetosheath, as described in Figure 4.

565 Earth compared to those shown in Figure 4. Similar to the results presented in Figure 4,
 566 the magnetosheath jets exhibit intricate interconnections and form a complex geometry,
 567 particularly in proximity to the bow shock (Figures 4a and 4b). In contrast to the results
 568 shown in Figure 4, we observe that jets during the southward IMF appear less fragmented,
 569 and spatially larger and more extended, which is associated with the IMF orientation that
 570 alters the physics of the interaction. However, we did not observe any noticeable differences
 571 in the average plasma dynamic pressure inside jets during the southward IMF compared to
 572 those presented earlier in Figure 4. A similar conclusion also holds for the northward IMF
 573 (see Figure S4 in the supplementary materials).

574 Similar to their structure, the evolution of jets is also complex and indeed a 3D problem.
 575 Figure 7 illustrates the angle between the local plasma flow and the upstream solar wind in
 576 the yz plane at $x = +11.5 R_E$, taken at different times from the R1Y simulation. In this
 577 figure, the zero degrees (white regions) mean the plasma flow direction is exactly parallel
 578 to the upstream solar wind (i.e., along the $-x$ axis). Angles between 0 and 90 degrees
 579 indicate an anti-sunward flow, and angles larger than 90 degrees show a sunward flow. In
 580 general, this figure shows how large the plasma flow direction deviates from the undisturbed
 581 solar wind flow direction in the shown planes. Similar to Figure 4, jets are the filamentary
 582 structures mainly clustered at the center of each panel (see Figure S5 in the supplementary
 583 materials for the time evolution of the dynamic pressure). Figure 7 indicates the dynamic
 584 movement of jets and underscores their lively environment in the yz plane. While the plasma
 585 flow motion within jets predominantly follows the solar wind flow direction with nearly 10°
 586 to 40° deviation (seen by the light blue regions in Figure 7), the low dynamic pressure
 587 regions encircling the jets in the magnetosheath move predominantly perpendicular to the
 588 solar wind and often sunward, which is consistent with previous findings (Shue et al., 2009;
 589 Plaschke et al., 2017; Guo et al., 2022).

590 As shown in Figure 7, the jets are highly dynamic, intermittently merging into and
 591 splitting from each other. For instance, let's consider a half-open loop jet positioned at
 592 $(y, z) \approx (+3, +2) R_E$, pointed to by an arrow in Figure 7a. This jet experiences a phase
 593 of closure to another jet after 24 seconds (Figure 7b). Subsequently, it reopens after 72
 594 seconds (Figure 7d) and then progresses towards the equatorial plane (Figures 7e and 7f).
 595 As shown previously in Figure 2, and also Figure S2 in the supplementary materials, these
 596 jets have a third dimension along the x axis, which makes their geometry not as simple as
 597 previously thought.

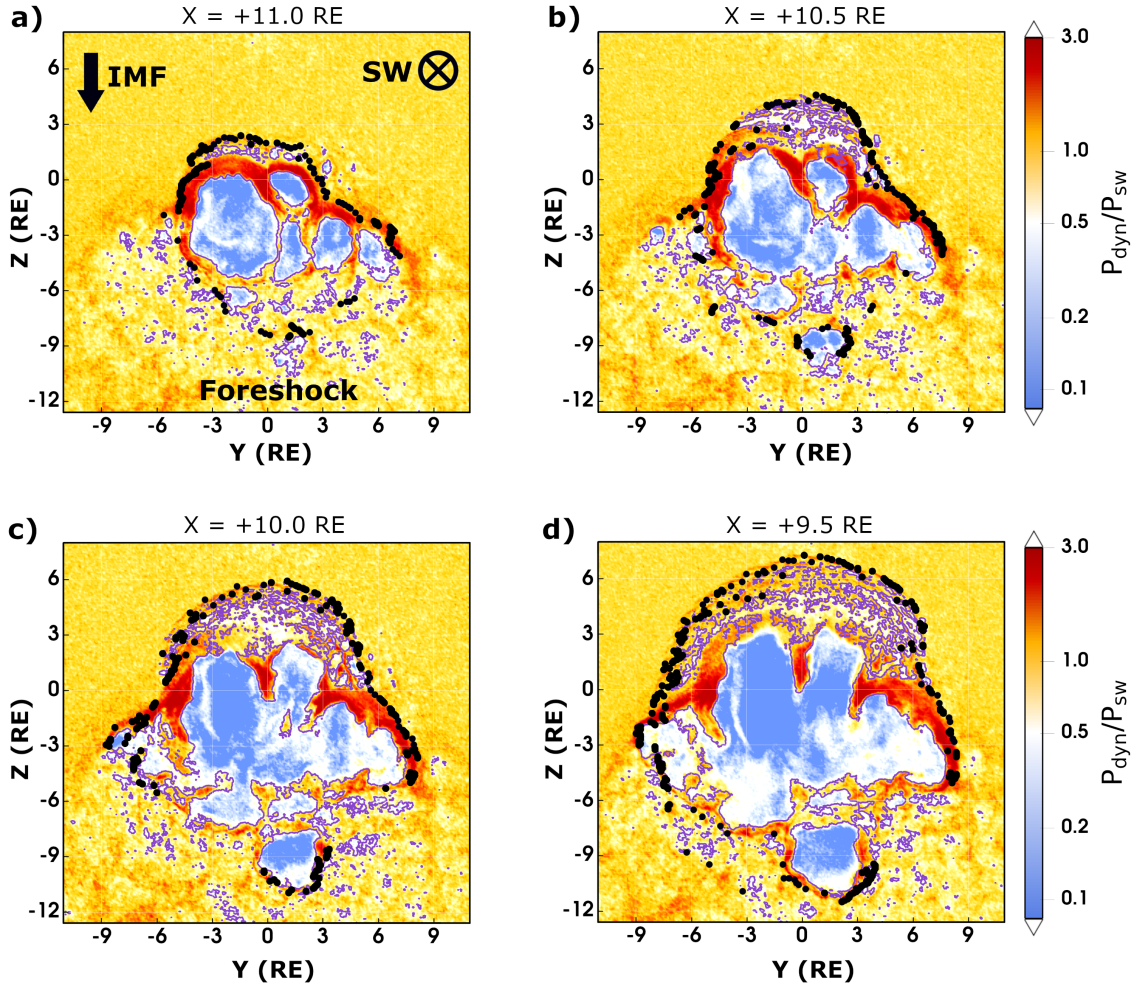


Figure 6. Hybrid simulation results obtained during the southward IMF (run R1S) at time $t = 2244$ s, presenting the dynamic pressure normalized to the upstream solar wind dynamic pressure, $P_{sw} = 1.86$ nPa in the yz plane at different distances from the Earth's center: (a) $x = +11.0 R_E$, (b) $x = +10.5 R_E$, (c) $x = +10.0 R_E$, and (d) $x = +9.5 R_E$. The figure format is the same as that shown in Figure 4.

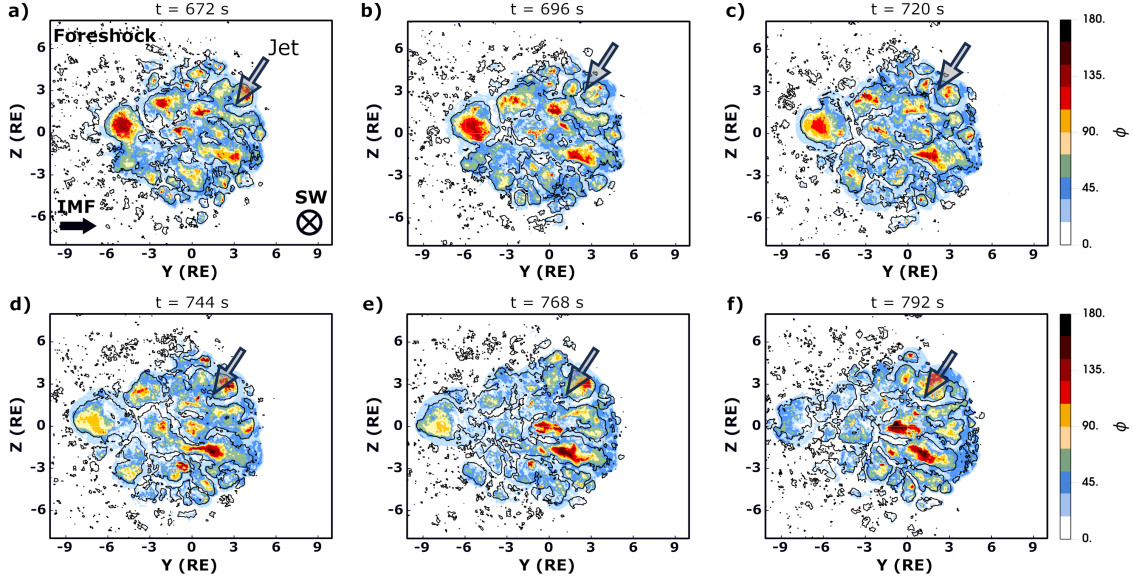


Figure 7. Hybrid simulation results obtained from run R1Y in the yz plane at $x = +11.5 R_E$ at six different simulation times: (a) 672 s, (b) 696 s, (c) 720 s, (d) 744 s, (e) 768 s, and (f) 792 s. The last panel is taken at nearly 400 s prior to the arrival of the southward magnetic transient from the R1S simulation. The background color illustrates the angle between the localized plasma flow direction and the upstream solar wind flow direction. The zero degree means exactly parallel flow to the solar wind (i.e., along the $-x$ axis). Angles between 0 and 90 degrees are anti-sunward flow, angles larger than 90 degrees mean sunward flow, and consequently, 180 degrees means perfectly anti-parallel to the solar wind flow direction (i.e., along the $+x$ axis). The jets are the filamentary structures, and they have a flow angle of less than ~ 40 degrees (light-blue colors). The black arrow in each panel points to one of the magnetosheath jets that gets connected to its neighboring jets at time 696 s and then gets disconnected again at time 744 s (see the text for more detail). The figure format is the same as that shown in Figure 4.

598 Consistent with previous observations, our simulations indicate that the low IMF cone
 599 angles relative to the solar wind flow direction are favorable for the generation of magne-
 600 tosheath jets downstream of the quasi-parallel shock in the sub-solar region (i.e., where the
 601 local bow shock normal is quasi-parallel to the IMF) (Archer & Horbury, 2013; Plaschke
 602 et al., 2013, 2018). In the case of run R2 (i.e., a perpendicular IMF to the solar wind
 603 flow), we did not observe jets in the sub-solar region. Instead, as shown in Figure S6 in
 604 the supplementary materials, jet-like structures with various scales manifest downstream of
 605 the quasi-perpendicular shock at the magnetosheath flanks, marked with the white arrow in
 606 Figure S6. This finding is in agreement with some of the earlier observations (e.g., Archer &
 607 Horbury, 2013). Recent studies, however, have suggested that the jets observed downstream
 608 of the quasi-perpendicular shock are originally forming at the quasi-parallel shock and later
 609 transported downstream of the quasi-perpendicular shock (Raptis et al., 2020; Kajdič et
 610 al., 2021). While our preliminary analyses using our simulations (not shown here) do not
 611 support this idea, investigating the nature of the jets downstream of quasi-perpendicular
 612 shocks requires a separate study.

613 3.4 Stationary Virtual Spacecraft Observations

614 To further investigate the characteristics of jets in our model, we placed two stationary
 615 virtual observers in our simulations at two distinct locations within the magnetosheath,
 616 mimicking spacecraft observations. The first observer is positioned downstream near the
 617 nose of the bow shock at $(+11.5, 0.0, -1.0) R_E$, and the second observer is located in prox-
 618 imity to the magnetopause at $(+10.0, 0.0, +3.5) R_E$. The time series for various parameters
 619 derived from our kinetic simulations are shown in Figure 8. In addition to these two ob-
 620 servers in the magnetosheath, we also placed one virtual observer as a reference point in the
 621 solar wind and far away from any terrestrial disturbances. The results from this observer
 622 are presented in Figure S7 in the supplementary materials.

623 The first 7.5 minutes of our simulations are highlighted as the “development phase” in
 624 Figure 8. This is the minimum time required for the dayside magnetosphere to be developed
 625 in our experiments during the nominal solar wind conditions at Earth (see Movies S4 and S5
 626 in the supplementary materials). Subsequently, the magnetosphere attains a more developed
 627 state, and the simulation results reach a steady state. To introduce perturbations into the
 628 system, a magnetic transient in the form of a current sheet is applied upstream of our
 629 simulations (see Section 2 for more detail and also see time 12:30 in Figure S7d in the

630 supplementary materials). This magnetic transient arrives to the first observer at time
 631 $\sim 22:00$, and to the second observer around $23:00$. These instances of the magnetic transient
 632 are highlighted in red in Figure 8. Prior to the arrival of the magnetic transient and after
 633 its passage, the solar wind parameters, and magnetic field configurations remained constant
 634 upstream of our simulation domain, indicating a relatively constant environment in terms
 635 of solar wind conditions and magnetic field configurations for over 10 minutes.

636 In Figures 8a and 8f, the proton dynamic pressure, $P_{\text{dyn}} = mn\mathbf{v}^2$, is shown by the
 637 solid black line, where m represents the proton mass, n is the plasma density, and \mathbf{v} is
 638 the plasma flow velocity. The proton dynamic pressure along the solar wind flow direction,
 639 denoted as $P_{\text{dyn},x} = mnv_x^2$, is shown by the solid red line, where v_x is the x -component
 640 of the plasma flow velocity. The dashed horizontal line indicates the upstream solar wind
 641 dynamic pressure (1.86 nPa) and the dash-dotted horizontal line indicates half of the solar
 642 wind dynamic pressure (0.93 nPa). According to the Plaschke criterion, the observed feature
 643 with $P_{\text{dyn},x} \geq 0.93$ nPa are jets. In approximately 30 minutes after the development phase,
 644 we observed many jets passing through both observers in our simulations, some of them are
 645 labeled with numbers in the top panels in Figure 8. The identified jets vary in duration,
 646 ranging from a few seconds (e.g., jets #1, #6, and #9) to several minutes (e.g., jets #7,
 647 #8, and #10).

648 Nevertheless, it is essential to recognize that the intricate 3D structure of the jets,
 649 as obtained from our simulation results (illustrated in Figures 2–7 and the accompanying
 650 supplementary movies), indicates that some of the identified jets in Figure 8 could be com-
 651 ponents of the same jet. These components may undergo fragmentation and recombination,
 652 and appear as seemingly a new jet at later times in the “1D view” presented in Figure 8.
 653 This statement also holds for the previous spacecraft observations of magnetosheath jets.

654 Comparing Figure 8a with Figure 8f, we observe more jets near the bow shock than near
 655 the magnetopause, which is consistent with previous observations (Archer & Horbury, 2013;
 656 Plaschke et al., 2013; Goncharov et al., 2020). In addition, our simulations demonstrate that
 657 jets can form during stable IMF configurations, which confirms earlier observations that did
 658 not directly relate the formation of the jets to magnetic transients (Archer & Horbury, 2013;
 659 Plaschke et al., 2013). For example, all labeled jets, except #5, formed during a constant
 660 and stable IMF. During the transient event, however, we also observe the passage of a jet
 661 through the first observer near the bow shock (i.e., jet #5), which may or may not have

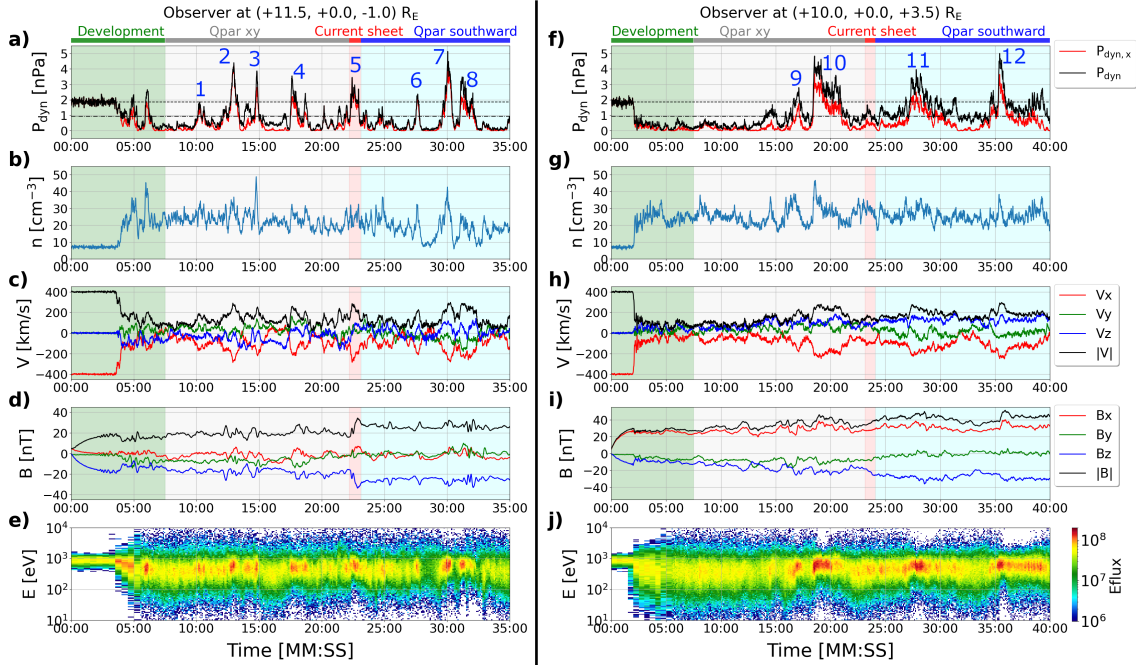


Figure 8. The temporal evolution of various quantities examined at the position of two stationary virtual observers located within the magnetosheath in our hybrid simulations: (a–e) results at the first observer located downstream of the bow shock at $(+11.5, 0.0, -1.0) R_E$, and (f–j) results at the second observer positioned upstream of the magnetopause at $(+10.0, 0.0, +3.5) R_E$. (a, f) Proton dynamic pressure, $P_{\text{dyn}} = mn_{\text{sw}}\mathbf{v}^2$, is shown by the solid black line, and the proton dynamic pressure along the solar wind flow direction, denoted as $P_{\text{dyn},x} = mn_{\text{sw}}v_x^2$, is shown in red. The dashed horizontal line shows the upstream solar wind dynamic pressure, 1.86 nPa, and the dash-dotted horizontal line marks half of the solar wind dynamic pressure, 0.93 nPa. Several magnetosheath jets, where their $P_{\text{dyn},x} \geq 0.93 \text{ nPa}$ are labeled with numbers. (b, g) Proton density, (c, h) three components of the proton velocity, (d, i) three components of the magnetic field, and (e, j) differential proton energy flux (“Eflux”) as a function of energy and time. The initial phase of the magnetosphere development in our model is highlighted in green (i.e., the first 7.5 minutes). Subsequently, the IMF aligns quasi-parallel to the solar wind flow in the xy plane (run R1Y). After approximately 22 minutes the current sheet reaches the first observer, and nearly one minute later it arrives at the second observer. After this, the IMF exhibits a southward orientation for more than 15 minutes (run R1S). The period encompasses both the R1Y and R1S simulations, during which a current sheet (magnetic transient) traverses Earth’s magnetosphere is highlighted in red. Also, see Figure S7 in the supplementary materials for the upstream observer.

662 been formed by the transient event. Investigating the formation mechanism of the jets is
 663 beyond the topic of this research and will be conducted in a separate study.

664 Noteworthy characteristics of jets can be seen in the second and third rows in Figure 8.
 665 Consistent with previous observations (Archer & Horbury, 2013; Plaschke et al., 2018), some
 666 jets exhibit a substantial rise in plasma density (e.g., jets #3, #7, and #10), while others
 667 do not display significant changes (e.g., jets #2, #4 and #11). However, all identified jets
 668 shown in Figure 8 demonstrate a substantial increase in their flow velocity. In particular,
 669 the x -component of velocity during the passage of nearly all jets, as shown by the red lines
 670 in Figures 8c and 8h, reaches ~ 200 km/s and beyond, which aligns with earlier observations
 671 (Archer & Horbury, 2013; Plaschke et al., 2013; Gunell et al., 2014; Karlsson et al., 2015).
 672 Furthermore, Figures 8d and 8i illustrate magnetic field variations, which may be associated
 673 with jets, as observed in spacecraft data (Plaschke et al., 2020). However, we collected the
 674 simulated magnetic field data at the location of our virtual observers with a frequency of
 675 0.33 Hz, which is not high enough to pursue wave analysis. The energetic behavior of jets can
 676 also be distinguished in the energy-time spectrogram obtained from our kinetic simulations,
 677 shown in Figures 8e and 8j. Consistent with previous spacecraft observations (Hietala et
 678 al., 2009; Archer et al., 2012; Archer & Horbury, 2013; Plaschke et al., 2013; Dmitriev &
 679 Suvorova, 2012; Plaschke et al., 2018; Raptis, Karlsson, Vaivads, Lindberg, et al., 2022),
 680 the identified jets in our simulations exhibit a higher energy flux and lower plasma heating
 681 compared to the classical structure of the magnetosheath plasma without jets.

682 4 Discussion and Conclusions

683 We present the first 3D, global, hybrid-kinetic plasma interaction between the solar wind
 684 plasma and Earth's magnetosphere at its physical scales using Amitis, a high-performance
 685 GPU-based hybrid-kinetic plasma framework (Fatemi et al., 2017). While MHD models
 686 have been extensively applied for decades to study the solar wind interaction with Earth
 687 (e.g., Den et al., 2006; Lopez et al., 2011), the kinetic nature of the interaction, for example,
 688 the formation of an extensive foreshock during quasi-parallel IMF configurations cannot be
 689 explained by MHD models. Moreover, earlier kinetic simulations applied to this problem are
 690 either 2D models (e.g., Hao, Lembège, et al., 2016; Omid et al., 2016; Palmroth et al., 2018;
 691 Suni et al., 2021; Guo et al., 2022) and/or have scaled down the size of the magnetosphere
 692 or the solar wind parameters to reduce the computational costs (e.g., Karimabadi et al.,
 693 2014; Omid et al., 2016; Ng et al., 2021; Omelchenko et al., 2021).

694 In addition, we present the first 3D structure of magnetosheath jets. Consistent with
695 previous observations and numerical simulations, we show that magnetosheath jets appear
696 during stable IMF configurations, and therefore, should not be merely related to transient
697 events in the solar wind. In contrast to earlier findings and analyses, our investigation
698 demonstrates that these jets do not have a simple geometry like a cylinder, sphere, or
699 pancake. Instead, they exhibit a complex 3D and dynamic structure, interlinked in a highly
700 intricate manner. They repeatedly merge into and split from each other, encompassing a
701 broad spectrum of dimensions, and reach the magnetopause over a spatially large area (see
702 Movie S1, S2, and S3 in the supplementary materials for more details).

703 Previous 2D simulations of the magnetosheath jets (Gutynska et al., 2015; Hao, Lembège,
704 et al., 2016; Palmroth et al., 2018; Preisser et al., 2020; Palmroth et al., 2021; Suni et al.,
705 2021; Guo et al., 2022) may provide a misleading impression of the structure, size, and time-
706 evolution of jets due to their 2D perspective and the lack of the third dimension. Moreover,
707 3D simulations without realistic scales for Earth (Omelchenko et al., 2021) did not yield
708 definitive findings concerning the morphology of jets, primarily due to scaling factors ap-
709 plied to the size of Earth and/or the strength of Earth’s magnetic dipole. However, our
710 simulations with physical scaling of Earth’s magnetosphere reveal that jets are intricate,
711 dynamic, and indeed, 3D structures.

712 By analyzing the results from our single-point measurements, presented in Figure 8,
713 we lack additional information about the 3D spatial arrangement of jets. This arrangement
714 resembles spacecraft observations that probe only a small spatial area at once, and therefore,
715 provide a limited “1D snapshot” view of jets. Consequently, by using the spacecraft data
716 we cannot definitively determine if the observed jets are numerous individual entities, or
717 if they are fewer in number with some being components of an interconnected structure,
718 akin to the examples illustrated in Figures 4–7. This indicates the significance of utilizing
719 3D kinetic simulations for the magnetosphere to comprehensively explore the morphology
720 of the jets.

721 Through the exploration of the 3D structure of magnetosheath jets, we can improve our
722 knowledge of the Earth’s magnetosphere and its interaction with the solar wind. In addition,
723 recent studies have provided compelling evidence for the formation of magnetosheath jets in
724 planetary magnetospheres beyond our own (Gunell et al., 2023). Therefore, our research not
725 only advances our understanding of magnetosheath jets within the magnetosphere of Earth

726 but also offers valuable insights into analogous phenomena occurring in other planetary
727 magnetospheres. This can open new windows for comparative planetary research.

728 **Open Research Section**

729 All the simulation data presented in this manuscript is archived at Zenodo, and publicly
730 accessible via <https://doi.org/10.5281/zenodo.8421137>.

731 **Acknowledgments**

732
733 **Funding:** The authors acknowledge financial support from the Swedish National Space
734 Agency (SNSA) grant 2022-00138. S.F. also acknowledges financial support from SNSA
735 grant 115/18, the Swedish Research Council (VR) grant 2018-03454, and Nvidia’s Academic
736 Hardware Program, grant RTX-A6000. M.H. & E.K. also acknowledge financial support
737 from VR grant 2018-03623.

738 **Computation resources:** The computations were primarily enabled by the Berzelius
739 resource provided by the Knut and Alice Wallenberg Foundation (KAW) at the National
740 Supercomputer Centre (NSC), Linköping, Sweden. They were partly conducted through
741 computation and data storage resources at the High Performance Computing Center North
742 (HPC2N), Umeå University, Sweden, and partly through infrastructure and hardware grants
743 awarded through “Kempestiftelserna” and “medeldyrutrustning” at Umeå University, Swe-
744 den. S.F. acknowledges Prof. Paolo Bientinesi, Mr. Åke Sandgren, and Mr. Björn Torkels-
745 son at HPC2N for their unconditional support and assistance in providing hardware for
746 running the Amitis code on the Kebnekaise supercomputer.

747 **Author contributions:** S.F. is the developer of the Amitis code, planned and ran
748 all the simulations, performed the analyses, made the figures, and wrote the first draft of
749 the paper. S.F. and E.K. developed the post-processing and visualization tools for Amitis
750 simulations. All authors contributed to the discussions and interpretation of the results and
751 improvement of the analyses. They also contributed to editing and improving the text of
752 this manuscript.

753 **References**

754 Aizawa, S., Griton, L. S., Fatemi, S., Exner, W., Deca, J., Pantellini, F., ... others

- 755 (2021). Cross-comparison of global simulation models applied to mercury's day-
756 side magnetosphere. *Planetary and Space Science*, *198*, 105176. Retrieved from
757 <https://doi.org/10.1016/j.pss.2021.105176>
- 758 Archer, M. O., & Horbury, T. S. (2013). Magnetosheath dynamic pressure enhancements:
759 Occurrence and typical properties. *Annales Geophysicae*, *31*(2), 319–331. Retrieved
760 from <https://doi.org/10.5194/angeo-31-319-2013>
- 761 Archer, M. O., Horbury, T. S., & Eastwood, J. P. (2012). Magnetosheath pressure pulses:
762 Generation downstream of the bow shock from solar wind discontinuities. *Journal of*
763 *Geophysical Research: Space Physics*, *117*(A5). Retrieved from [https://doi.org/](https://doi.org/10.1029/2011JA017468)
764 [10.1029/2011JA017468](https://doi.org/10.1029/2011JA017468)
- 765 Aubry, M. P., Russell, C. T., & Kivelson, M. G. (1970). Inward motion of the magnetopause
766 before a substorm. *Journal of Geophysical Research*, *75*(34), 7018–7031. Retrieved
767 from <https://doi.org/10.1029/JA075i034p07018>
- 768 Bame, S. J., Asbridge, J. R., Hundhausen, A. J., & Montgomery, M. D. (1970). Solar
769 wind ions: 56fe+8 to 56fe+12, 28si+7, 28si+8, 28si+9, and 16o+6. *Journal of Geo-*
770 *physical Research*, *75*(31), 6360–6365. Retrieved from [https://doi.org/10.1029/](https://doi.org/10.1029/JA075i031p06360)
771 [JA075i031p06360](https://doi.org/10.1029/JA075i031p06360)
- 772 Bochsler, P. (2007). Minor ions in the solar wind. *The Astronomy and Astrophysics Review*,
773 *14*, 1–40. Retrieved from <https://doi.org/10.1007/s00159-006-0002-x>
- 774 Brain, D., Barabash, S., Boesswetter, A., Bougher, S., Brecht, S., Chanteur, G., ... others
775 (2010). A comparison of global models for the solar wind interaction with mars.
776 *Icarus*, *206*(1), 139–151. Retrieved from [https://doi.org/10.1016/j.icarus.2009](https://doi.org/10.1016/j.icarus.2009.06.030)
777 [.06.030](https://doi.org/10.1016/j.icarus.2009.06.030)
- 778 Chao, J. K., Wu, D. J., Lin, C.-H., Yang, Y.-H., Wang, X. Y., Kessel, M., ... Lepping,
779 R. P. (2002). Models for the size and shape of the earth's magnetopause and bow
780 shock. In *Cospar colloquia series* (Vol. 12, pp. 127–135). Retrieved from [https://](https://doi.org/10.1016/S0964-2749(02)80212-8)
781 [doi.org/10.1016/S0964-2749\(02\)80212-8](https://doi.org/10.1016/S0964-2749(02)80212-8)
- 782 Den, M., Tanaka, T., Fujita, S., Obara, T., Shimazu, H., Amo, H., ... others (2006).
783 Real-time earth magnetosphere simulator with three-dimensional magnetohydrody-
784 namic code. *Space Weather*, *4*(6). Retrieved from [https://doi.org/10.1029/](https://doi.org/10.1029/2004SW000100)
785 [2004SW000100](https://doi.org/10.1029/2004SW000100)
- 786 Dmitriev, A. V., & Suvorova, A. V. (2012). Traveling magnetopause distortion related
787 to a large-scale magnetosheath plasma jet: Themis and ground-based observations.

- 788 *Journal of Geophysical Research: Space Physics*, 117(A8). Retrieved from [https://](https://doi.org/10.1029/2011JA016861)
789 doi.org/10.1029/2011JA016861
- 790 Dmitriev, A. V., & Suvorova, A. V. (2015). Large-scale jets in the magnetosheath and plasma
791 penetration across the magnetopause: Themis observations. *Journal of Geophysical*
792 *Research: Space Physics*, 120(6), 4423–4437. Retrieved from [https://doi.org/10](https://doi.org/10.1002/2014JA020953)
793 [.1002/2014JA020953](https://doi.org/10.1002/2014JA020953)
- 794 Eastwood, J. P., Lucek, E. A., Mazelle, C., Meziane, K., Narita, Y., Pickett, J., & Treumann,
795 R. A. (2005). The foreshock. *Space Science Reviews*, 118, 41–94. Retrieved from
796 <https://doi.org/10.1007/s11214-005-3824-3>
- 797 Exner, W., Simon, S., Heyner, D., & Motschmann, U. (2020). Influence of mercury’s
798 exosphere on the structure of the magnetosphere. *Journal of Geophysical Research:*
799 *Space Physics*, 125(7), e2019JA027691. Retrieved from [https://doi.org/10.1029/](https://doi.org/10.1029/2019JA027691)
800 [2019JA027691](https://doi.org/10.1029/2019JA027691)
- 801 Fatemi, S., Holmström, M., & Futaana, Y. (2012). The effects of lunar surface plasma
802 absorption and solar wind temperature anisotropies on the solar wind proton veloc-
803 ity space distributions in the low-altitude lunar plasma wake. *Journal of Geophysi-*
804 *cal Research: Space Physics*, 117(A10). Retrieved from [https://doi.org/10.1029/](https://doi.org/10.1029/2011JA017353)
805 [2011JA017353](https://doi.org/10.1029/2011JA017353)
- 806 Fatemi, S., Poirier, N., Holmström, M., Lindkvist, J., Wieser, M., & Barabash, S. (2018).
807 A modelling approach to infer the solar wind dynamic pressure from magnetic field
808 observations inside Mercury’s magnetosphere. *Astronomy & Astrophysics*, 614, A132.
- 809 Fatemi, S., Poppe, A. R., & Barabash, S. (2020). Hybrid simulations of solar wind proton
810 precipitation to the surface of mercury. *J. Geophys. Res.: Space Physics*, 125(4),
811 e2019JA027706.
- 812 Fatemi, S., Poppe, A. R., Delory, G. T., & Farrell, W. M. (2017). AMITIS: A 3D GPU-
813 Based Hybrid-PIC Model forSpace and Plasma Physics. *J. Phys.: Conf. Ser.*, 837,
814 012017.
- 815 Fatemi, S., Poppe, A. R., Vorburger, A., Lindkvist, J., & Hamrin, M. (2022). Ion dynamics
816 at the magnetopause of ganymede. *Journal of Geophysical Research: Space Physics*,
817 127(1), e2021JA029863. Retrieved from <https://doi.org/10.1029/2021JA029863>
- 818 Fuqua-Haviland, H., Poppe, A. R., Fatemi, S., Delory, G. T., & de Pater, I. (2019). Time-
819 Dependent Hybrid Plasma Simulations of Lunar Electromagnetic Induction in the
820 Solar Wind. *Geophys. Res. Lett.*, 46(8), 4151–4160.

- 821 Ganushkina, N. Y., Liemohn, M. W., & Dubyagin, S. (2018). Current systems in the earth's
 822 magnetosphere. *Reviews of Geophysics*, *56*(2), 309–332. Retrieved from [https://](https://doi.org/10.1002/2017RG000590)
 823 doi.org/10.1002/2017RG000590
- 824 Goncharov, O., Gunell, H., Hamrin, M., & Chong, S. (2020). Evolution of high-speed
 825 jets and plasmoids downstream of the quasi-perpendicular bow shock. *Journal*
 826 *of Geophysical Research: Space Physics*, *125*(6), e2019JA027667. Retrieved from
 827 <https://doi.org/10.1029/2019JA027667>
- 828 Gunell, H., Goetz, C., & Fatemi, S. (2024). Impact of radial interplanetary magnetic fields
 829 on the inner coma of comet 67p/churyumov-gerasimenko-hybrid simulations of the
 830 plasma environment. *Astronomy & Astrophysics*, *682*, A62. Retrieved from [https://](https://doi.org/10.1051/0004-6361/202348186)
 831 doi.org/10.1051/0004-6361/202348186
- 832 Gunell, H., Hamrin, M., Nesbit-Östman, S., Krämer, E., & Nilsson, H. (2023). Mag-
 833 netosheath jets at mars. *Science Advances*, *9*(22), eadg5703. Retrieved from
 834 <https://doi.org/10.1126/sciadv.adg5703>
- 835 Gunell, H., Nilsson, H., Stenberg, G., Hamrin, M., Karlsson, T., Maggiolo, R., ... Dan-
 836 douras, I. (2012). Plasma penetration of the dayside magnetopause. *Physics of*
 837 *Plasmas*, *19*(7). Retrieved from <https://doi.org/10.1063/1.4739446>
- 838 Gunell, H., Stenberg Wieser, G., Mella, M., Maggiolo, R., Nilsson, H., Darrouzet, F., ...
 839 others (2014). Waves in high-speed plasmoids in the magnetosheath and at the
 840 magnetopause. *Annales geophysicae*, *32*(8), 991–1009. Retrieved from [https://doi](https://doi.org/10.5194/angeo-32-991-2014)
 841 [.org/10.5194/angeo-32-991-2014](https://doi.org/10.5194/angeo-32-991-2014)
- 842 Guo, J., Lu, S., Lu, Q., Lin, Y., Wang, X., Ren, J., ... Gao, X. (2022). Large-scale high-
 843 speed jets in earth's magnetosheath: Global hybrid simulations. *Journal of Geophysical*
 844 *Research: Space Physics*, *127*(6), e2022JA030477. Retrieved from [https://doi.org/](https://doi.org/10.1029/2022JA030477)
 845 [10.1029/2022JA030477](https://doi.org/10.1029/2022JA030477)
- 846 Gutynska, O., Sibeck, D. G., & Omid, N. (2015). Magnetosheath plasma structures and
 847 their relation to foreshock processes. *Journal of Geophysical Research: Space Physics*,
 848 *120*(9), 7687–7697. Retrieved from <https://doi.org/10.1002/2014JA020880>
- 849 Han, D.-S., Nishimura, Y., Lyons, L. R., Hu, H.-Q., & Yang, H.-G. (2016). Throat
 850 aurora: The ionospheric signature of magnetosheath particles penetrating into the
 851 magnetosphere. *Geophysical Research Letters*, *43*(5), 1819–1827. Retrieved from
 852 <https://doi.org/10.1002/2016GL068181>
- 853 Hao, Y., Lembège, B., Lu, Q., & Guo, F. (2016). Formation of downstream high-speed jets

- 854 by a rippled nonstationary quasi-parallel shock: 2-d hybrid simulations. *Journal of*
855 *Geophysical Research: Space Physics*, *121*(3), 2080–2094. Retrieved from [https://](https://doi.org/10.1002/2015JA021419)
856 doi.org/10.1002/2015JA021419
- 857 Hao, Y., Lu, Q., Gao, X., & Wang, S. (2016). Ion dynamics at a rippled quasi-parallel
858 shock: 2d hybrid simulations. *The Astrophysical Journal*, *823*(1), 7. Retrieved from
859 <https://doi.org/10.3847/0004-637X/823/1/7>
- 860 Harned, D. S. (1982). Quasineutral hybrid simulation of macroscopic plasma phenomena.
861 *Journal of Computational Physics*, *47*(3), 452–462. Retrieved from [https://doi.org/](https://doi.org/10.1016/0021-9991(82)90094-8)
862 [10.1016/0021-9991\(82\)90094-8](https://doi.org/10.1016/0021-9991(82)90094-8)
- 863 Herčík, D., Trávníček, P. M., Štverák, Š., & Hellinger, P. (2016). Properties of hermean
864 plasma belt: Numerical simulations and comparison with messenger data. *Journal*
865 *of Geophysical Research: Space Physics*, *121*(1), 413–431. Retrieved from [https://](https://doi.org/10.1002/2015JA021938)
866 doi.org/10.1002/2015JA021938
- 867 Hietala, H., Laitinen, T. V., Andréevová, K., Vainio, R., Vaivads, A., Palmroth, M.,
868 ... Rème, H. (2009). Supermagnetosonic jets behind a collisionless quasiparallel
869 shock. *Physical Review Letters*, *103*(24), 245001. Retrieved from [https://doi.org/](https://doi.org/10.1103/PhysRevLett.103.245001)
870 [10.1103/PhysRevLett.103.245001](https://doi.org/10.1103/PhysRevLett.103.245001)
- 871 Hietala, H., Partamies, N., Laitinen, T. V., Clausen, L. B. N., Facskó, G., Vaivads, A., ...
872 Lucek, E. (2012). Supermagnetosonic subsolar magnetosheath jets and their effects:
873 From the solar wind to the ionospheric convection. *Annales Geophysicae*, *30*(1), 33–48.
874 Retrieved from <https://doi.org/10.5194/angeo-30-33-2012>
- 875 Hietala, H., Phan, T. D., Angelopoulos, V., Oieroset, M., Archer, M. O., Karlsson, T.,
876 & Plaschke, F. (2018). In situ observations of a magnetosheath high-speed jet trig-
877 gering magnetopause reconnection. *Geophysical Research Letters*, *45*(4), 1732–1740.
878 Retrieved from <https://doi.org/10.1002/2017GL076525>
- 879 Hietala, H., & Plaschke, F. (2013). On the generation of magnetosheath high-speed jets by
880 bow shock ripples. *Journal of Geophysical Research: Space Physics*, *118*(11), 7237–
881 7245. Retrieved from <https://doi.org/10.1002/2013JA019172>
- 882 Holmström, M. (2013). Handling vacuum regions in a hybrid plasma solver. *ASTRONUM-*
883 *2012, ASP conference series*(474), 202–207.
- 884 Holmström, M., Fatemi, S., Futaana, Y., & Nilsson, H. (2012). The interaction between
885 the moon and the solar wind. *Earth, planets and space*, *64*, 237–245. Retrieved from
886 <https://link.springer.com/article/10.5047/eps.2011.06.040>

- 887 Jarvinen, R., Alho, M., Kallio, E., & Pulkkinen, T. (2020). Ultra-low-frequency waves in
888 the ion foreshock of mercury: a global hybrid modelling study. *Monthly Notices of the*
889 *Royal Astronomical Society*, *491*(3), 4147–4161. Retrieved from [https://doi.org/](https://doi.org/10.1093/mnras/stz3257)
890 [10.1093/mnras/stz3257](https://doi.org/10.1093/mnras/stz3257)
- 891 Kajdič, P., Blanco-Cano, X., Omidi, N., Rojas-Castillo, D., Sibeck, D. G., & Billing-
892 ham, L. (2017). Traveling foreshocks and transient foreshock phenomena. *Journal of Geophysical Research: Space Physics*, *122*(9), 9148–9168. Retrieved from
893 <https://doi.org/10.1002/2017JA023901>
- 894
895 Kajdič, P., Raptis, S., Blanco-Cano, X., & Karlsson, T. (2021). Causes of jets in the quasi-
896 perpendicular magnetosheath. *Geophysical Research Letters*, *48*(13), e2021GL093173.
897 Retrieved from <https://doi.org/10.1029/2021GL093173>
- 898 Kallio, E. (2005). Formation of the lunar wake in quasi-neutral hybrid model. *Geophysical*
899 *Research Letters*, *32*(6). Retrieved from <https://doi.org/10.1029/2004GL021989>
- 900 Kallio, E., & Janhunen, P. (2004). The response of the hermean magnetosphere to the inter-
901 planetary magnetic field. *Advances in Space research*, *33*(12), 2176–2181. Retrieved
902 from [https://doi.org/10.1016/S0273-1177\(03\)00447-2](https://doi.org/10.1016/S0273-1177(03)00447-2)
- 903 Karimabadi, H., Roytershteyn, V., Vu, H., Omelchenko, Y., Scudder, J., Daughton, W., ...
904 others (2014). The link between shocks, turbulence, and magnetic reconnection in
905 collisionless plasmas. *Physics of Plasmas*, *21*(6). Retrieved from [https://doi.org/](https://doi.org/10.1063/1.4882875)
906 [10.1063/1.4882875](https://doi.org/10.1063/1.4882875)
- 907 Karlsson, T., Brenning, N., Nilsson, H., Trotignon, J.-G., Vallières, X., & Facsko, G.
908 (2012). Localized density enhancements in the magnetosheath: Three-dimensional
909 morphology and possible importance for impulsive penetration. *Journal of Geophys-*
910 *ical Research: Space Physics*, *117*(A3). Retrieved from [https://doi.org/10.1029/](https://doi.org/10.1029/2011JA017059)
911 [2011JA017059](https://doi.org/10.1029/2011JA017059)
- 912 Karlsson, T., Kullen, A., Liljeblad, E., Brenning, N., Nilsson, H., Gunell, H., & Hamrin, M.
913 (2015). On the origin of magnetosheath plasmoids and their relation to magnetosheath
914 jets. *Journal of Geophysical Research: Space Physics*, *120*(9), 7390–7403. Retrieved
915 from <https://doi.org/10.1002/2015JA021487>
- 916 Karlsson, T., Plaschke, F., Hietala, H., Archer, M., Blanco-Cano, X., Kajdič, P., ... Ger-
917 shman, D. J. (2018). Investigating the anatomy of magnetosheath jets—mms obser-
918 vations. , *36*(2), 655–677. Retrieved from [https://doi.org/10.5194/angeo-36-655](https://doi.org/10.5194/angeo-36-655-2018)
919 [-2018](https://doi.org/10.5194/angeo-36-655-2018)

- 920 Kivelson, M. G., & Russell, C. T. (1995). *Introduction to space physics*. Cambridge university
921 press.
- 922 Krämer, E., Hamrin, M., Gunell, H., Karlsson, T., Steinvall, K., Goncharov, O., & André, M.
923 (2023). Waves in magnetosheath jets-classification and the search for generation mech-
924 anisms using mms burst mode data. *Journal of Geophysical Research: Space Physics*,
925 *128*(7), e2023JA031621. Retrieved from <https://doi.org/10.1029/2023JA031621>
- 926 LaMoury, A. T., Hietala, H., Plaschke, F., Vuorinen, L., & Eastwood, J. P. (2021). Solar
927 wind control of magnetosheath jet formation and propagation to the magnetopause.
928 *Journal of Geophysical Research: Space Physics*, *126*(9), e2021JA029592. Retrieved
929 from <https://doi.org/10.1029/2021JA029592>
- 930 Lavraud, B., Borovsky, J., Ridley, A., Pogue, E., Thomsen, M., Rème, H., ... Lucek,
931 E. (2007). Strong bulk plasma acceleration in earth's magnetosheath: A magnetic
932 slingshot effect? *Geophysical Research Letters*, *34*(14). Retrieved from [https://](https://doi.org/10.1029/2007GL030024)
933 doi.org/10.1029/2007GL030024
- 934 Le, A., Stanier, A., Yin, L., Wetherton, B., Keenan, B., & Albright, B. (2023). Hybrid-vpic:
935 An open-source kinetic/fluid hybrid particle-in-cell code. *Physics of Plasmas*, *30*(6).
936 Retrieved from <https://doi.org/10.1063/5.0146529>
- 937 Le, G., Lühr, H., Anderson, B., Strangeway, R., Russell, C., Singer, H., ... others
938 (2016). Magnetopause erosion during the 17 march 2015 magnetic storm: Com-
939 bined field-aligned currents, auroral oval, and magnetopause observations. *Geophysi-
940 cal Research Letters*, *43*(6), 2396–2404. Retrieved from [https://doi.org/10.1002/](https://doi.org/10.1002/2016GL068257)
941 [2016GL068257](https://doi.org/10.1002/2016GL068257)
- 942 Ledvina, S., Ma, Y.-J., & Kallio, E. (2008). Modeling and simulating flowing plasmas
943 and related phenomena. *Comparative aeronomy*, 143–189. Retrieved from [https://](https://link.springer.com/chapter/10.1007/978-0-387-87825-6_5)
944 link.springer.com/chapter/10.1007/978-0-387-87825-6_5
- 945 Liu, T. Z., Hietala, H., Angelopoulos, V., Omelchenko, Y., Roytershteyn, V., & Vainio,
946 R. (2019). Themis observations of particle acceleration by a magnetosheath jet-
947 driven bow wave. *Geophysical Research Letters*, *46*(14), 7929–7936. Retrieved from
948 <https://doi.org/10.1029/2019GL082614>
- 949 Lopez, R. E., Merkin, V., & Lyon, J. (2011). The role of the bow shock in solar wind-
950 magnetosphere coupling. In *Annales geophysicae* (Vol. 29, pp. 1129–1135). Retrieved
951 from <https://doi.org/10.5194/angeo-29-1129-2011>
- 952 Milan, S. E., Clausen, L. B. N., Coxon, J. C., Carter, J. A., Walach, M.-T., Laundal, K.,

- 953 ... others (2017). Overview of solar wind–magnetosphere–ionosphere–atmosphere
954 coupling and the generation of magnetospheric currents. *Space Science Reviews*, 206,
955 547–573. Retrieved from <https://doi.org/10.1007/s11214-017-0333-0>
- 956 Müller, J., Simon, S., Wang, Y.-C., Motschmann, U., Heyner, D., Schüle, J., ... Pringle,
957 G. J. (2012). Origin of mercury’s double magnetopause: 3d hybrid simulation study
958 with aikef. *Icarus*, 218(1), 666–687. Retrieved from [https://doi.org/10.1016/
959 j.icarus.2011.12.028](https://doi.org/10.1016/j.icarus.2011.12.028)
- 960 Narita, Y., Plaschke, F., & Vörös, Z. (2021). The magnetosheath. *Magnetospheres in the*
961 *Solar System*, 137–152. Retrieved from [https://doi.org/10.1002/9781119815624
962 .ch9](https://doi.org/10.1002/9781119815624.ch9)
- 963 Němeček, Z., Šafránková, J., Přejch, L., Sibeck, D., Kokubun, S., & Mukai, T. (1998).
964 Transient flux enhancements in the magnetosheath. *Geophysical Research Letters*,
965 25(8), 1273–1276. Retrieved from <https://doi.org/10.1029/98GL50873>
- 966 Ng, J., Chen, L.-J., & Omelchenko, Y. (2021). Bursty magnetic reconnection at the earth’s
967 magnetopause triggered by high-speed jets. *Physics of Plasmas*, 28(9). Retrieved
968 from <https://doi.org/10.1063/5.0054394>
- 969 Norenus, L., Hamrin, M., Goncharov, O., Gunell, H., Opgenoorth, H., Pitkänen, T.,
970 ... Baddeley, L. (2021). Ground-based magnetometer response to impacting
971 magnetosheath jets. *Journal of Geophysical Research: Space Physics*, 126(8),
972 e2021JA029115. Retrieved from <https://doi.org/10.1029/2021JA029115>
- 973 Omelchenko, Y., Chen, L.-J., & Ng, J. (2021). 3d space-time adaptive hybrid simulations
974 of magnetosheath high-speed jets. *Journal of Geophysical Research: Space Physics*,
975 126(7), e2020JA029035. Retrieved from <https://doi.org/10.1029/2020JA029035>
- 976 Omid, N., Berchem, J., Sibeck, D., & Zhang, H. (2016). Impacts of spontaneous hot
977 flow anomalies on the magnetosheath and magnetopause. *Journal of Geophysical*
978 *Research: Space Physics*, 121(4), 3155–3169. Retrieved from [https://doi.org/10
979 .1002/2015JA022170](https://doi.org/10.1002/2015JA022170)
- 980 Palmroth, M., Hietala, H., Plaschke, F., Archer, M., Karlsson, T., Blanco-Cano, X., ...
981 others (2018). Magnetosheath jet properties and evolution as determined by a global
982 hybrid-vlasov simulation. *Annales Geophysicae*, 36(5), 1171–1182. Retrieved from
983 <https://doi.org/10.5194/angeo-36-1171-2018>
- 984 Palmroth, M., Raptis, S., Suni, J., Karlsson, T., Turc, L., Johlander, A., ... others (2021).
985 Magnetosheath jet evolution as a function of lifetime: Global hybrid-vlasov simulations

- 986 compared to mms observations. *Annales Geophysicae*, *39*(2), 289–308. Retrieved from
987 <https://doi.org/10.5194/angeo-39-289-2021>
- 988 Phan, T., Paschmann, G., Twitty, C., Mozer, F., Gosling, J., Eastwood, J., ... Lucek,
989 E. (2007). Evidence for magnetic reconnection initiated in the magnetosheath.
990 *Geophysical Research Letters*, *34*(14). Retrieved from [https://doi.org/10.1029/
991 2007GL030343](https://doi.org/10.1029/2007GL030343)
- 992 Plaschke, F., Hietala, H., & Angelopoulos, V. (2013). Anti-sunward high-speed jets in the
993 subsolar magnetosheath. *Annales Geophysicae*, *31*(10), 1877–1889. Retrieved from
994 <https://doi.org/10.5194/angeo-31-1877-2013>
- 995 Plaschke, F., Hietala, H., Angelopoulos, V., & Nakamura, R. (2016). Geoeffective jets
996 impacting the magnetopause are very common. *Journal of Geophysical Research:
997 Space Physics*, *121*(4), 3240–3253. Retrieved from [https://doi.org/10.1002/
998 2016JA022534](https://doi.org/10.1002/2016JA022534)
- 999 Plaschke, F., Hietala, H., Archer, M., Blanco-Cano, X., Kajdič, P., Karlsson, T., ... others
1000 (2018). Jets downstream of collisionless shocks. *Space Science Reviews*, *214*, 1–77.
1001 Retrieved from <https://doi.org/10.1007/s11214-018-0516-3>
- 1002 Plaschke, F., Hietala, H., & Vörös, Z. (2020). Scale sizes of magnetosheath jets. *Journal
1003 of Geophysical Research: Space Physics*, *125*(9), e2020JA027962. Retrieved from
1004 <https://doi.org/10.1029/2020JA027962>
- 1005 Plaschke, F., Karlsson, T., Hietala, H., Archer, M., Vörös, Z., Nakamura, R., ... oth-
1006 ers (2017). Magnetosheath high-speed jets: Internal structure and interaction with
1007 ambient plasma. *Journal of Geophysical Research: Space Physics*, *122*(10), 10–157.
1008 Retrieved from <https://doi.org/10.1002/2017JA024471>
- 1009 Poppe, A. R., & Fatemi, S. (2023). The solar wind interaction with (1) ceres: The role
1010 of interior conductivity. *The Planetary Science Journal*, *4*(1), 14. Retrieved from
1011 <https://doi.org/10.3847/PSJ/acaf6a>
- 1012 Poppe, A. R., Garrick-Bethell, I., & Fatemi, S. (2021). Fractionation of solar wind minor
1013 ion precipitation by the lunar paleomagnetosphere. *The Planetary Science Journal*,
1014 *2*(2), 60. Retrieved from <https://doi.org/10.3847/PSJ/abea7d>
- 1015 Preisser, L., Blanco-Cano, X., Kajdič, P., Burgess, D., & Trotta, D. (2020). Magne-
1016 tosheath jets and plasmoids: Characteristics and formation mechanisms from hy-
1017 brid simulations. *The Astrophysical Journal Letters*, *900*(1), L6. Retrieved from
1018 <https://doi.org/10.3847/2041-8213/abad2b>

- 1019 Rakhmanova, L., Riazantseva, M., Zastenker, G., & Yermolaev, Y. (2023). Role of the
1020 variable solar wind in the dynamics of small-scale magnetosheath structures. *Frontiers*
1021 *in Astronomy and Space Sciences*, *10*, 1121230. Retrieved from [https://doi.org/](https://doi.org/10.3389/fspas.2023.1121230)
1022 [10.3389/fspas.2023.1121230](https://doi.org/10.3389/fspas.2023.1121230)
- 1023 Raptis, S., Karlsson, T., Plaschke, F., Kullen, A., & Lindqvist, P.-A. (2020). Classifying
1024 magnetosheath jets using mms: Statistical properties. *Journal of Geophysical Re-*
1025 *search: Space Physics*, *125*(11), e2019JA027754. Retrieved from [https://doi.org/](https://doi.org/10.1029/2019JA027754)
1026 [10.1029/2019JA027754](https://doi.org/10.1029/2019JA027754)
- 1027 Raptis, S., Karlsson, T., Vaivads, A., Lindberg, M., Johlander, A., & Trollvik, H. (2022).
1028 On magnetosheath jet kinetic structure and plasma properties. *Geophysical Re-*
1029 *search Letters*, *49*(21), e2022GL100678. Retrieved from [https://doi.org/10.1029/](https://doi.org/10.1029/2022GL100678)
1030 [2022GL100678](https://doi.org/10.1029/2022GL100678)
- 1031 Raptis, S., Karlsson, T., Vaivads, A., Pollock, C., Plaschke, F., Johlander, A., ... Lindqvist,
1032 P.-A. (2022). Downstream high-speed plasma jet generation as a direct consequence
1033 of shock reformation. *Nature communications*, *13*(1), 598. Retrieved from [https://](https://doi.org/10.1038/s41467-022-28110-4)
1034 doi.org/10.1038/s41467-022-28110-4
- 1035 Rasca, A. P., Fatemi, S., & Farrell, W. M. (2022). Modeling the lunar wake response to
1036 a cme using a hybrid pic model. *The Planetary Science Journal*, *3*(1), 4. Retrieved
1037 from <https://doi.org/10.3847/PSJ/ac3fba>
- 1038 Russell, C., & Hoppe, M. (1983). Upstream waves and particles. *Space Science Reviews*,
1039 *34*(2), 155–172. Retrieved from <https://doi.org/10.1007/BF00194624>
- 1040 Savin, S., Amata, E., Zelenyi, L., Budaev, V., Consolini, G., Treumann, R., ... others
1041 (2008). High energy jets in the earth's magnetosheath: Implications for plasma
1042 dynamics and anomalous transport. *JETP letters*, *87*, 593–599. Retrieved from
1043 <https://doi.org/10.1134/S0021364008110015>
- 1044 Savin, S., Amata, E., Zelenyi, L., Lutsenko, V., Safrankova, J., Nemecek, Z., ... others
1045 (2012). Super fast plasma streams as drivers of transient and anomalous magne-
1046 topheric dynamics. *Annales Geophysicae*, *30*(1), 1–7. Retrieved from [https://](https://doi.org/10.5194/angeo-30-1-2012)
1047 doi.org/10.5194/angeo-30-1-2012
- 1048 Shi, Z., Rong, Z., Fatemi, S., Slavin, J. A., Klinger, L., Dong, C., ... others (2022).
1049 An eastward current encircling mercury. *Geophysical Research Letters*, *49*(10),
1050 e2022GL098415. Retrieved from <https://doi.org/10.1029/2022GL098415>
- 1051 Shue, J.-H., Chao, J.-K., Song, P., McFadden, J., Suvorova, A., Angelopoulos, V., ...

- 1052 Plaschke, F. (2009). Anomalous magnetosheath flows and distorted subsolar mag-
1053 netopause for radial interplanetary magnetic fields. *Geophysical Research Letters*,
1054 *36*(18). Retrieved from <https://doi.org/10.1029/2009GL039842>
- 1055 Suni, J., Palmroth, M., Turc, L., Battarbee, M., Johlander, A., Tarvus, V., ... others (2021).
1056 Connection between foreshock structures and the generation of magnetosheath jets:
1057 Vlasiator results. *Geophysical Research Letters*, *48*(20), e2021GL095655. Retrieved
1058 from <https://doi.org/10.1029/2021GL095655>
- 1059 Tóth, G., Chen, Y., Gombosi, T. I., Cassak, P., Markidis, S., & Peng, I. B. (2017). Scaling
1060 the ion inertial length and its implications for modeling reconnection in global simu-
1061 lations. *Journal of Geophysical Research: Space Physics*, *122*(10), 10–336. Retrieved
1062 from <https://doi.org/10.1002/2017JA024186>
- 1063 Voitcu, G., & Echim, M. (2018). Crescent-shaped electron velocity distribution functions
1064 formed at the edges of plasma jets interacting with a tangential discontinuity. In
1065 *Annales geophysicae* (Vol. 36, pp. 1521–1535). Retrieved from [https://doi.org/](https://doi.org/10.5194/angeo-36-1521-2018)
1066 [10.5194/angeo-36-1521-2018](https://doi.org/10.5194/angeo-36-1521-2018)
- 1067 Vuorinen, L., Hietala, H., & Plaschke, F. (2019). Jets in the magnetosheath: Imf control
1068 of where they occur. , *37*(4), 689–697. Retrieved from [https://doi.org/10.5194/](https://doi.org/10.5194/angeo-37-689-2019)
1069 [angeo-37-689-2019](https://doi.org/10.5194/angeo-37-689-2019)
- 1070 Walt, M. (1994). Introduction to geomagnetically trapped radiation. *Camb. Atmos. Space*
1071 *Sci. Ser.*, *10*.
- 1072 Wang, B., Nishimura, Y., Hietala, H., & Angelopoulos, V. (2022). Investigating the role
1073 of magnetosheath high-speed jets in triggering dayside ground magnetic ultra-low
1074 frequency waves. *Geophysical Research Letters*, *49*(22), e2022GL099768. Retrieved
1075 from <https://doi.org/10.1029/2022GL099768>
- 1076 Wang, B., Nishimura, Y., Hietala, H., Lyons, L., Angelopoulos, V., Plaschke, F., ...
1077 Weatherwax, A. (2018). Impacts of magnetosheath high-speed jets on the mag-
1078 netosphere and ionosphere measured by optical imaging and satellite observations.
1079 *Journal of Geophysical Research: Space Physics*, *123*(6), 4879–4894. Retrieved from
1080 <https://doi.org/10.1029/2017JA024954>
- 1081 Wang, X.-D., Fatemi, S., Nilsson, H., Futaana, Y., Holmström, M., & Barabash, S.
1082 (2023). Solar wind interaction with mars: electric field morphology and source terms.
1083 *Monthly Notices of the Royal Astronomical Society*, *521*(3), 3597–3607. Retrieved
1084 from <https://doi.org/10.1093/mnras/stad247>

1085 Wiltberger, M., Lopez, R. E., & Lyon, J. G. (2003). Magnetopause erosion: A global
1086 view from mhd simulation. *Journal of Geophysical Research: Space Physics*, *108*(A6).
1087 Retrieved from <https://doi.org/10.1029/2002JA009564>

Figure 1.

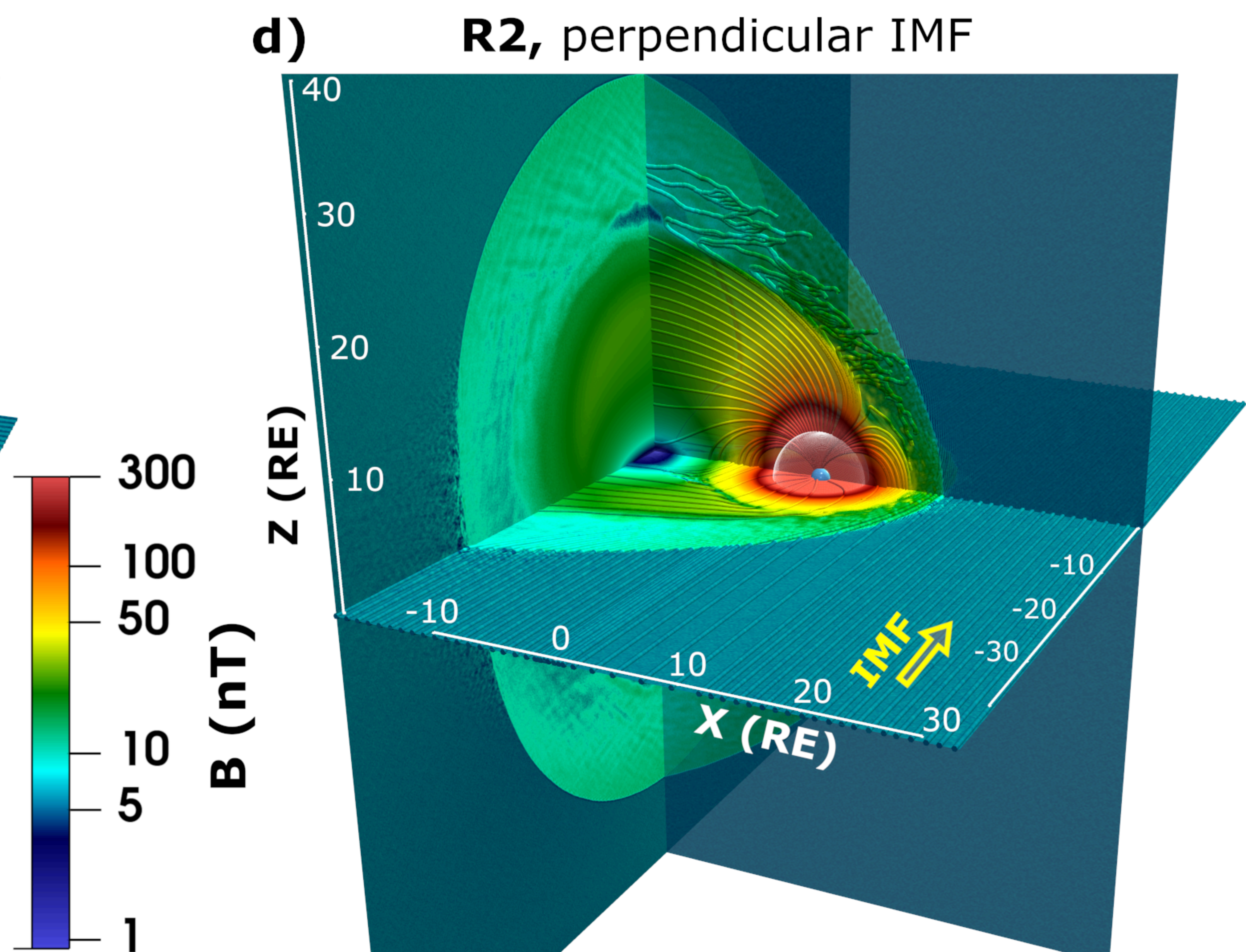
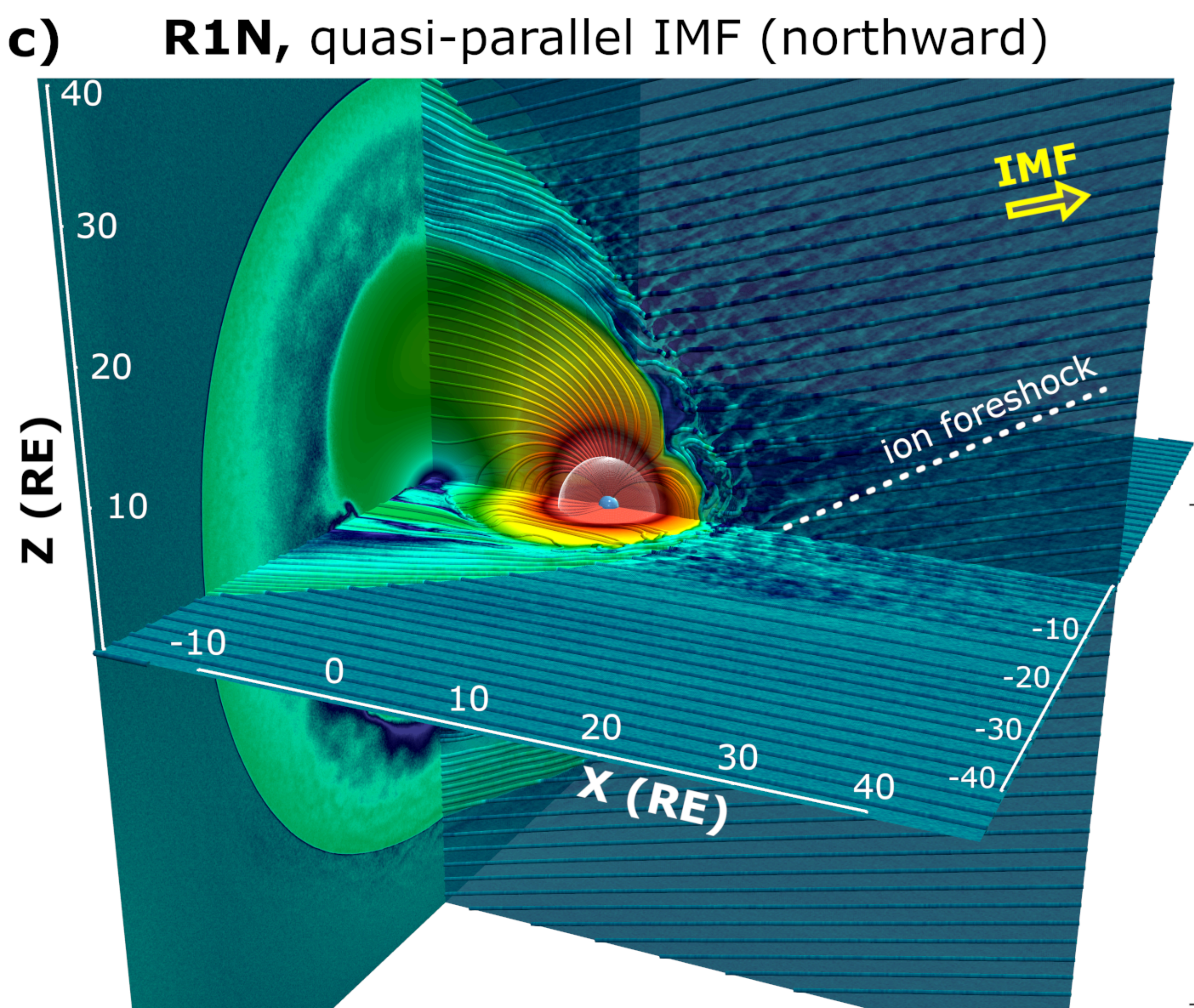
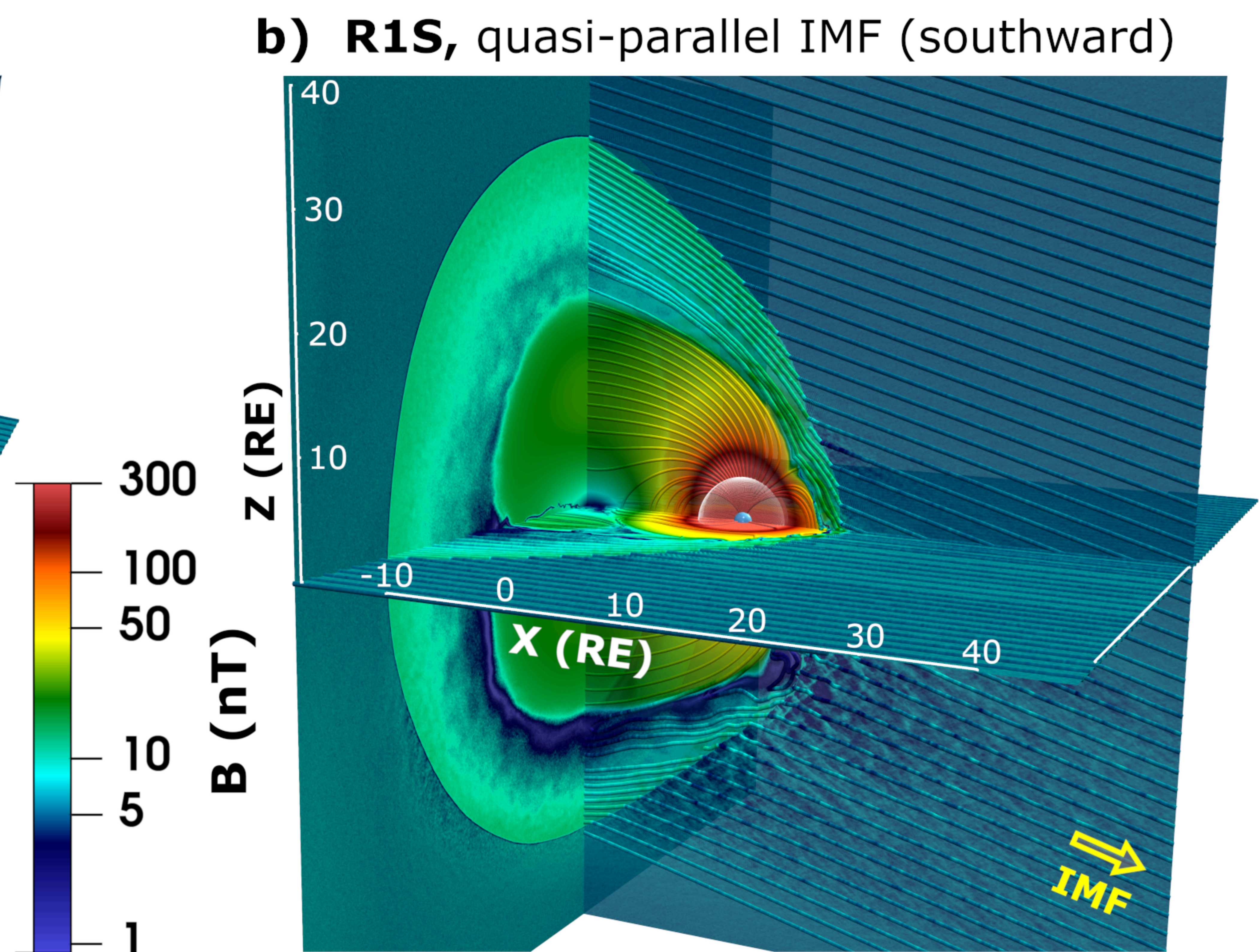
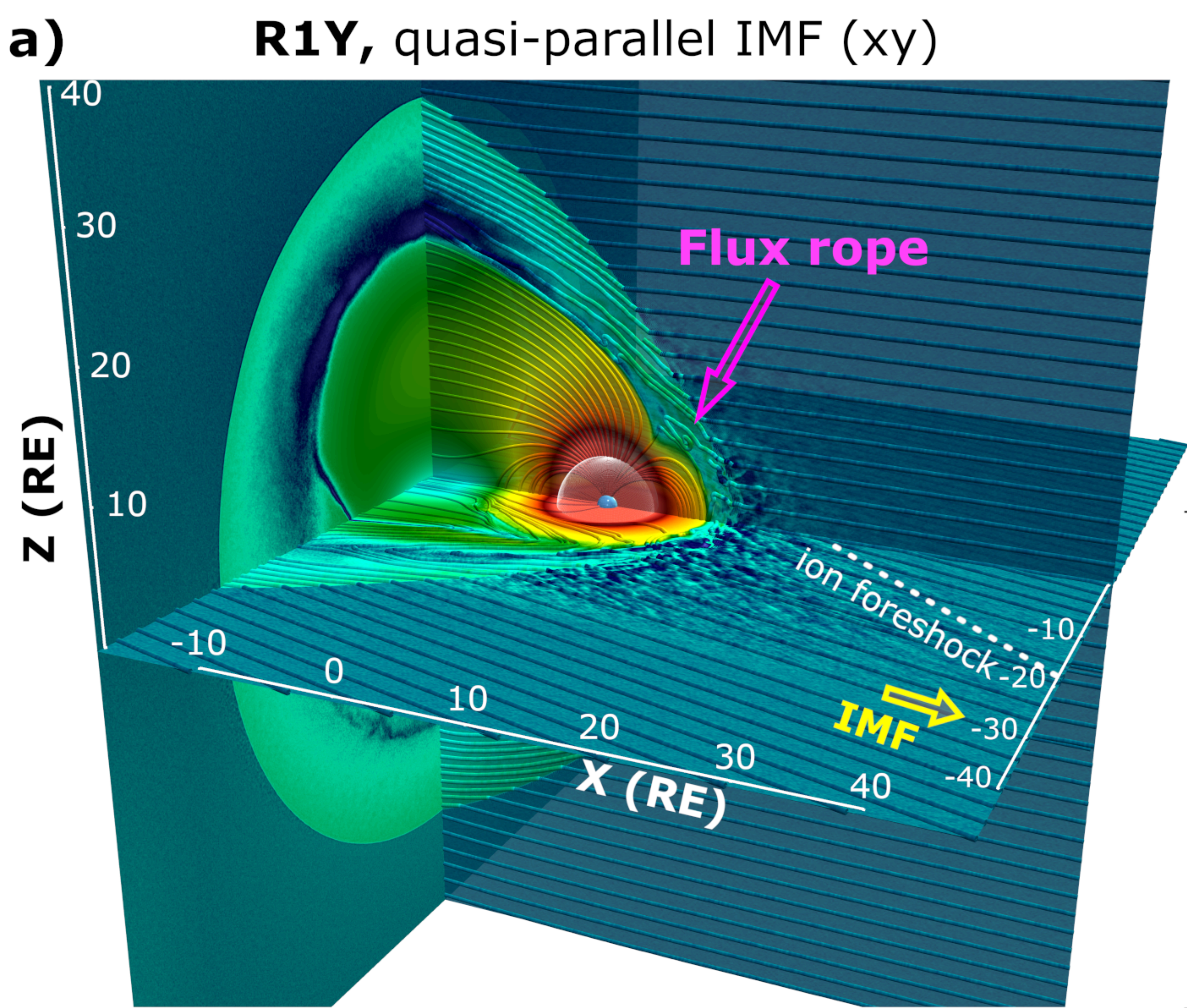


Figure 2.

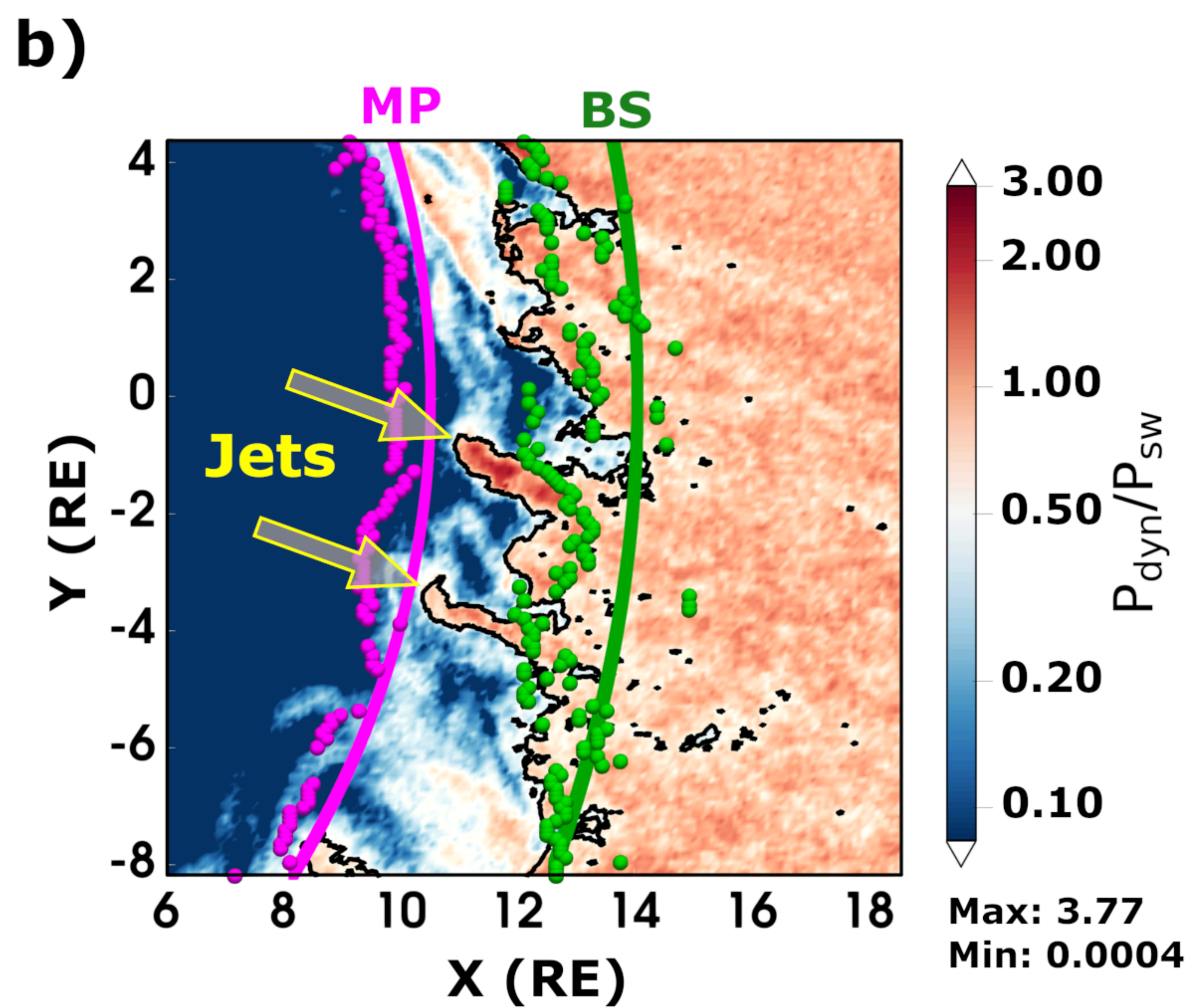
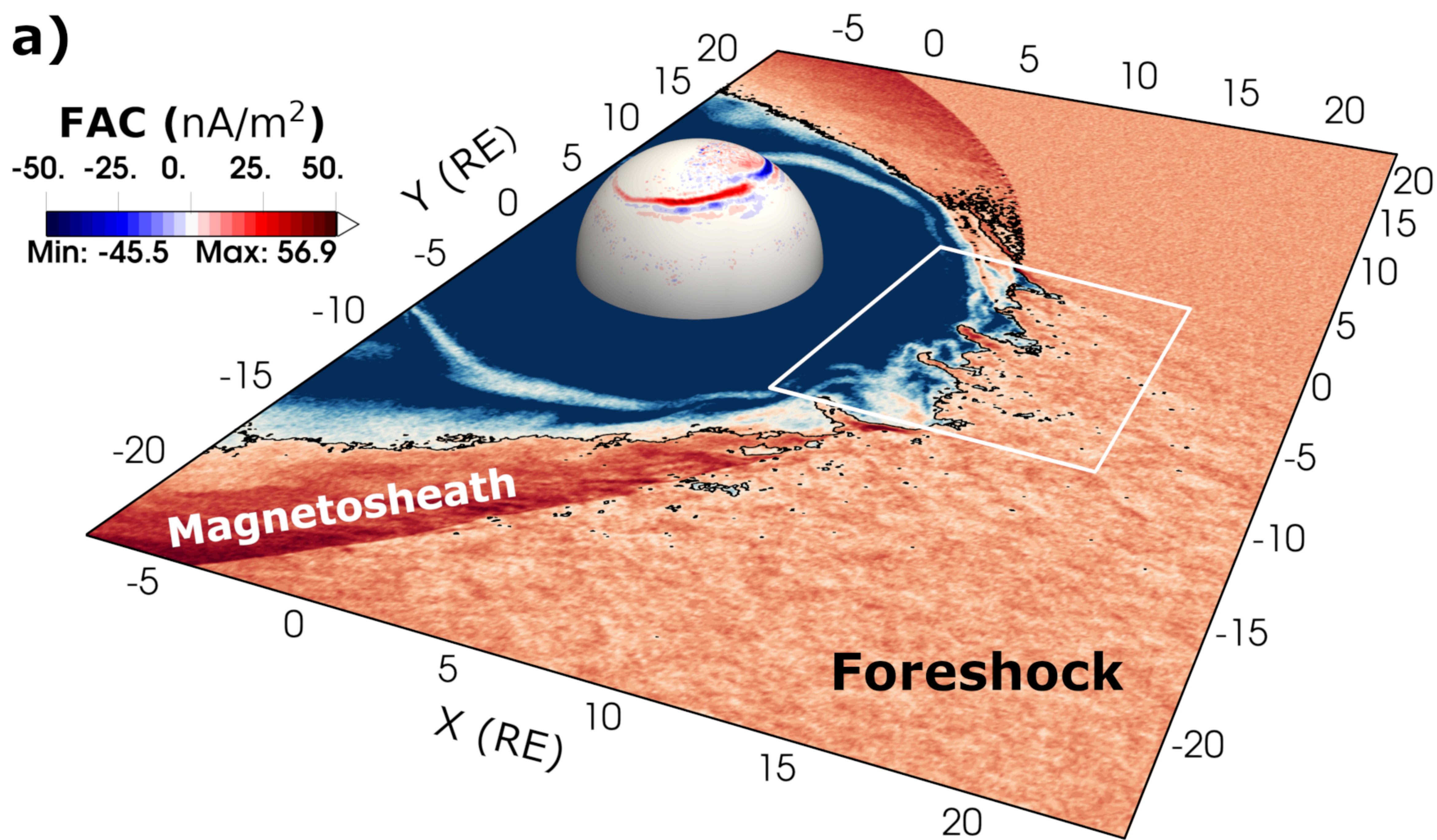


Figure 3.

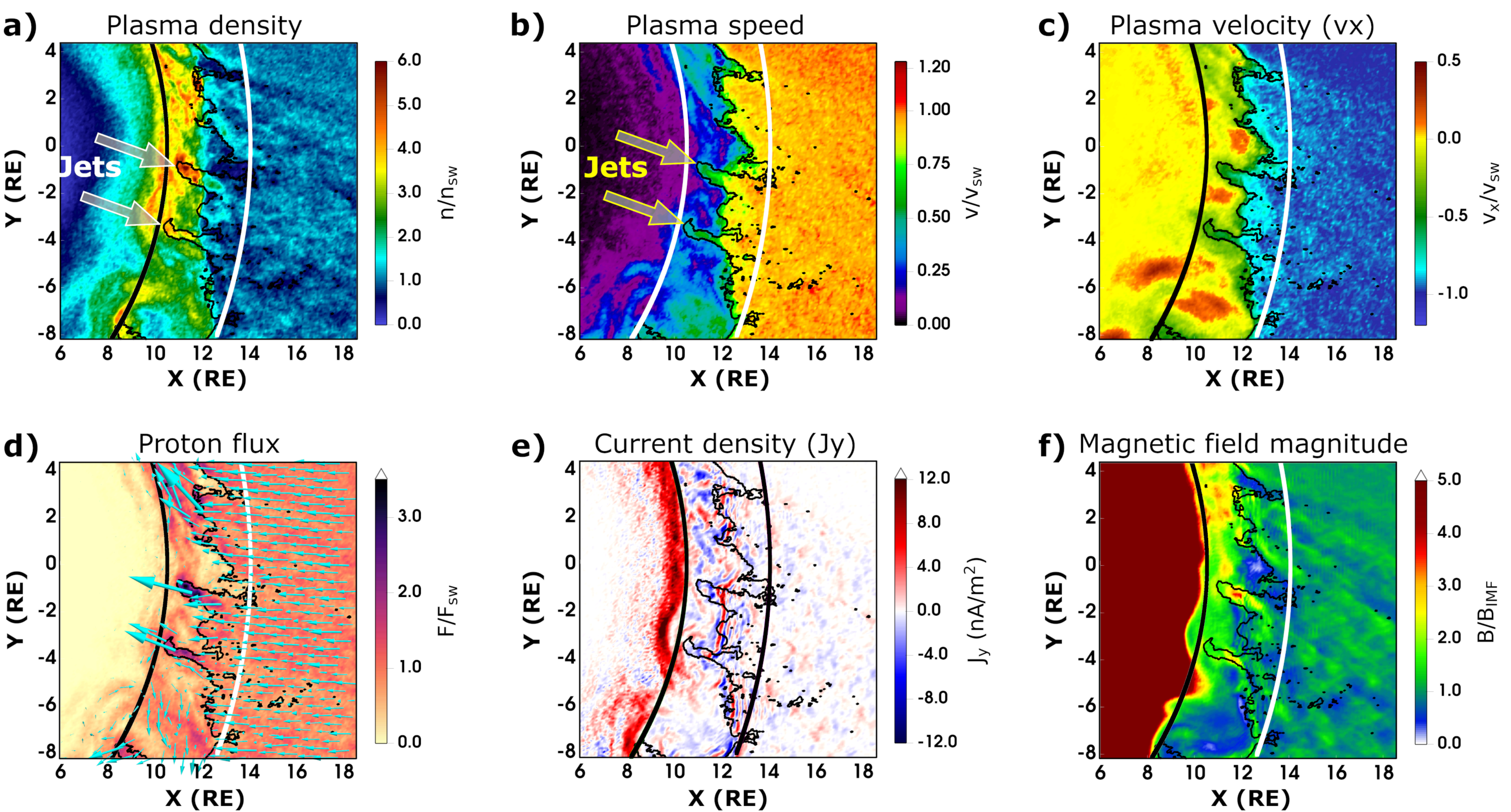


Figure 4.

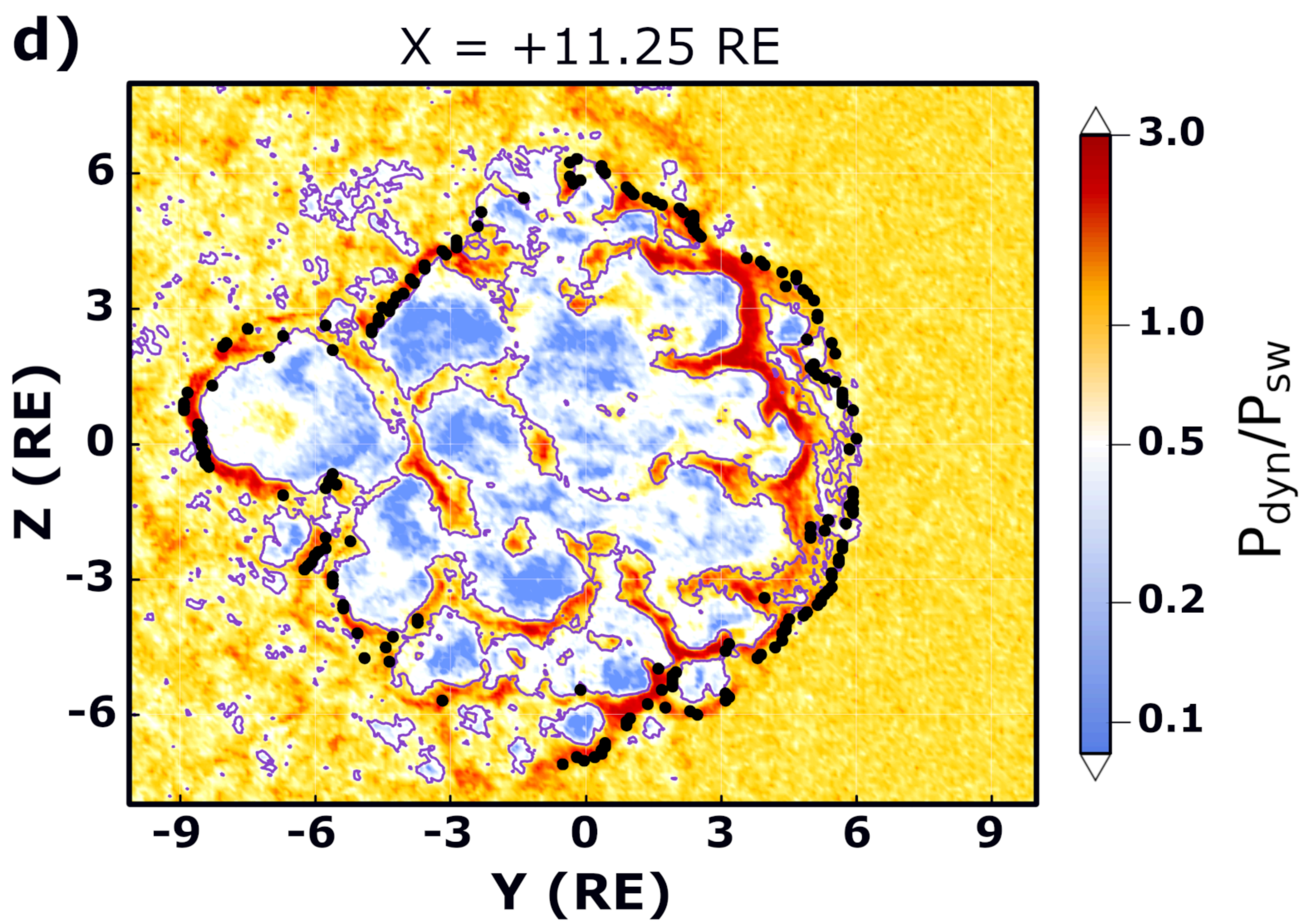
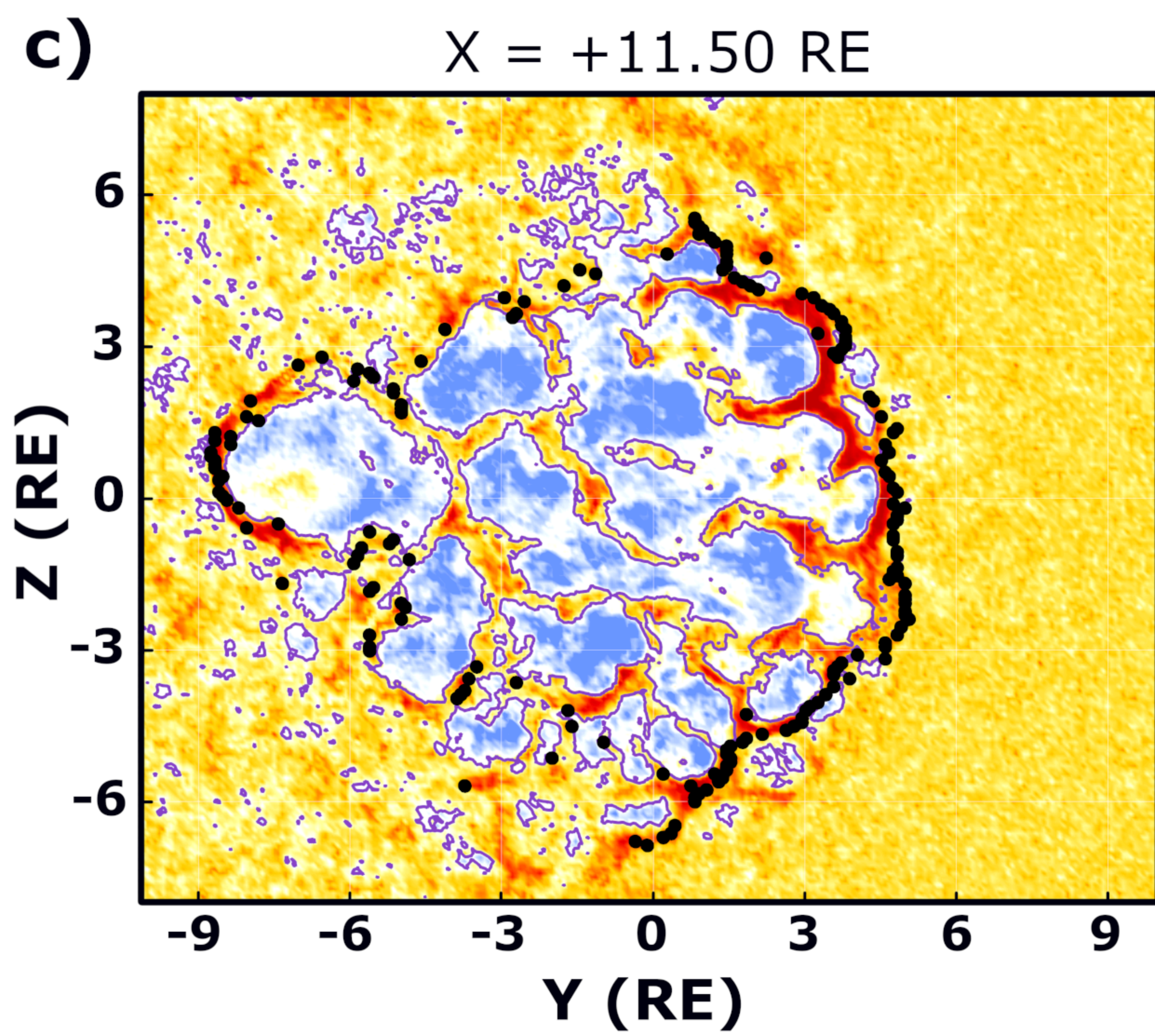
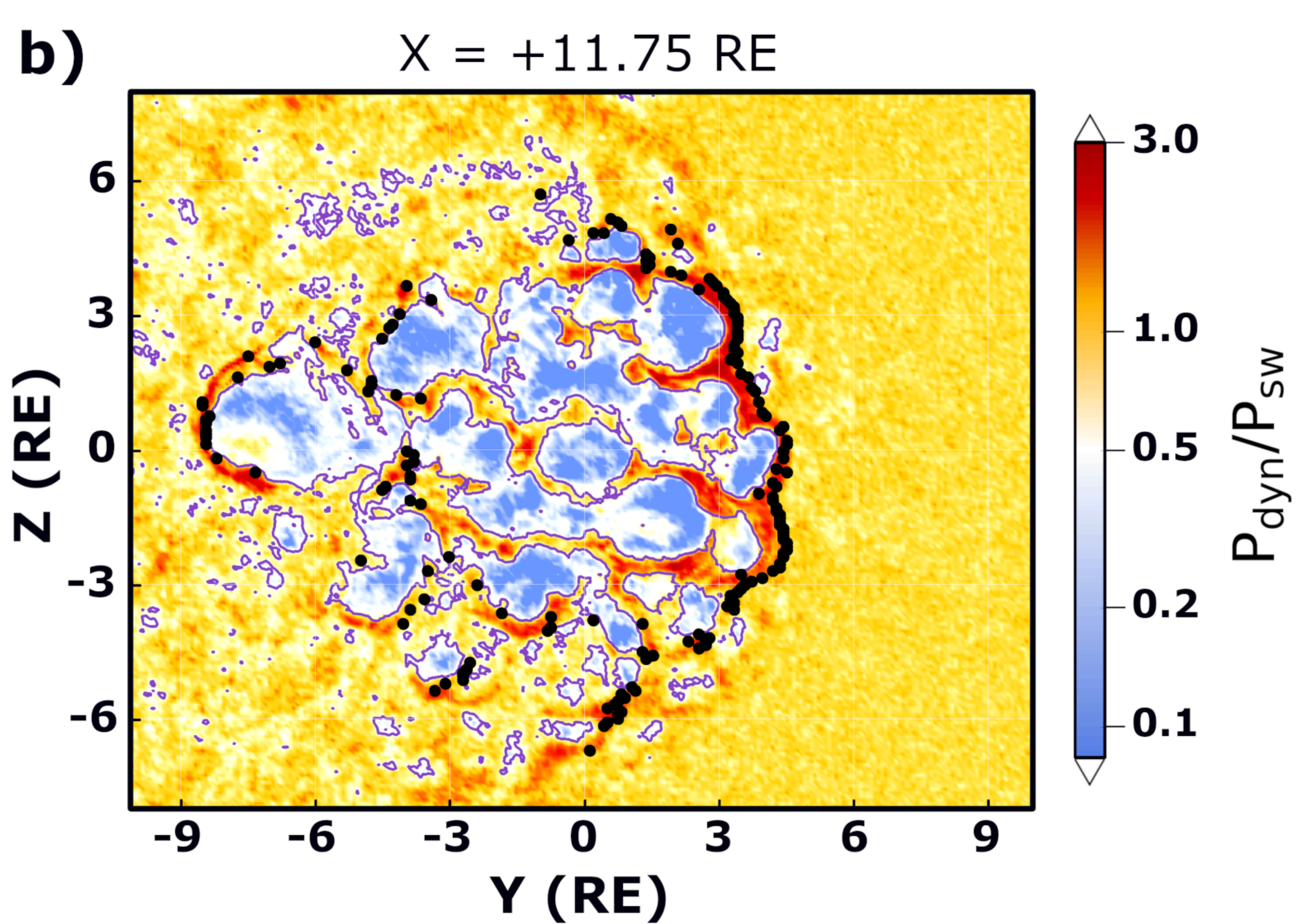
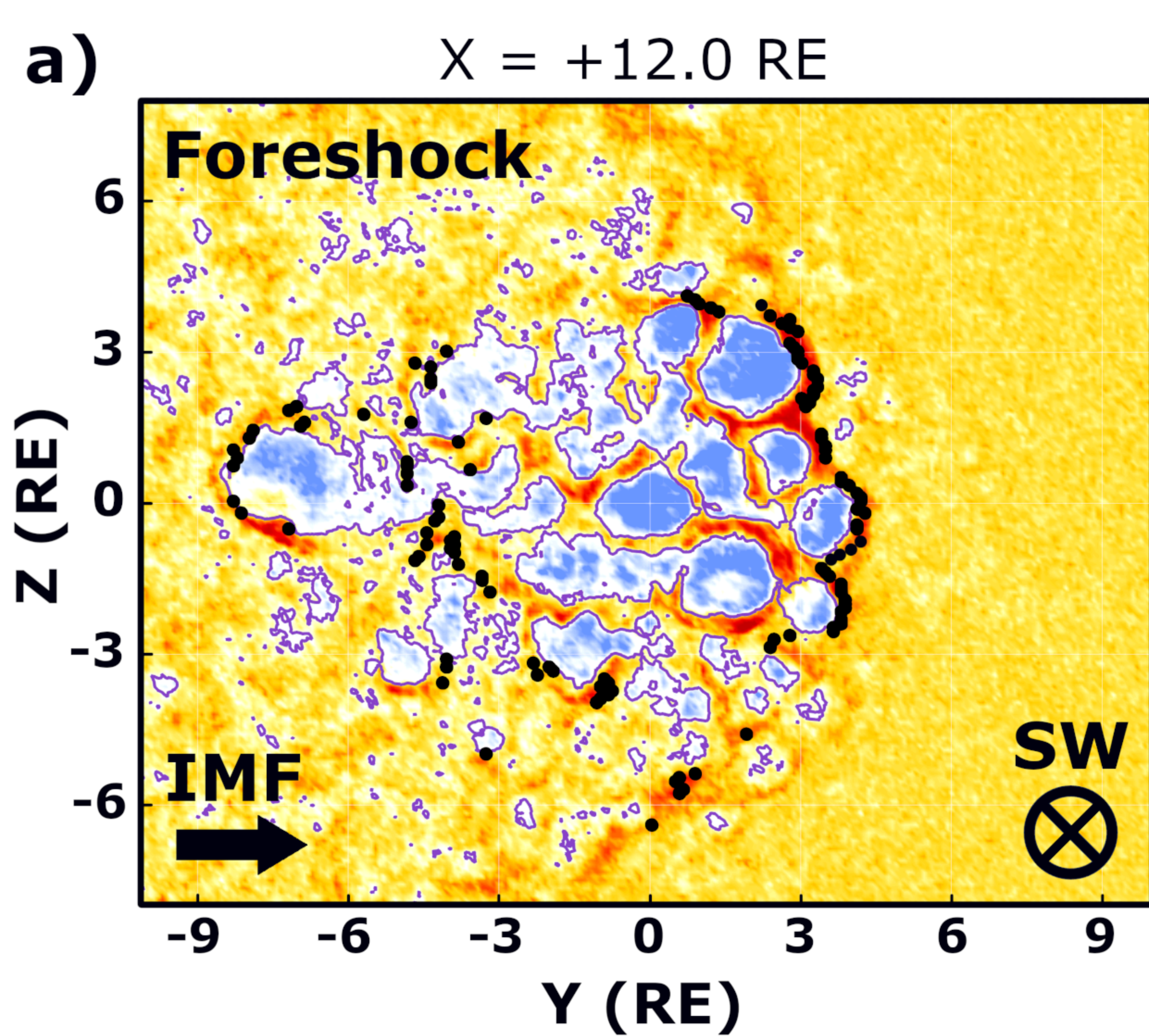


Figure 5.

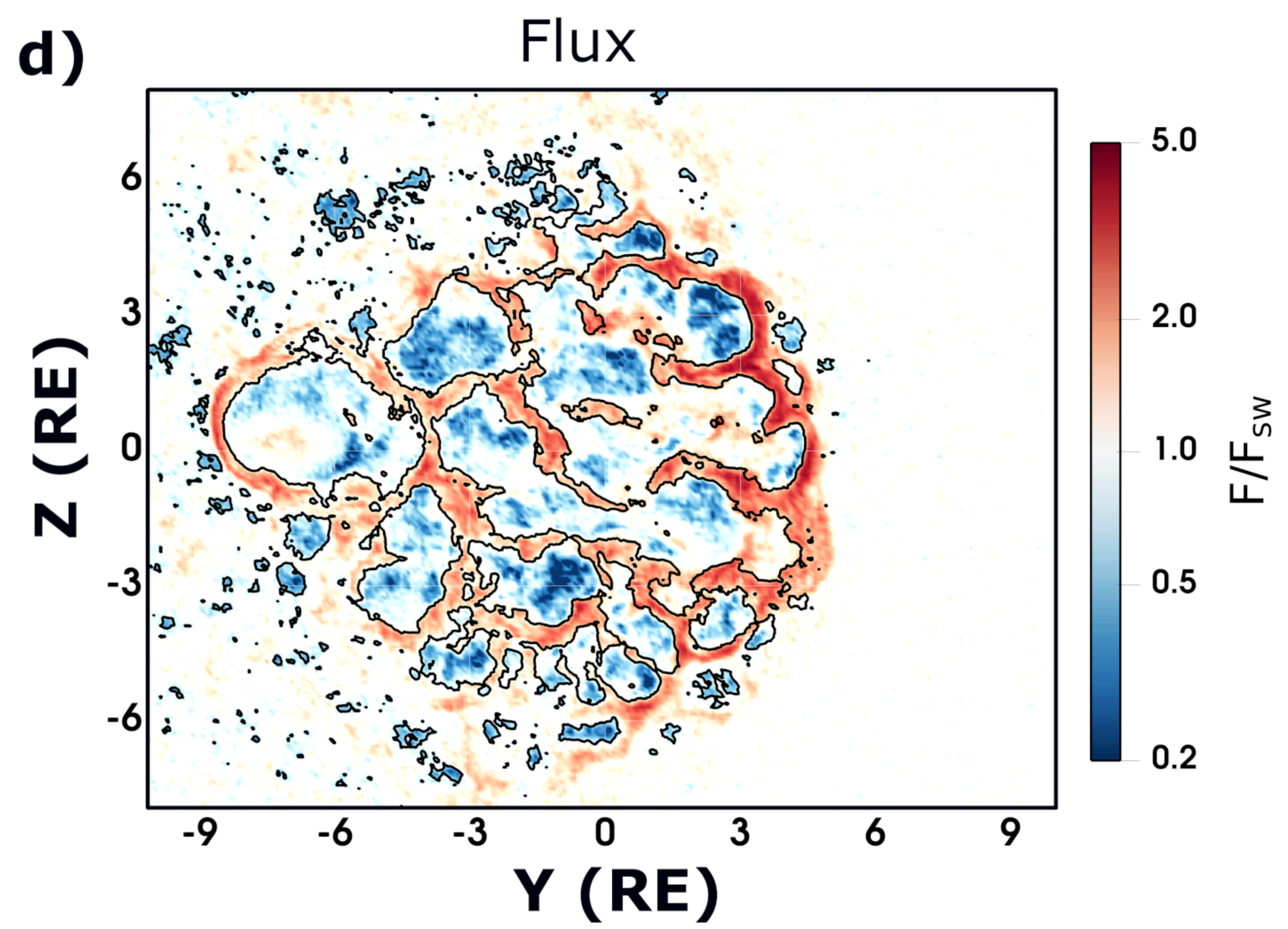
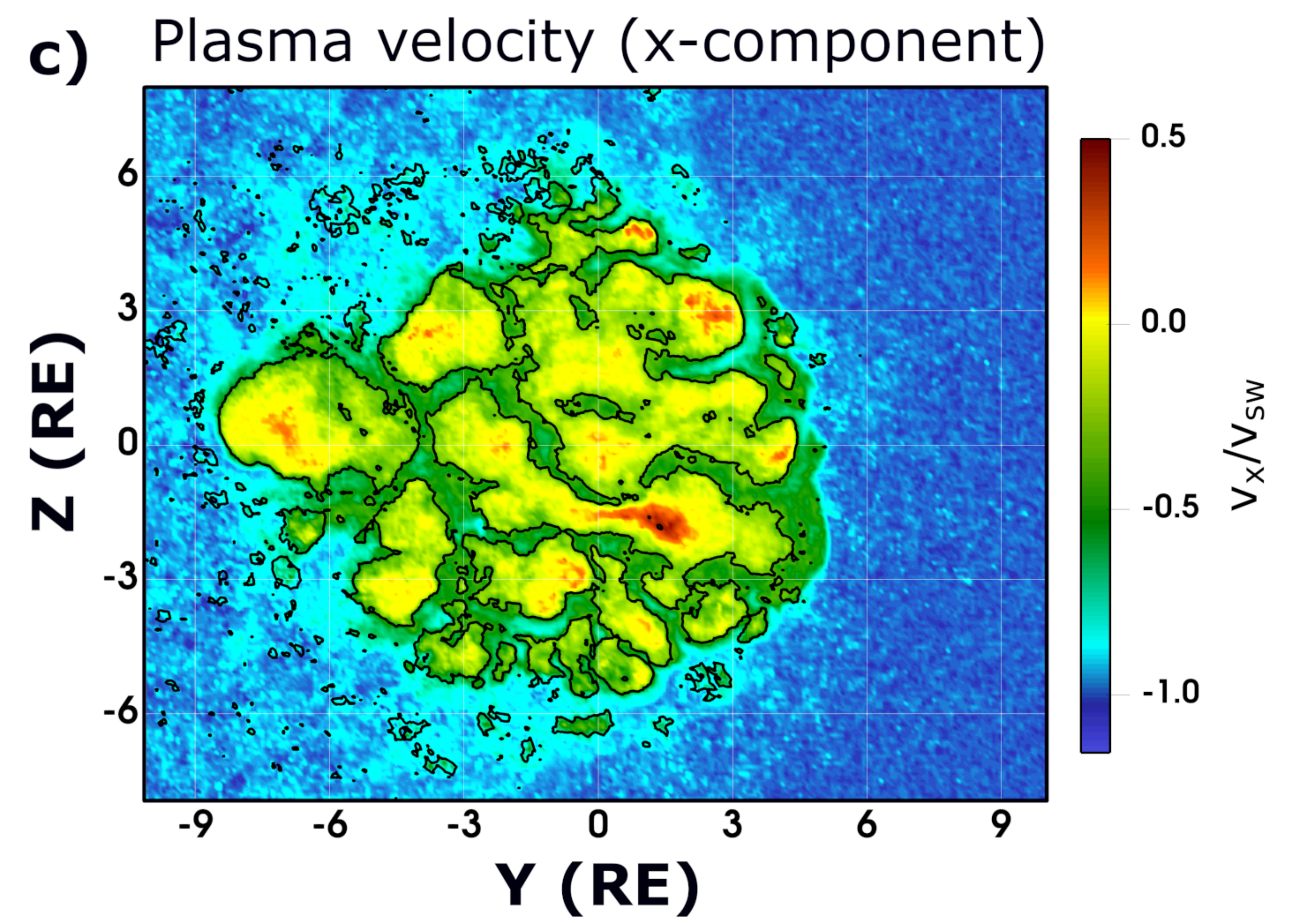
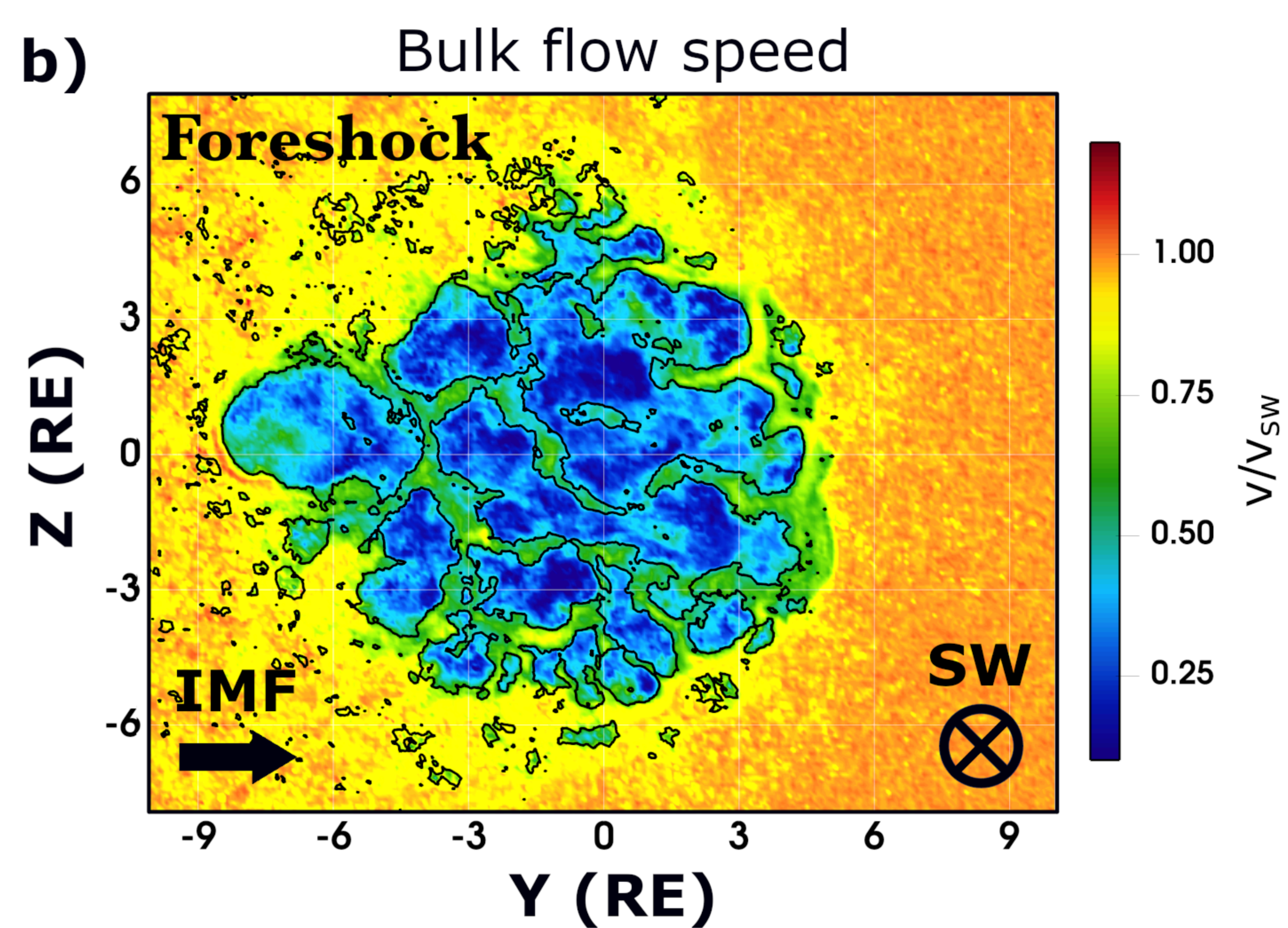
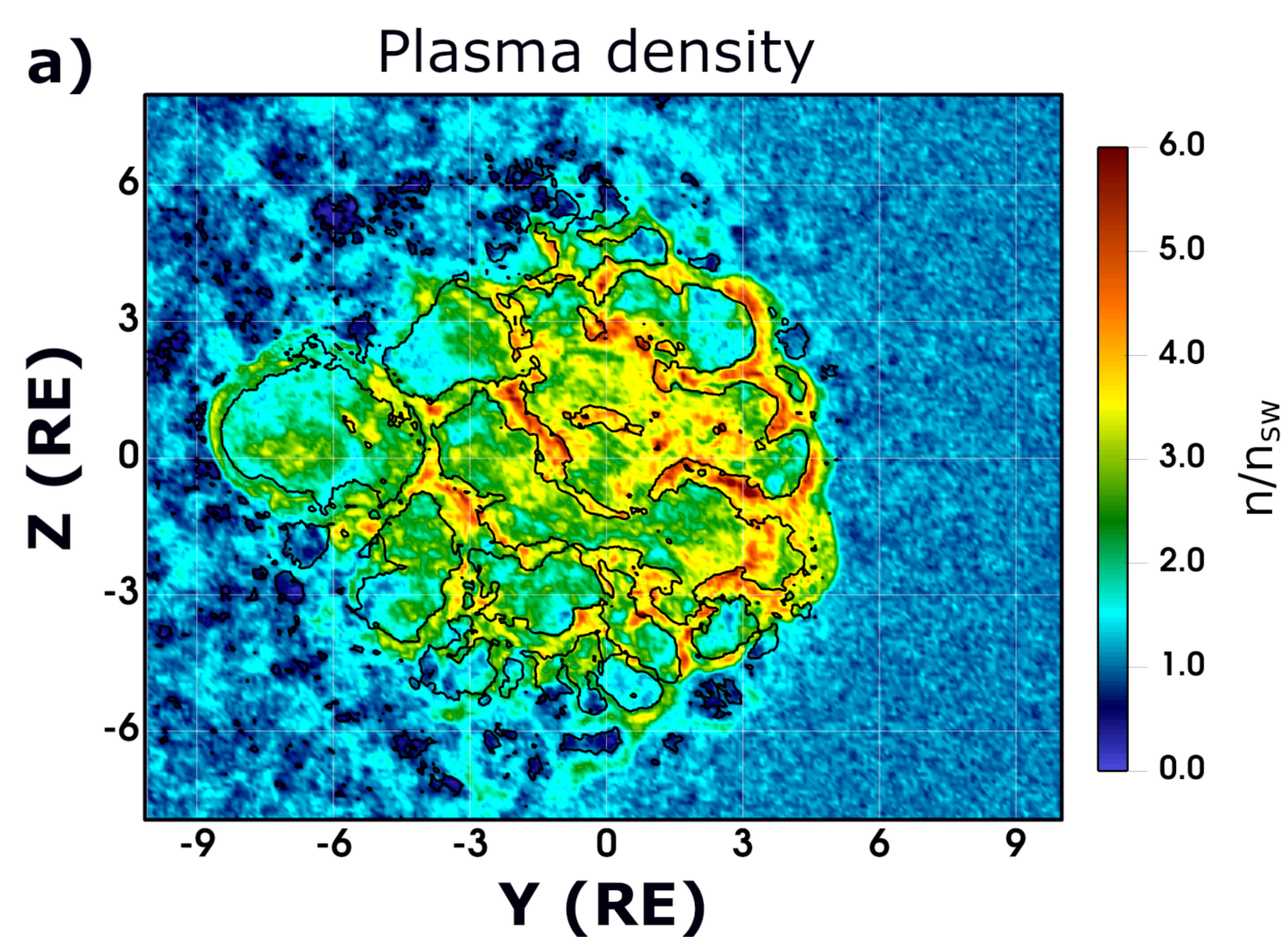


Figure 6.

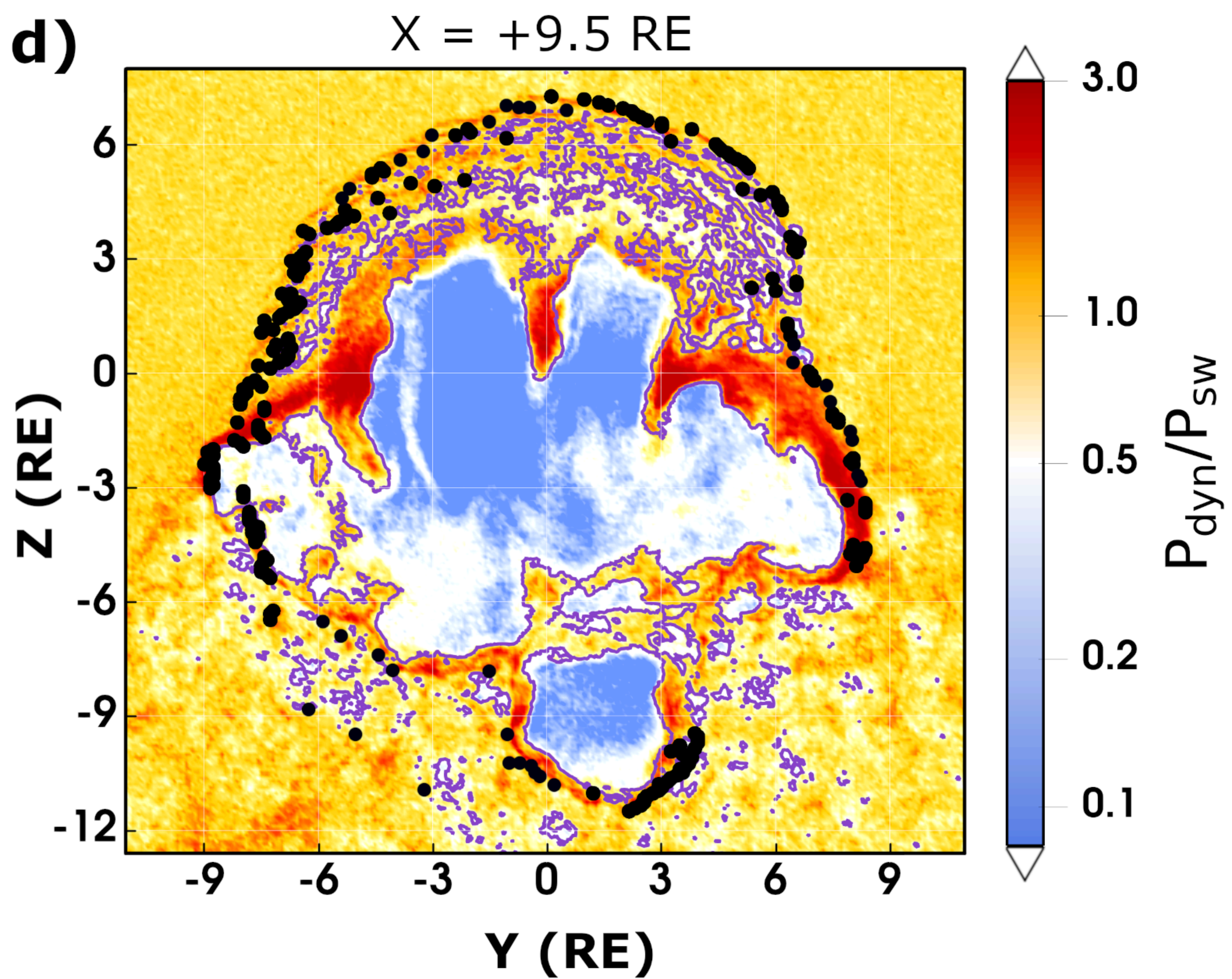
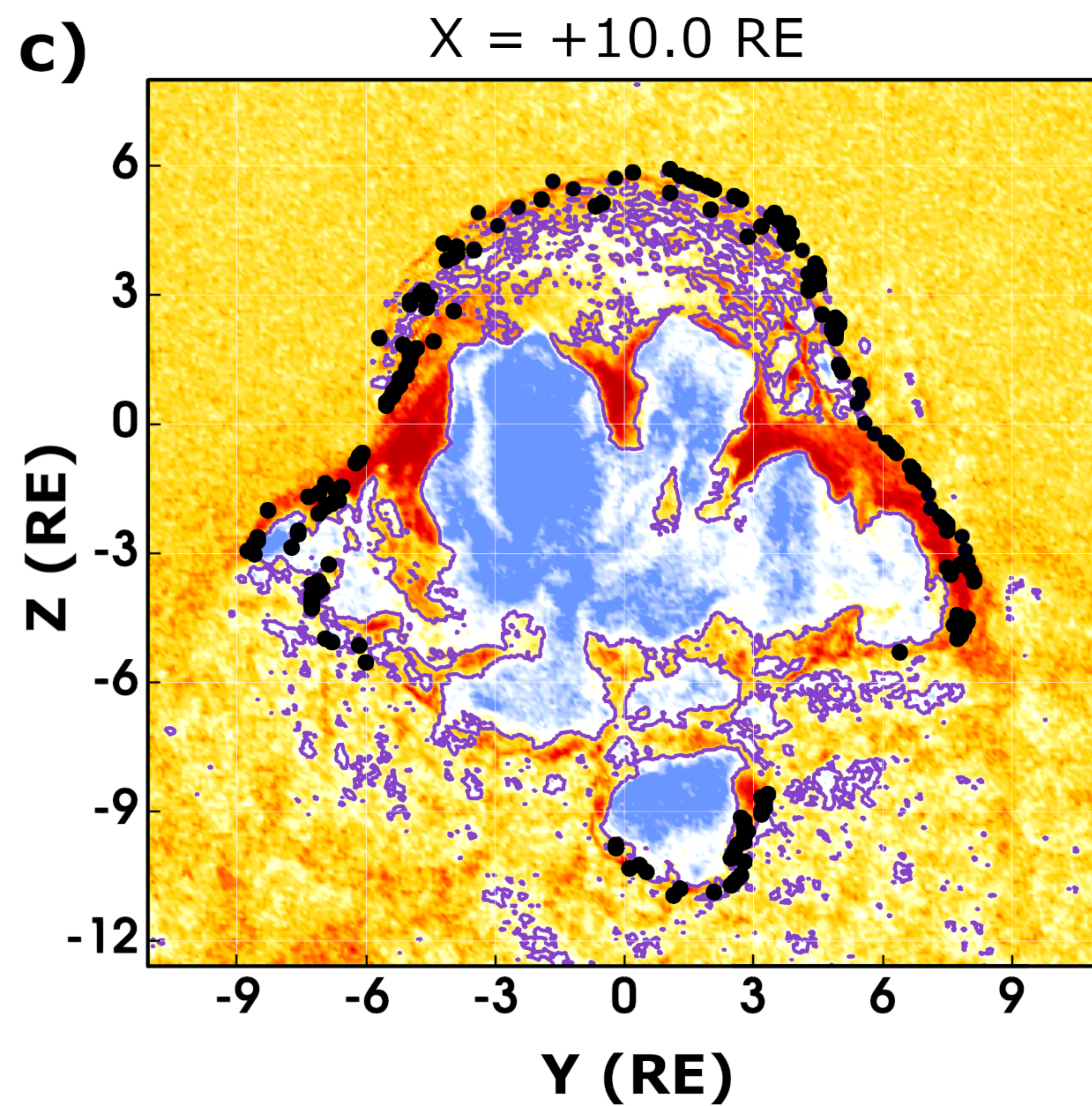
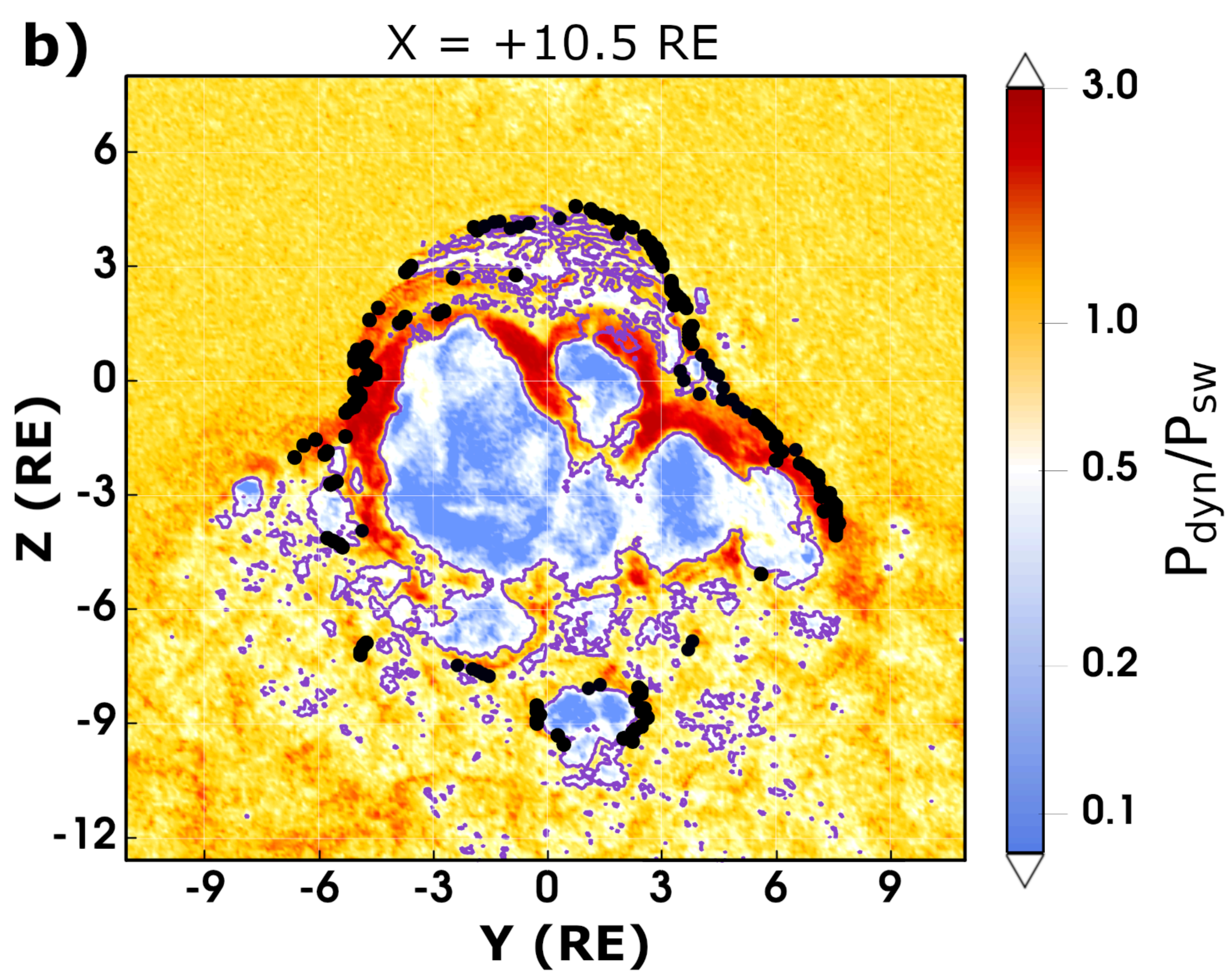
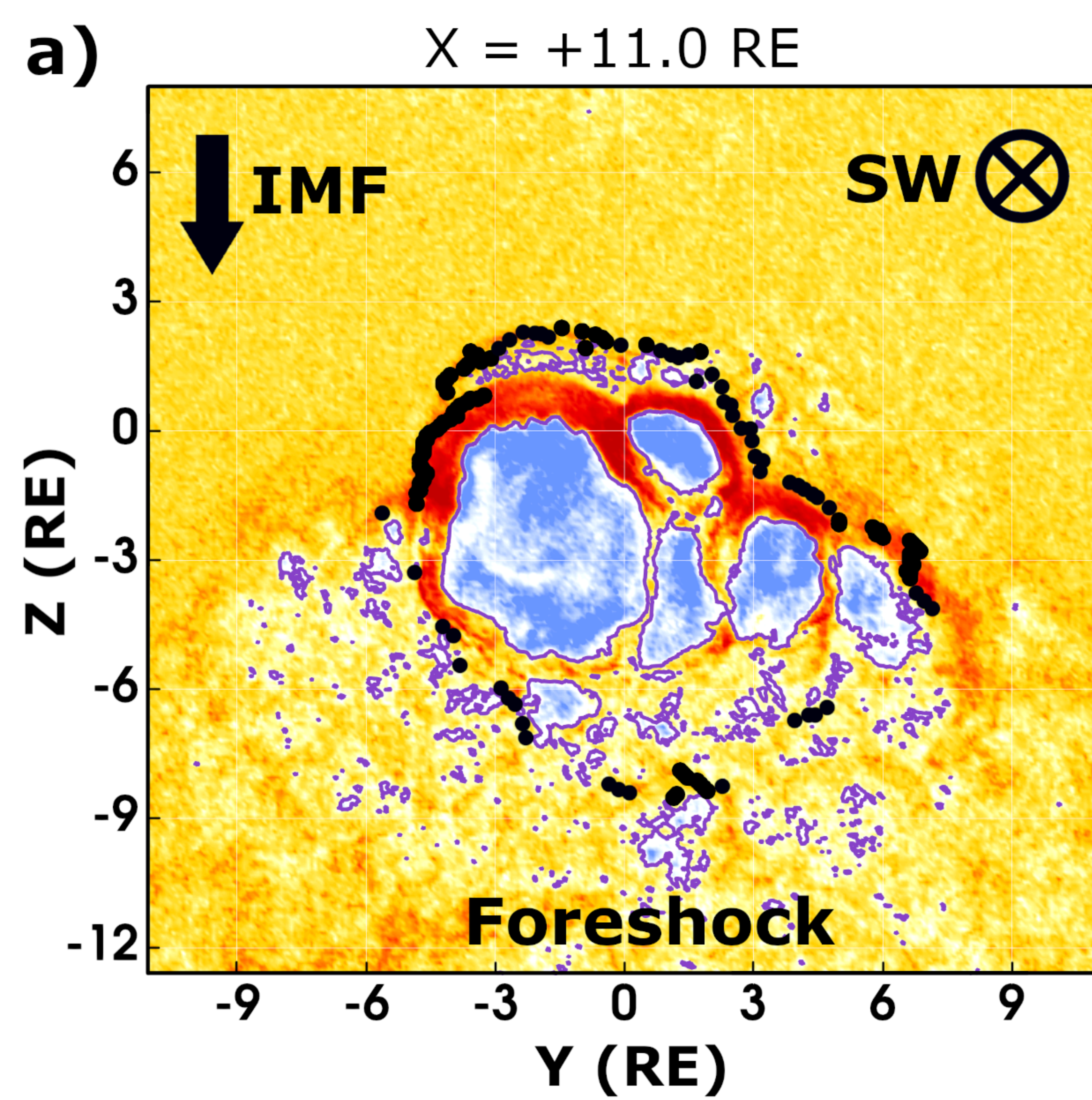


Figure 7.

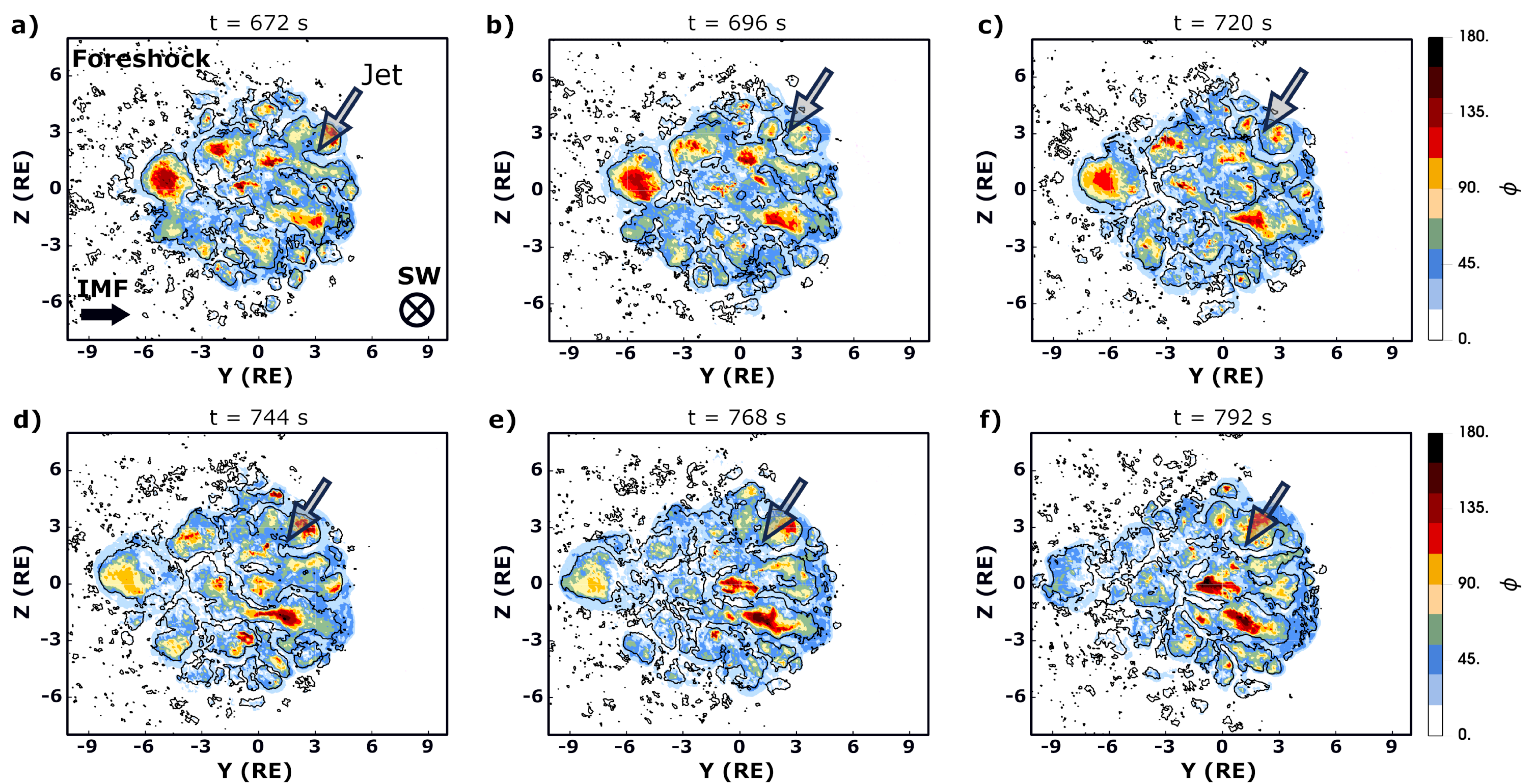
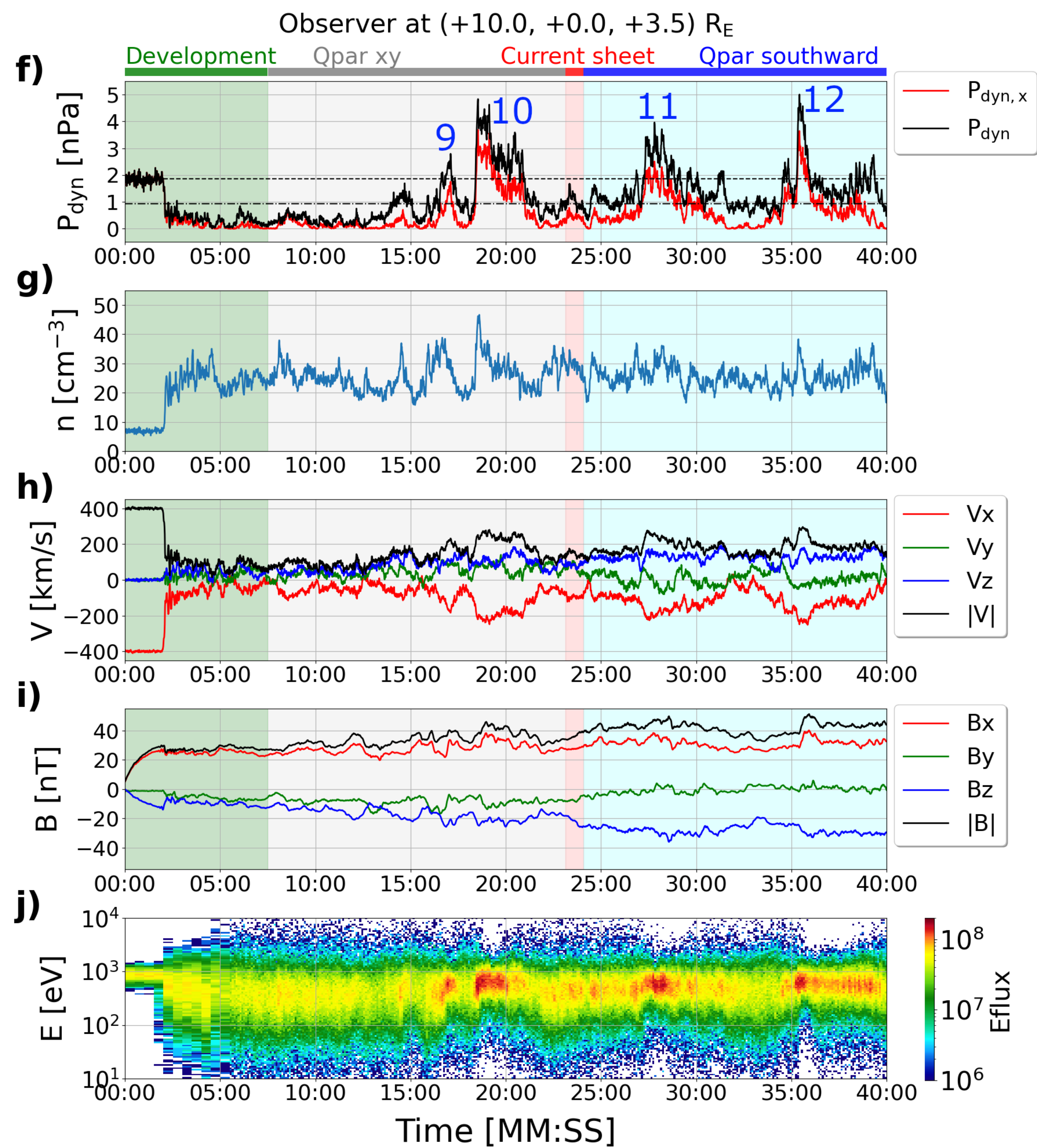
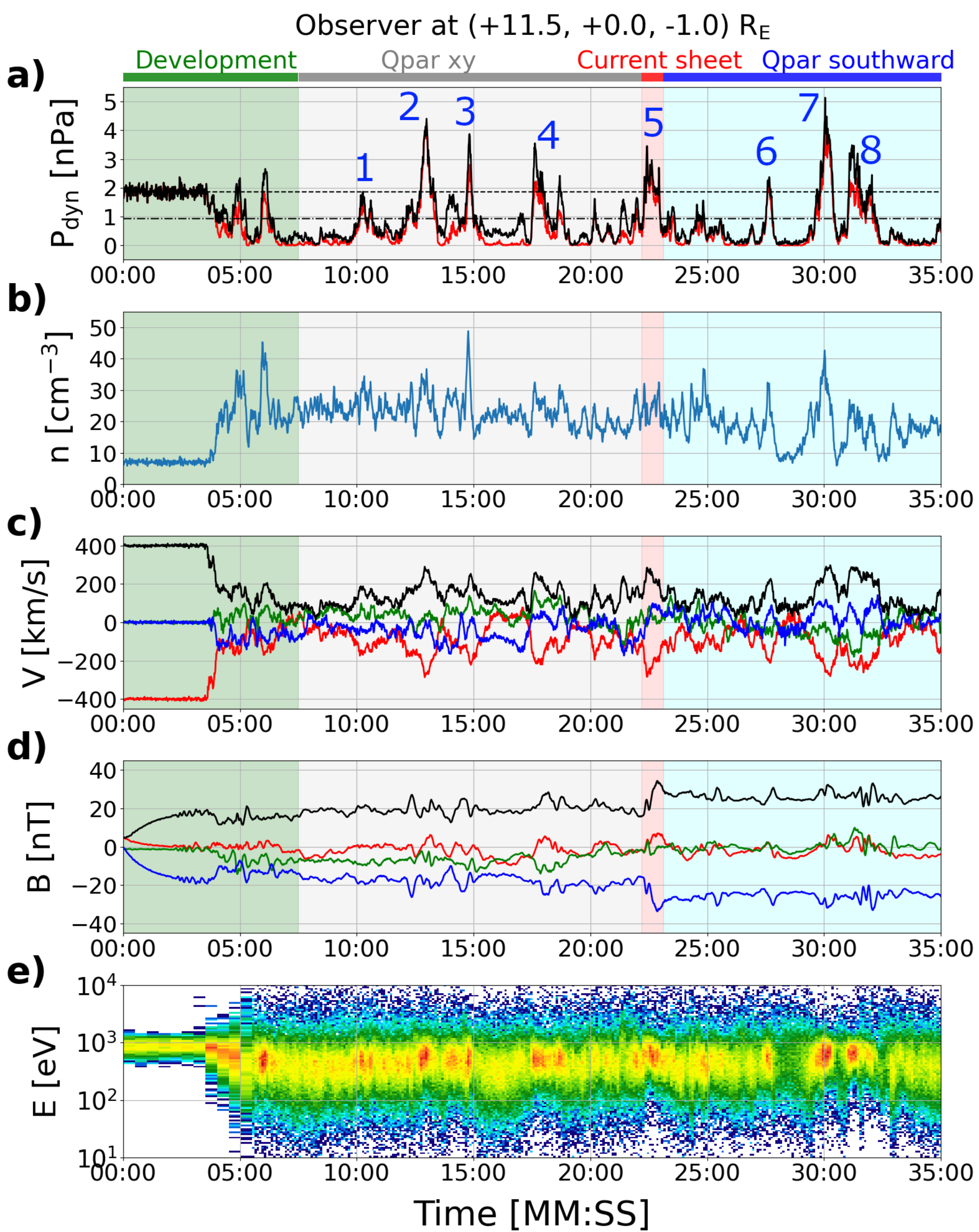


Figure 8.



Supporting Information for “Unveiling the 3D Structure of Magnetosheath Jets”

Shahab Fatemi¹*, Maria Hamrin¹, Eva Krämer¹, Herbert Gunell¹, Gabriella

Nordin¹, Tomas Karlsson², Oleksandr Goncharov³

¹Department of Physics, Umeå University, Umeå, Sweden

²School of Electric Engineering and Computer Science, KTH Royal Institute of Technology, Stockholm, Sweden

³Faculty of Mathematics and Physics, Charles University, Prague, The Czech Republic

Contents of this file

1. Figures S1 to S7

Additional Supporting Information (Files uploaded separately)

1. Captions for Movies S1 to S5

Introduction Here, we present figures and movies that provide supporting information to the main text and figures in our manuscript.

*Address: Linnaeus väg 20, 901 87 Umeå,

Sweden; email:

shahab.fatemi@amiticode.com;

shahab.fatemi@umu.se

Movie S1.

Amitis hybrid-kinetic simulation results presented in the GSM coordinate system for the R1Y simulation from time 640 s (i.e., 10:40) to 1200 s (i.e., 20:00) in the xy (equatorial) plane at $z = 0$. The background color, similar to Figure 2 in the main text, shows plasma dynamic pressure in logarithmic scale, normalized to the upstream solar wind dynamic pressure, $P_{\text{sw}} = 1.86 \text{ nPa}$. The sphere centered at the origin of the coordinate system represents the inner boundary of our simulation at $4.7 R_E$ with a projected plasma flux precipitating into the inner boundary, normalized to the solar wind flux $F_{\text{sw}} = 2.8 \times 10^{12} \text{ m}^{-2} \text{ s}^{-1}$. The solid black contour lines show $P_{\text{dyn},x} = 0.5 P_{\text{sw}}$, i.e., the Plaschke criterion for identifying magnetosheath jets, explained in the Model and Methods section in the main text.

Movie S2.

Similar to Movie S1, but showing different quantities. In this movie, the background color shown in the xy plan illustrates the y -component of the electric current density, J_y in the units of the nA/m^2 . The sphere shows the inner boundary of our simulation at $4.7 R_E$ with projected field-aligned currents (FAC) at the boundary.

Movie S3.

Amitis hybrid simulation results obtained from run R1Y from time 640 s (i.e., 10:40) to 1200 s (i.e., 20:00) in the GSM coordinate system, presenting the dynamic pressure normalized to the upstream solar wind dynamic pressure, $P_{\text{sw}} = 1.86 \text{ nPa}$ in the yz plane at $x = +11.5 R_E$, similar to the time snapshot shown in Figure 4c in the main text. The

geometry of the plan is similar to those shown in Figure 4 in the main text.

Movie S4.

Amitis hybrid-kinetic simulation results show the global structure of the solar wind plasma interaction with Earth. The background color shows the magnitude of the magnetic field in logarithmic scale in (left) the xy plane at $z = 0$ and (right) the xz plane at $y = 0$, both presented in the GSM coordinate system. The presented planes are perpendicular to each other, showing the 3D structure of the magnetic fields. The solar wind flows along the $-x$ axis (from right to left), shown by the yellow arrows. The orientation of the IMF is also shown by the white arrow on each plane. This movie shows in total 40 minutes of real-time solar wind interaction with Earth, covering the R1Y and R1S simulations. From time 00:00 to 14:20, the IMF is on the xy plane with $B_z = 0$ (i.e., run R1Y). At time 14:20, a current sheet arrives at $x = +40 R_E$, where the IMF orientation changes southward without changing its initial magnitude (i.e., run R1S). After ≈ 7 minutes, the current sheet reaches the dayside magnetosphere. Before the arrival of the current sheet, the ion foreshock region is visible upstream of the bow shock on the xy plane. During the passage of the current sheet, the entire system including the foreshock, bow shock, and the magnetosphere, responds to the changes in the IMF orientation. After that, the foreshock region is mainly visible in the xz plane. Since the magnitude of the IMF and solar wind plasma parameters remain unchanged during the entire simulation, no signature of the current sheet is evident in this movie. The IMF magnitude is 5 nT, marked as $|B_{\text{IMF}}|$ on the color bar.

Movie S5.

Amitis hybrid-kinetic simulation results show the global structure of the solar wind plasma interaction with Earth. The background color shows the plasma density in logarithmic scale in (left) the xy plane at $z = 0$ and (right) the xz plane at $y = 0$, both presented in the GSM coordinate system. The geometry of the planes is similar to those presented in Movie S4. The solar wind plasma density is 7 cm^{-3} , marked as n_{sw} on the color bar.

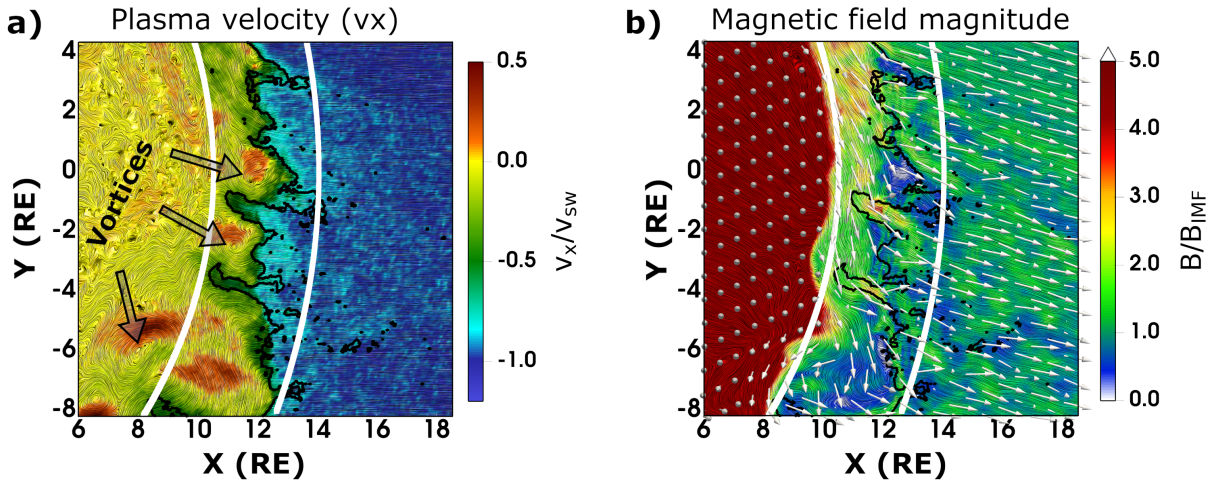


Figure S1. Hybrid simulation results in the xy (equatorial) plane from a zoomed-in region to the white rectangle in Figure 2a in the main text. The geometry of the cuts is the same as those described in Figure 2. Both panels here were previously shown in Figure 3. Here, we have added more details to them that could not become apparent in Figure 3. (a) Similar to Figure 3c. The background color shows the x -component of the solar wind velocity, v_x , normalized to the upstream solar wind speed, $v_{sw} = 400$ km/s. The streamlines show the direction of the plasma flow motion. Both jets have a forward velocity component towards the magnetopause, and a few Kelvin-Helmholtz-like vortices are visible in this panel, marked by arrows. (b) Similar to Figure 3f. The background color shows the magnitude of the magnetic field normalized to the strength of the IMF, $B_{IMF} = 5$ nT. The background streamlines together with arrows show the direction of the magnetic field. Inside the magnetosphere ($x \lesssim 9 R_E$), the magnetic field lines primarily point northward (outward in the plane shown), and therefore, only the arrowheads are visible.

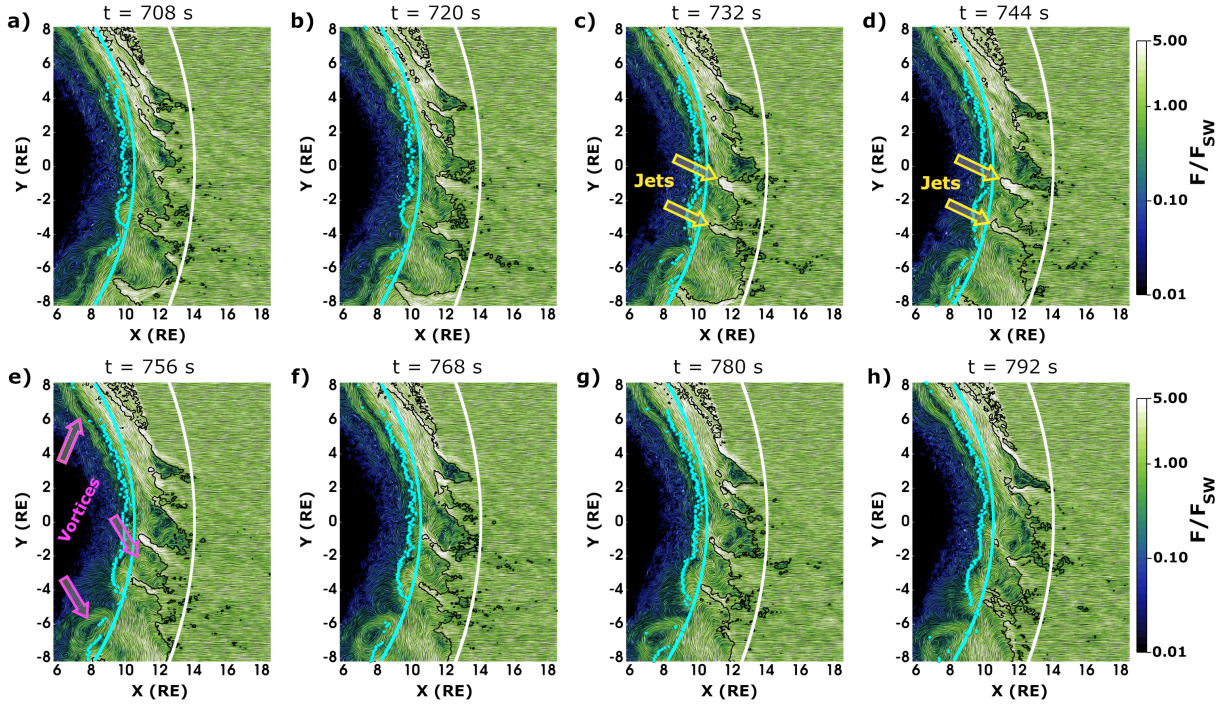


Figure S2. Time evolution of the magnetosheath jets in the xy plane at $z = 0$ obtained from our hybrid plasma model for the R1Y simulation setup. Background color is the normalized proton flux on a logarithmic scale. The streamlines show the direction of the plasma flow. The solid contour lines mark $P_{\text{dyn}} = 0.5 P_{\text{SW}}$. Several jets can be seen at different times, and, for example, two of them are marked by yellow arrows in panels c and d. In addition, a few Kelvin-Helmholtz-like vortices are apparent in several panels, and three of them are marked by pink arrows in panel e. The cyan dots denote the magnetopause boundary estimated from our simulations. The solid cyan and white lines, respectively, mark the magnetopause and bow shock boundaries from the empirical model by Chao et al. (2002). The geometry of the planes is similar to those presented in Figure 3 in the main text.

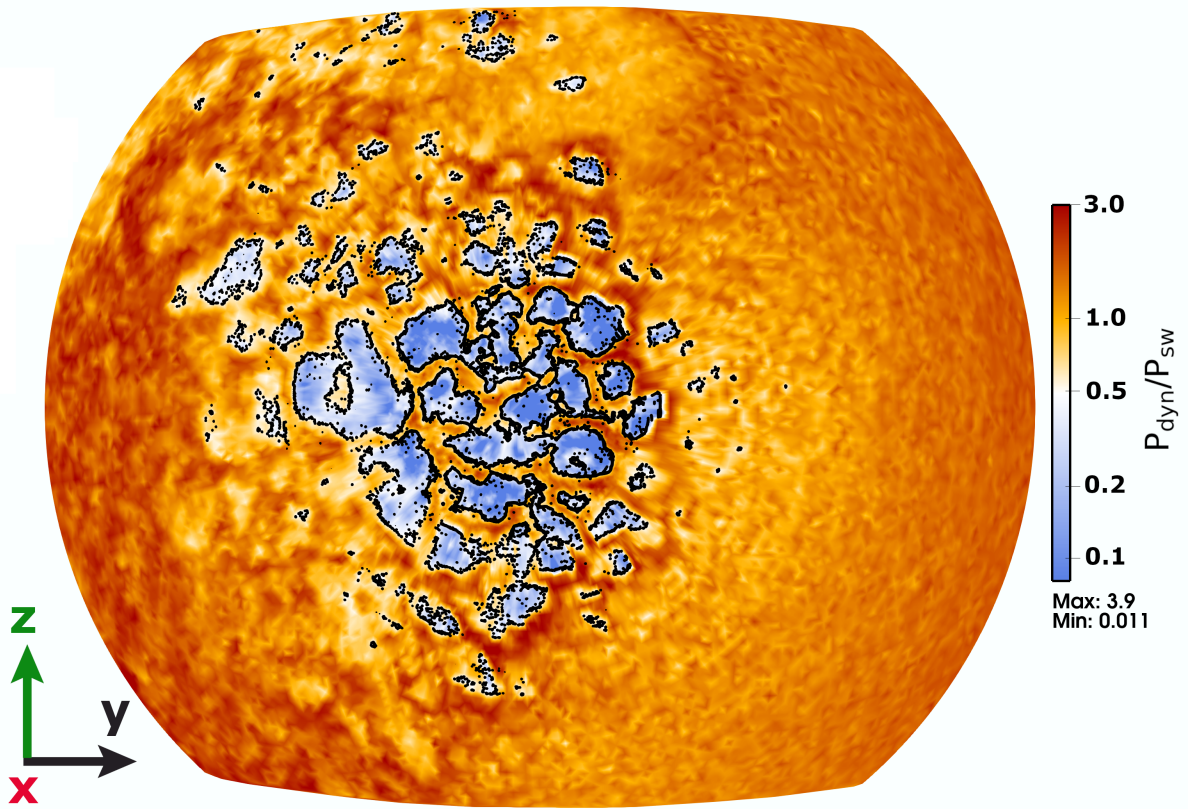


Figure S3. Amitis hybrid simulation results obtained from run R1Y at time $t = 744$ s in the GSM coordinate system, presenting the dynamic pressure normalized to the upstream solar wind dynamic pressure, $P_{\text{sw}} = 1.86$ nPa mapped on a 3D curved structure in the magnetosheath adjacent to the bow shock. The solid black contour lines highlight $P_{\text{dyn},x} = 0.5 P_{\text{sw}}$ (i.e., the Plaschke criterion for identifying magnetosheath jets). Given the complexity of this geometry and the asymmetric nature of the magnetosheath structure, we present our simulation results exclusively on simple 2D flat plans, as shown in Figures 4–7 in the main text. This figure here is added to demonstrate that the structure of the magnetosheath presented in the main text is not associated with the geometry of the 2D slices. Indeed, the jet structures shown in Figures 4–7 are similar to those mapped on a 3D curved plane shown here.

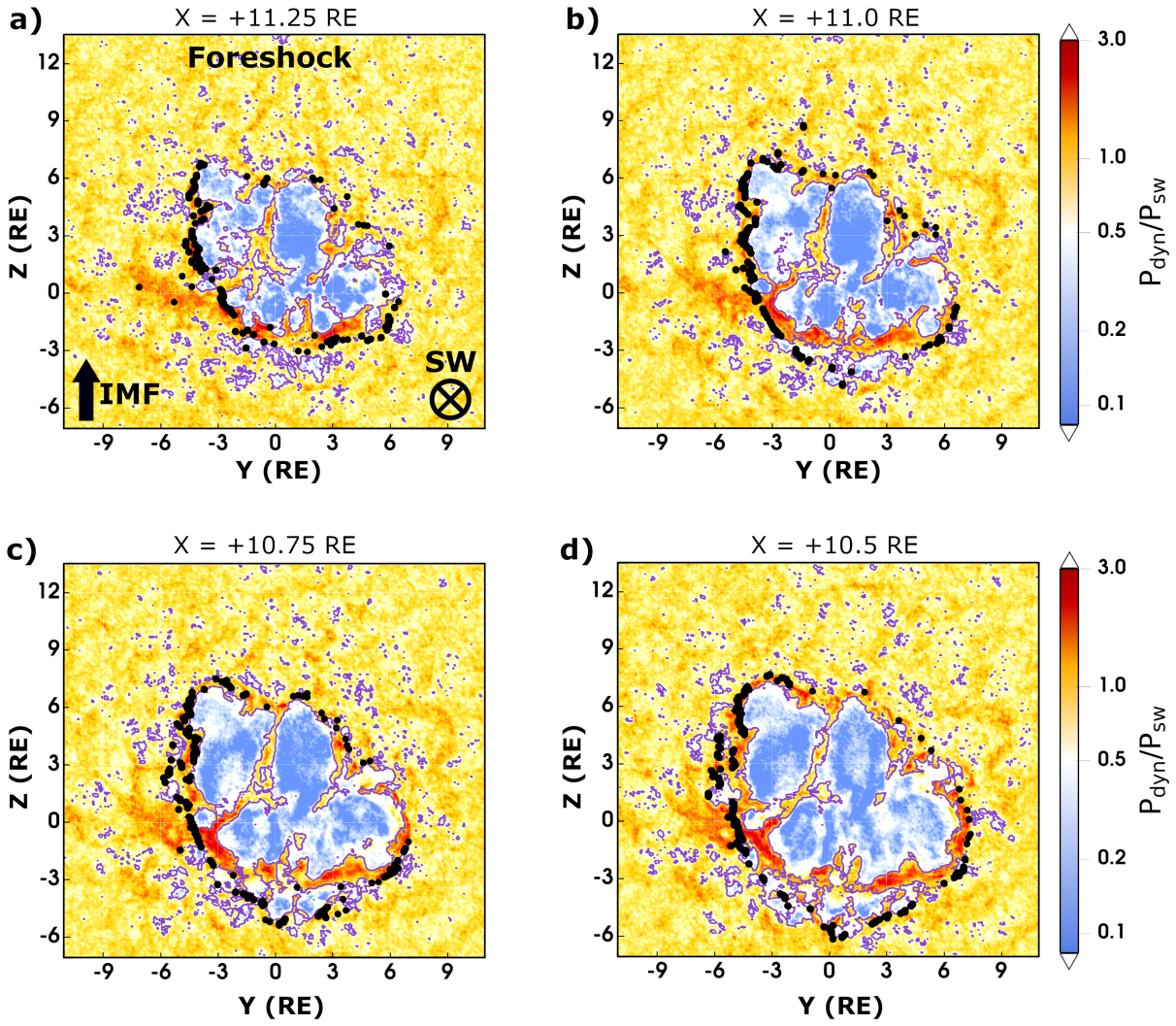


Figure S4. Hybrid simulation results obtained during the northward IMF (run R1N) at time $t = 3060$ s, presenting the dynamic pressure normalized to the upstream solar wind dynamic pressure in the yz plane at different distances from the Earth's center: (a) $x = +11.25 R_E$, (b) $x = +11.0 R_E$, (c) $x = +10.75 R_E$, and (d) $x = +10.5 R_E$. The figure format is the same as that shown in Figures 4 and 6 in the main text.

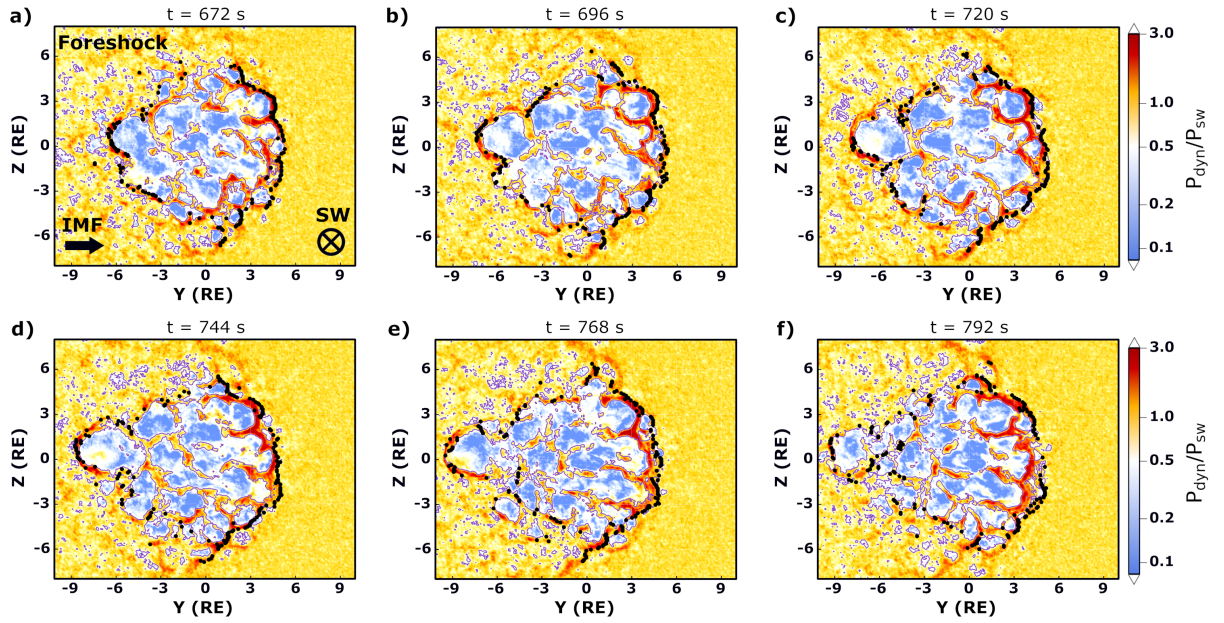


Figure S5. Hybrid simulation results obtained from run R1Y in the yz plane at $x = +11.5 R_E$ at six different simulation times: (a) 672 s, (b) 696 s, (c) 720 s, (d) 744 s, (e) 768 s, and (f) 792 s. The background color illustrates the normalized dynamic pressure. The solid black contour lines highlight $P_{\text{dyn},x} = 0.5 P_{\text{sw}}$ (i.e., the Plaschke criterion for identifying magnetosheath jets), and the black dots indicate the bow shock boundary obtained from our simulations, explained in the Materials and Methods section. The magnetosheath is the region surrounded by the bow shock boundary, and the jets are the filamentary structures with dynamic pressure $\geq 0.5 P_{\text{sw}}$ in the magnetosheath. The figure format is the same as that shown in Figure 7.

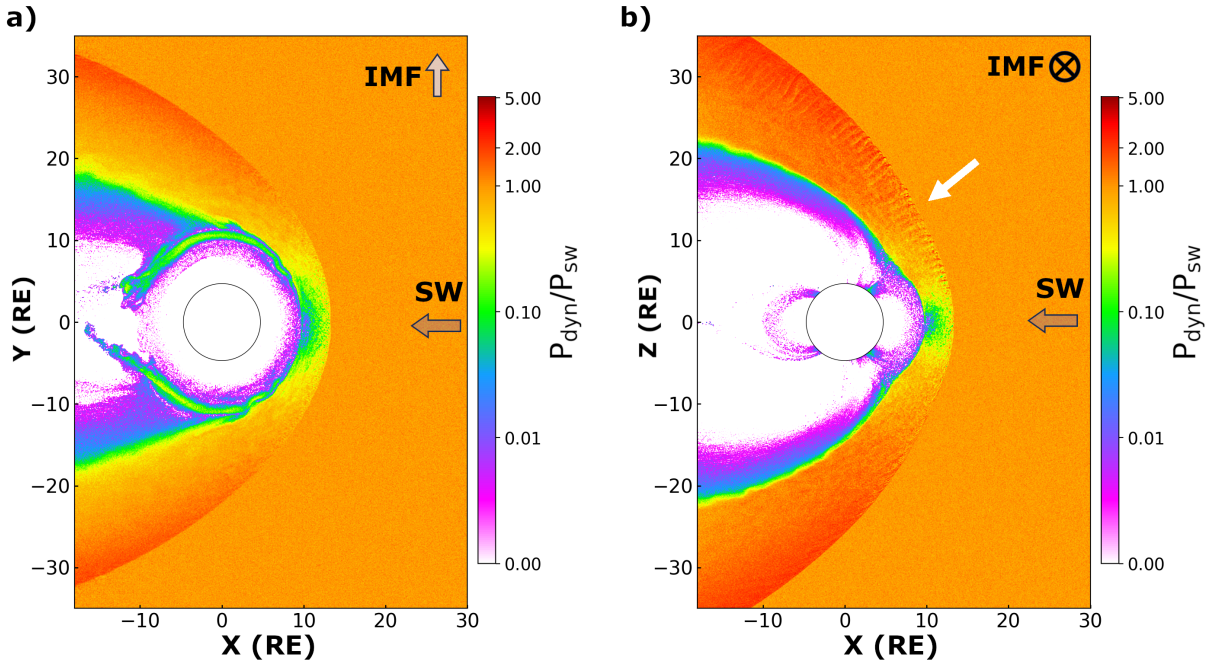


Figure S6. Hybrid simulation results when the IMF is perpendicular to the solar wind (run R2), obtained at time $t = 900$ s, presenting the dynamic pressure normalized to the upstream solar wind dynamic pressure, $P_{\text{sw}} = 1.86$ nPa in the (a) xy plane at $z = 0$ and in the (b) xz plane at $y = 0$. The solar wind and IMF orientations at different planes are shown by gray arrows. In panel b, the solar wind convective electric field, $\mathbf{E} = -\mathbf{v} \times \mathbf{B}$, is pointing upward along the $+z$ axis. The white arrow in panel b points to the quasi-perpendicular shock where many small irregular filamentary features, somewhat similar to the magnetosheath jets, are evident downstream of the quasi-perpendicular shock at the $+E$ hemisphere of the magnetosphere. Identifying the nature and characteristics of these filamentary structures are outside the scope of the current study, and will be investigated in a separate research.

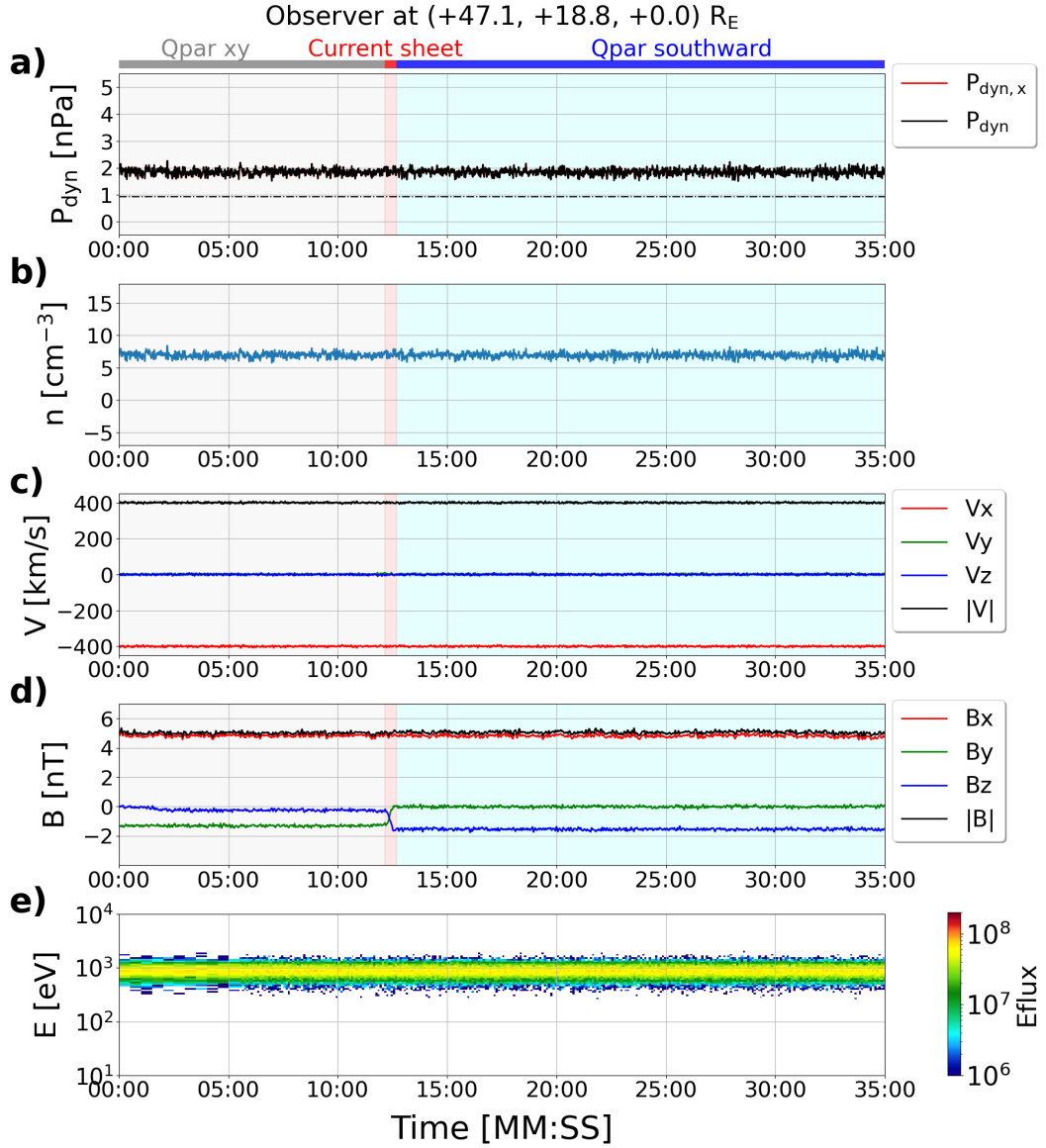


Figure S7. The temporal evolution of (a) plasma dynamic pressure, (b) proton density, (c) proton velocity, (d) magnetic field, and (e) differential proton flux, examined at the position of a stationary virtual observer located in the solar wind and far away from any magnetospheric and foreshock disturbances at $(+47.1, +18.8, 0.0) R_E$. The magnetic transient (current sheet) arrives at the observer at time $\approx 12:30$, highlighted in red. The description of different panels is the same as that shown in Figure 8 in the main text. We intentionally did not place the observer only along the x axis to ensure the terrestrial disturbances do not reach the observer during the magnetic transients.